Title
A THz-Driven Electron Gun

Author
Lewis, Samantha Michelle

Publication Date
2020

A THz-Driven Electron Gun

by

Samantha Michelle Lewis

A dissertation submitted in partial satisfaction of the

requirements for the degree of

Doctor of Philosophy

in

Nuclear Engineering

in the

Graduate Division

of the

University of California, Berkeley

Committee in charge:

Professor Karl van Bibber, Chair
Assistant Professor Emilio Nanni
Professor Lee Bernstein
Professor David Attwood

Fall 2020

A THz-Driven Electron Gun

Abstract

A THz-Driven Electron Gun

by

Samantha Michelle Lewis

Doctor of Philosophy in Nuclear Engineering

University of California, Berkeley

Professor Karl van Bibber, Chair

This thesis presents the development of a THz-driven electron gun and associated beam characterization assembly. The THz gun is a 2 cell electroformed copper structure and uses a copper tip field emission cathode. The cells operate in the π mode at 110.081 GHz and are designed to be powered by a 110 GHz gyrotron oscillator. For 500 kW of input power, the gun is expected to produce bunches of electrons accelerated to a peak energy of 365 keV. Electromagnetic simulations predict the fields on the surface of the cathode will reach 3.9 GV/m for this input power, resulting in 51 fC bunches. The beam is accelerated over a distance of 1.6 mm in the two cells.

The gun structure and characterization assembly are designed to operate over a range of input powers beyond the nominal operating point of 500 kW. The electron beam characterization assembly consists of a focusing solenoid, a dipole-based energy spectrometer, an on-axis microchannel plate detector, and a Faraday cup. The setup is designed to measure the energy spread, beam size, and current to characterize the gun performance. Each element in the assembly was custom designed for this setup and the expected energy range of the beam. The expected performance is based on modeling of the electromagnetic performance of the cells and 3D particle simulations of the beam dynamics and transport.

Fabricated gun cells were cold tested and an extensive study of cell tuning was performed. Several copper tip structures were successfully tuned using mechanical compression. This is the first demonstration of the mechanical tuning of individual W-band accelerator cavities. The effects of plating and etching were also studied. Further electromagnetic and particle modeling was performed to characterize the expected performance of the fabricated and tuned structures. One set of tuned cells was incorporated into the full assembly and cold tested under vacuum. The cell resonances occur at their expected frequencies and the performance is preserved after cycling between air and vacuum.

Contents

List of Figures

List of Tables

Acknowledgments

As I reflect on my time in graduate school after what has been an exceptionally challenging year, I am grateful for the wealth of people who have been a part of my life and this work. I have learned that nothing is more essential for success than having the support and companionship of colleagues and friends.

First, I would like to acknowledge my advisers and mentors. I have been fortunate to have mentors who are invested in my success and have given me both the guidance and the space to grow as a researcher. Thank you to Emilio Nanni for giving me the opportunity to work on this project, and for challenging me to keep pushing forward through the toughest moments. His mentorship was essential to my start as a researcher as an undergraduate, and I hope to continue to benefit from his wisdom throughout my career. I would also like to thank Karl van Bibber, my adviser at Berkeley. Karl's support and encouragement is unending, and he is always ready to do whatever he can to help his students. I appreciate that he valued my opinion and experience from day one in graduate school and encouraged me to forge my own path. It is with his support that I approach my future work with confidence.

Additionally, I would like to thank Lee Bernstein both for serving on this committee and for giving me the opportunity to discover my love of teaching. His passion for teaching is admirable and I was lucky to be able to work in his classroom. I also would like to thank David Attwood for his feedback on this thesis and his encouragement. Finally, I would like to thank Richard Temkin. As my undergraduate research adviser he gave me many opportunities to build my skills and explore my interests. Now as a collaborator, his advice has been essential to the success of this work.

My work at SLAC would not have been possible without the help of many colleagues and collaborators. I would like to thank my group members, especially Mohamed Othman, Emma Snively, and Annika Gabriel for their advice and comments on this thesis. I will miss their company and our lunches by the fountain. Thank you to Dennis Palmer for his guidance and help in the lab. I would also like to thank Julian Merrick and Andy Haase for their engineering wisdom which brought this project from concept to reality. A special thank you to Julian for truly going above and beyond to help me bring this project to completion. This work would not have been possible without him and I am eternally grateful for his support, patience, and friendship.

Further, this thesis would not have been possible without the work of everyone at SLAC's TID Advanced Prototyping and Fabrication shops. Thank you to Andy Nguyen, Dale Miller, Mario Cardoso, Walter Brown, Chuck Yoneda, and everyone at APF for their hard work and help with all of the various challenges that have popped up along the way. I would also like to acknowledge my collaborators at MIT who will soon be hosting this experiment. Thank you especially to Julian Picard for answering my never-ending series of questions.

My time in graduate school has been made richer by the friends I've been able to meet. My department at Berkeley was a fantastic home for the past several years. Thank you to my office-mates in the PANDA group—especially Amanda Lewis, Eric Matthews, Maria

Simanovskaia, Alex Droster, Bella Urdinaran, and Kelly Backes—for making my time on campus so enjoyable.

I want to thank Josh and Christie Rehak, Chris Poresky, and Joey Kabel for their friendship since those first days of graduate school and so many fantastic memories. Also thank you to Mario Ortega, Marissa Ramirez de Chanlatte, and Milos Atz for wonderful conversations and support in hard times. Thank you to James Kendrick and Koshy Thomas, the best roommates that anyone could ask for. All of you have made my years in Berkeley exciting, fulfilling, and memorable.

Finally, I want to thank my closest loved ones. Without them I would not be the person I am today. Yuanshen, thank you for everything. You have made my life richer and I don't know how I could have done this without you. Thank you to Chamille, who has believed in me and encouraged me through every obstacle. Your friendship means the world to me. Thank you to my sister Danielle, who brings endless joy to my life in ways big and small. Thank you to my parents, who have always encouraged me to follow my passions. I hope that I've made you all proud.

Chapter 1

Introduction

1.1 Motivation

Particle accelerator facilities are necessary tools of scientific study across a broad range of disciplines. Most major facilities in use today are electron accelerators. Ranging from small scale laboratory electron microscopes to large scale electron-based light sources, these devices enable scientists to study materials, examine samples, and observe new phenomena in ways that would not be possible otherwise. Two emerging uses for modern accelerators are the free electron laser (FEL) and ultrafast electron diffraction (UED). Free electron lasers use electrons to generate high power X-rays which can then be used to study a wide variety of chemical and biological samples. Ultrafast electron diffraction uses the particles themselves as a probe to study materials on femtosecond timescales. The performance of these instruments depends on many factors, but the quality of the electron source plays a primary role. In particular, the brightness of the electron source—the amount of particles the source delivers compared to the size of the beam—determines how the accelerator can be used.

There is strong demand within the scientific community for electron accelerator facilities that can reach higher powers, better resolution, and faster timescales. In order to meet the desired performance targets, new electron source technology is required [1]. Next-generation FEL facilities aim to produce higher energy X-rays with better temporal resolution, which will require brighter electron beams with shorter pulse lengths. Future UED facilities will require shorter bunches with smaller emittance and reduced energy spread to improve their temporal and spatial resolution. Existing facilities have already proven to be crucial for breakthroughs in biology, materials science, chemistry, and physics. The enormous discovery potential of future facilities provides a clear motivation for developing novel electron sources.

Advances in several areas of accelerator physics research provide a unique opportunity to develop a new kind of electron source: a THz-driven electron gun. Investigations of high gradient acceleration have found that there are significant benefits in using high frequency structures, including into the THz regime. So far, THz-based accelerators have been limited by the lack of availability of THz sources and the complexity of fabricating small cavities. High power THz sources have seen rapid development in recent years and are reaching the performance specifications required to power an accelerator [2, 3, 4, 5]. Meanwhile, advanced fabrication techniques have made it possible to create THz accelerator cavities which directly draw on design and operational experience of microwave-range accelerators [6, 7, 8]. Further, the development of particle simulation codes makes it possible to accurately model low energy, low charge beams including space charge forces. The design presented in this thesis aims to leverage these developments to create a new kind of compact, high gradient electron source.

1.2 Electron sources

1.2.1 Figures of merit

A key figure of merit of an electron source is its brightness. Brightness is a measure of the current per unit phase space area. There are several different definitions of the brightness that are useful in various circumstances. The 6D brightness defines the brightness over all 3 spatial dimensions. This value is most useful when discussing beam transport over a long beamline such as in FELs or synchrotrons. For electron sources, it is more appropriate to focus on the transverse plane. In Cartesian coordinates, the 4D transverse phase space is expressed in physical positions x and y and momenta p_x and p_y. The normalized transverse brightness is given by

$$B = \frac{\bar{I}}{4\pi^2 \epsilon_{Nx} \epsilon_{Ny}} \tag{1.1}$$

where $\bar{I}$ is the average beam current [9].[1] The normalized emittances ϵ_{Nx} and ϵ_{Ny} measure the area of the beam in the x-p_x and y-p_y phase space planes, respectively.

Higher brightness can be achieved by increasing the source current (charge per unit time) and decreasing the emittance. The desired bunch charge is determined by the application and beam quality requirements. In FELs and UED, higher bunch charge is not desirable above certain values because it can lead to beam degradation due to space charge effects and to damage in samples. Current FEL facilities have bunch charges up to 1 nC, but routinely operate with tens to hundreds of pC. UED facilities typically require bunch charges ranging from 0.1 fC to 1 pC. For a given bunch charge, the current can be increased by reducing the bunch length.

Decreasing the emittance at the source serves dual purposes, both increasing the brightness and improving spatial resolution. The particle distribution at the source typically determines the minimum achievable emittance in an accelerator, as a result of Liouville's theorem. This is discussed in more detail in Section 2.4. In the absence of particle loss, normalized emittance can only be reduced through techniques like electron beam cooling or

---

[1] This can also be used to express 5D brightness by using the peak current.

emittance exchange. Thus, it is vital to achieve the lowest emittance possible in the source itself.

1.2.2 Types of electron guns

In most particle accelerator facilities, the electrons are provided by an electron gun. Electron guns consist of a cathode and an accelerating stage. There are three main types of cathodes used in electron guns: thermionic, photoemission, and field emission. In each case, electrons are emitted from a material and then accelerated by either a constant electric potential or an oscillating electric field. Thermionic cathodes emit electrons when they are heated above a certain temperature, giving electrons in the cathode material enough energy to overcome the potential barrier and escape the surface. In a photocathode, the electrons are emitted via the photoelectric effect when a laser pulse is incident on the cathode material. Field emission guns use local electric field enhancement to lower the potential barrier and allow electrons to tunnel through, escaping the surface.

The choice of cathode type depends on the requirements of the application. Most guns in use in current accelerator facilities are photocathodes due to the high degree of control provided by the laser pulse and the resulting beam quality. Field emission guns are most commonly found in electron microscopes due to their compact design. However, there is great interest in developing new field emission guns for FEL and UED applications. Field emission guns can be driven by the same source as accelerator cavities (see Section 2.2.3), making them less susceptible to difficulties with timing and stability. Field emission cathodes are also of interest for developing photo-field emission sources. Photo-field emission sources combine field emission on a sharp tip with an incident laser pulse to get very fast, low emittance beams for applications such as ultrafast electron microscopy [10, 11, 12, 13].

1.3 Particle accelerators

Particle accelerators transfer energy from electromagnetic waves to charged particles. The Lorentz force on a charged particle in the presence of an electric field $\mathbf{E}$ and a magnetic field $\mathbf{B}$ is given by

$$\mathbf{F} = q\left(\mathbf{E} + \mathbf{v} \times \mathbf{B}\right) \tag{1.2}$$

where q is the particle charge and $\mathbf{v}$ is the particle velocity. Thus, particles can be accelerated along the direction of an electric field, $\mathbf{F} = q\mathbf{E}$. The acceleration typically takes place in multiple stages. Electrostatic accelerators use electrodes at varying potentials to accelerate particles across a gap. RF accelerators use bounded oscillating electric and magnetic fields for the same purpose. The magnitude of the electric field directly determines the energy the particle gains. The relevant unit of particle energy is the electronvolt (eV), which is defined as the energy an electron with charge e gains traversing a 1 V potential.

RF accelerators are based on eigenmodes of the electric and magnetic fields supported by waveguides or cavities. An eigenmode is characterized by the frequency at which the fields oscillate, quoted in Hz (cycles per second). These eigenmodes can be fully confined (standing waves) or propagating (traveling waves). Traveling-wave accelerators operate by slowing the electromagnetic wave such that the phase velocity of the wave is close to the velocity of the particle. They have net power flow which is eventually coupled out of the structure. These accelerators can provide significant acceleration because the particle is always experiencing the maximum field. However, the high power flow makes them susceptible to breakdowns (discussed in Section 1.3.2) [14]. This acceleration scheme is most applicable for high energy electrons where the beam velocity is near the speed of light. The electron gun presented in this thesis is a standing-wave design, and thus standing-wave accelerators will be discussed in further detail.

1.3.1 Standing-wave accelerators

Standing-wave accelerators do not have not have net power flow on axis. They are based on cavity eigenmodes with a fixed phase shift from one cell to the next. The theory of electromagnetic cavities is described in Section 2.1. A schematic of a standing-wave accelerator is shown in Figure 1.1. A typical accelerator cavity is a 'pillbox' with an aperture in the center for the beam. In this geometry, the possible accelerating modes are TM modes that have on-axis electric fields in the z direction. The transverse dimensions of the cavity determine the resonant frequency of the accelerating mode, and the length is set such that the orientation of the field is always aligned to accelerate the particle by the time it reaches the next cell.

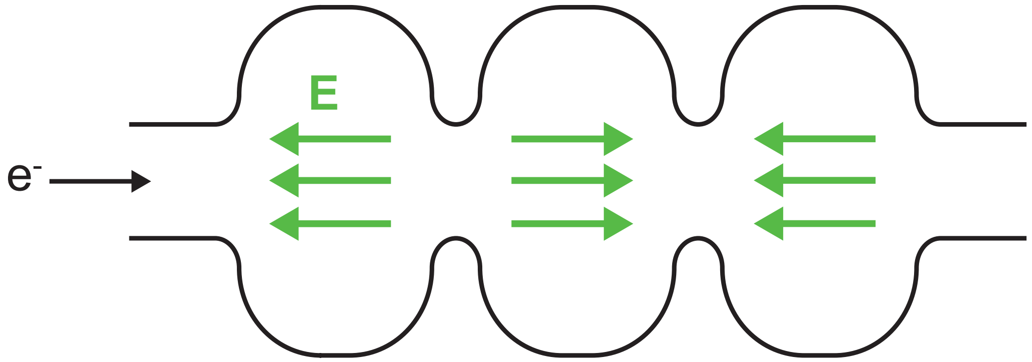

Figure 1.1: Schematic of a simple standing wave accelerator. The electron beam indicated by $\mathbf{e}^-$ travels along the central axis and is accelerated by the electric field $\mathbf{E}$. This schematic shows the π mode, where the field orientation changes in each cell. The field oscillates at a frequency f determined by the cavity geometry. In this configuration, the electron travels the distance of a cell (one period) in a half cycle of the oscillation such that the field is always in the correct orientation to accelerate the electron.

The cavity fields must be excited by an external source at the appropriate frequency. The input power required is dependent on the quality factor Q and shunt impedance of the cells as well the degree of coupling between the source and the cavity, which all determine the amount of input RF power that is ultimately transferred to the beam. Multiple cycles are required for the cells to reach full field, known as the fill time. This fill time sets the minimum source pulse length and is one limiting factor of how quickly a pulsed accelerator can operate (the repetition rate). These parameters are discussed in detail in 2.2.1. In general, standing-wave accelerators have a narrower bandwidth and require longer fill times compared to traveling-wave accelerators, but have higher shunt impedances.

1.3.2 Gradient and breakdown

An important performance metric of an accelerator is the acceleration gradient: the amount of energy a particle gains per unit distance. In the simplest picture, the energy gained in 1 m in a 1 V/m electric field is 1 eV. This would correspond to a gradient of 1 eV/m. In reality, the electric field on-axis is not a single value and the gradient must be calculated more thoroughly.

Modern RF accelerators operate in the range of 1–35 MeV/m, with some photocathode guns reaching 100 MeV/m [1]. The maximum achievable gradient is limited by vacuum breakdowns, which are related to pulse length and surface heating. In a breakdown event, a large amount of stored electrical energy is suddenly dissipated, which disrupts the vacuum and can cause material damage [15, 16]. Determining the exact causes of vacuum breakdown is still an area of active research. Recent results have shown that breakdown is heavily related to the surface magnetic field and pulsed heating of an accelerator structure [17, 18], which is discussed further in Section 2.2.1. Experiments have also shown that the threshold for breakdowns scales as the surface electric field, E_s,

$$E_s \propto \frac{f^{1/2}}{\tau^{1/4}} \tag{1.3}$$

where f is the frequency and τ is the pulse length. This is a rough scaling which is complicated by many factors, but has been shown to hold for a range of different existing structures [19, 20, 21]. The surface and on-axis electric fields for a given mode are linked, and therefore a limit in the surface field also implies a limit in the on-axis field and by extension the gradient. Even with advancements in cavity design, the peak surface field is typically at least twice the magnitude of the peak on-axis field. Therefore, a large amount of research aimed at reaching higher accelerating gradients is focused on raising E_s.

The accelerating gradient directly impacts the quality of a particle beam, especially in the case of electron guns. When electrons are sub-relativistic, beam quality degrades due to space charge forces. At relativistic speeds, space charge forces are largely negligible for the bunch charges of interest. Emittance growth during the time between emission to injection into an accelerator must be minimized for a high quality electron source. Increasing the gradient to achieve relativistic speeds more quickly is a promising method to create high brightness, low emittance sources.

1.3.3 Frequency scaling

Most existing accelerators operate in a few frequency ranges or bands in the microwave range from hundreds of MHz to tens of GHz. At these frequencies, high power sources are readily available and efficient.[2] However, the maximum surface fields and gradients are not sufficient for many future accelerator facility goals. Moving to higher frequency cavities can provide improvements on multiple fronts. The increased frequency f directly leads to an increased maximum surface field E_s before breakdown. The pulse length τ decreases because the cycle length is inherently shorter, which also results in increased E_s as seen in Equation 1.3.

Additional frequency scalings provide further benefits. The shunt impedance—which characterizes the strength of the accelerating field compared to the dissipated power—scales as $f^{1/2}$ and the dissipated power per unit length decreases as $f^{-1/2}$. As a result, fill time is decreased, the cavities can be powered more efficiently, and there is less pulsed heating. These factors combined indicate that high frequency accelerators could be operated at higher repetition rates than current microwave-range accelerators for the same gradient. The reduction in pulsed heating also indicates that the cavities may experience fewer breakdown events.

Standing-wave accelerators as described in this section cannot be scaled indefinitely. Above a certain frequency, it is no longer feasible to build normal conducting metallic resonant cavities because the metal conductivity begins to limit their performance. It also becomes challenging to transport and couple power through metallic waveguides, and high power narrowband sources are not readily available. Accelerators based near-infrared (NIR) and optical techniques have been developed to utilize available laser sources. These techniques provide many benefits but are subject to their own practical limitations, as discussed in the next section. In very high frequency accelerators, the short RF cycle also limits the achievable bunch charge.

THz-based accelerators utilize the benefits of frequency scaling while still being able to leverage well-developed techniques used in the microwave regime. The THz frequencies of interest fall between the microwave and NIR ranges, roughly 0.1 to a few THz. At the low end of this range, it is possible to use normal conducting accelerator cavities and use conventional waveguide transport.

1.4 Current state of the art

High brightness, low emittance electron accelerators are in high demand and as a result there are a variety of approaches researchers are taking to develop them. This section summarizes

---

[2] For example, the SLAC 5045 S-band (2.856 GHz) klystron operates with a peak output power of 65 MW with 3.5 μs pulses and 45% efficiency [22].

the current state of the art and recent results at the time of writing. It also briefly reviews the relative advantages and disadvantages of several leading approaches.

1.4.1 Electron source research

To date, the highest performing electron sources are photocathodes. The invention of photocathodes proved to be a breakthrough for particle accelerator development. Much of their performance is determined by the input laser pulse, which gives a high degree of control in shaping the beam and setting the bunch charge. Photocathodes regularly achieve emittances below 1 mm-mrad [1, 23, 19]. Current research is focused on improving this emittance further by reducing the mean transverse energy (MTE) of the emitted particles [24]. A drawback of some photocathodes is limited quantum efficiency (QE), meaning they require high laser pulse energies for useful bunch charges. In other cases, the response time of the material limits the possible repetition rate. Extensive research is being conducted on cathode materials that would simultaneously optimize the MTE, QE, and response time for high brightness beams [25, 26].

Unlike photocathodes, field emission sources do not have an external driver separate from the cavity field and thus the emittance is largely determined by the cathode geometry. Research into field emission sources is primarily focused on improved cathode materials and fabrication. The use of nano-emitters is a highly promising avenue to control the bunch emittance [27, 12, 13]. Researchers are also investigating novel materials [28] to provide bunches with very low energy spreads, an important parameter for microscopy applications. Field emission sources are particularly attractive for integrating into high frequency accelerating cavities because the emission timing is set by the cavity field. Thus, there is no issue with controlling the relative phasing between emission and the accelerating field, which can be especially challenging at high frequency.

1.4.2 Methods of high gradient acceleration

There are a number of techniques under study for high gradient acceleration. Techniques like plasma wakefield acceleration and direct laser acceleration have been developed for decades. Both techniques are based on accelerating the electrons with some high energy source other than a cavity field.

Plasma wakefield acceleration (PWA) is currently the leading method and has demonstrated multi-GeV/m gradients [29, 30, 31, 32]. These devices are capable of significant acceleration performance, including producing GeV electron beams and using multiple acceleration stages. The acceleration is provided by wakes in a mediating plasma generated by either a laser pulse or a charged particle beam. Though PWA has demonstrated high gradient acceleration, there are still challenges in reaching the performance required for various applications. Plasma instabilities can introduce problems with accelerator control, repetition rate, and stability. In the laser-driven case, the laser powers required are relatively high and are not widely available or efficient.

Direct laser acceleration (DLA) has not yet achieved similar performance. Thus far, experiments have seen small amounts acceleration of portions of an electron bunch [33, 34, 35, 36]. DLA uses a high-power laser pulse co-propagating with an electron beam to transfer energy. These devices are attractive because they are compact and the laser technology required is well-developed. However, they are fundamentally limited in the maximum achievable bunch charge by the laser wavelength. There are also challenges with timing and alignment precision between the two pulses that limit the performance in current experiments.

Improvements in laser-generated THz sources have also made it possible to accelerate and manipulate electron beams directly from a THz field [37, 38, 39, 40, 41]. These experiments operate by overlapping the paths of an input electron beam and a THz beam. In the interaction region, the strong THz field accelerates the electrons. Thus far, these experiments have been based on photocathodes and use the THz pulse to accelerate the photocathode-produced beam. Recent experiments have shown promising results demonstrating multi-stage acceleration [41]. The same laser pulse can be used to generate both the electron beam and the THz pulse, which simplifies matching the timing of the two pulses. It is expected that this method could achieve GeV/m-scale gradients with mJ THz pulses.

In the conventional accelerator realm, superconducting RF (SRF) and cooled normal conducting RF (NCRF) cavities are both candidates for high gradient acceleration. Superconducting structures can achieve much higher Q values which reduces losses and increases efficiency. Cooling NCRF structures reduces pulsed heating and allows the structures to reach higher gradients than would be possible at room temperature. Pulsed SRF experiments have shown gradients of roughly 50 MeV/m in the cavities, though with limited repetition rates [42]. The true gradient is limited by the filling factor of the cryomodules required to cool the cavities: the cavities only occupy a fraction of the overall length. Cooled NCRF experiments have demonstrated surface fields up to 500 MV/m, which indicates that gradients of hundreds of MeV/m should be possible [43]. There is also significant work underway to build continuous (CW) SRF accelerators [44, 45]. CW operation is preferred for applications that require long pulses. Experiments thus far have achieved gradients on the order of a single MeV/m in continuous operation. The primary limitation in these cases is the cost and complexity of cooling. In the case of pulsed SRF and cooled NCRF, the cryogenics are costly but available. However, at higher gradients, the required cryogenic cooling power is substantially increased. Efficient cooling for CW operation is an area of active research.

Room temperature X-band (8–12 GHz) NCRF structures can reach gradients of up 100 MeV/m with limited repetition rate. As discussed in the previous section, this gradient is fundamentally limited by the breakdown threshold. Recent experiments using THz-frequency NCRF structures have demonstrated gradients of up to 230 MeV/m with limited input power [46]. Experiments with wakefield-driven, THz traveling-wave structures have also demonstrated gradients of up to 300 MeV/m with 1.5 GV/m surface fields [47]. These results indicate that THz structures can be used to greatly increase the gradient while avoiding breakdowns. The achieved gradient in these experiments is thus far limited only by the available source power. Fully realized THz-based accelerators will require further development of high power, high efficiency THz sources.

1.5 Thesis overview

This thesis presents the development of a high gradient, THz-driven electron gun and beam characterization assembly. The following chapters include details on the gun cell design, fabrication, and low power testing. Modeling of the electron beam dynamics and transport are discussed as well as diagnostics developed to characterize the beam.

The standing-wave gun consists of two cells with a copper field emission cathode. The cells are designed to operate in the π mode at 110.081 GHz and are expected to produce 365 keV electrons after 1.6 mm of acceleration with 500 kW of input power. This structure is designed to eventually produce relativistic electrons with just 1 MW of input power supplied by a 110 GHz gyrotron oscillator. The gun assembly includes a horn and mode converter to power the cells. A solenoid focusing magnet was designed to control the divergence of the beam at the output of the gun assembly.

Multiple diagnostics were developed to measure the electron beam. A dipole magnet energy spectrometer assembly was designed to measure the energy spread. The dipole introduces an energy-based displacement which can be measured on a scintillating phosphor screen coupled to a microchannel plate detector (MCP). A second MCP and phosphor screen are included on-axis for measuring the beam size. The dipole current can be reversed to direct the beam into a Faraday cup to measure the current. The Faraday cup can also be used to monitor for dark current from breakdown events. Both the dipole and solenoid are electromagnets, allowing for focusing and characterization over a range of input powers and electron energies.

The theory of electromagnetic cavities, electron guns, and field emission is discussed in Chapter 2. Chapter 3 presents the design and modeling of the electron gun including both electromagnetic and particle simulations. Cold test measurements validating the electromagnetic performance of the cells are given in Chapter 4. Details on the fabrication and tuning of the gun structures are also included in Chapter 4. The full beam characterization assembly is discussed in Chapter 5 including the design and modeling of the electron beam diagnostics. Measurements under vacuum are also included in Chapter 5. Chapter 6 summarizes the findings of this work and outlines opportunities for future research.

Chapter 2

Background

This chapter introduces the fundamental physics required to describe field emission electron guns. Emphasis is placed on the equations, quantities, and definitions that are most relevant for the case of standing-wave, linear electron accelerators.

2.1 Theory of electromagnetic resonators

Electromagnetic fields are described by Maxwell's equations

$$\begin{aligned} \nabla \cdot \mathbf{D} &= \rho \\ \nabla \times \mathbf{H} - \frac{\partial \mathbf{D}}{\partial t} &= \mathbf{J} \\ \nabla \times \mathbf{E} + \frac{\partial \mathbf{B}}{\partial t} &= 0 \\ \nabla \cdot \mathbf{B} &= 0 \end{aligned} \tag{2.1}$$

where $\mathbf{J}$ is the electric current density, ρ is the electric charge density, and $\mathbf{D} = \epsilon\mathbf{E}$ and $\mathbf{B} = \mu\mathbf{H}$ are the electric and magnetic flux densities. Here, ϵ is the electric permittivity and μ is the magnetic permeability. Both $\mathbf{B}$ and $\mathbf{H}$ are both commonly referred to as 'magnetic field' for practical purposes in different contexts. They can be distinguished by their units. Discussing $\mathbf{B}$ in units of Teslas is most useful in the case of magnets, such as in Chapter 5. The magnetic field $\mathbf{H}$ in units of Amperes/meter is the 'magnetic field' of interest in this section.

Generally, the time dependence of electromagnetic fields has the form $e^{j\omega t}$ which allows Equations 2.1 to be rewritten in terms of the angular frequency ω as

$$\begin{aligned} \nabla \cdot \mathbf{D} &= \rho \\ \nabla \times \mathbf{H} &= j\omega\mathbf{D} + \mathbf{J} \\ \nabla \times \mathbf{E} &= -j\omega\mathbf{B} \\ \nabla \cdot \mathbf{B} &= 0 \end{aligned} \tag{2.2}$$

In a source-free region, these become

$$\nabla \times \mathbf{E} = -j\omega\mu\mathbf{H} \tag{2.3}$$
$$\nabla \times \mathbf{H} = j\omega\epsilon\mathbf{E} \tag{2.4}$$

which can be used to derive the Helmholtz wave equations

$$\nabla^2\mathbf{E} + \omega^2\mu\epsilon\mathbf{E} = 0 \tag{2.5}$$
$$\nabla^2\mathbf{H} + \omega^2\mu\epsilon\mathbf{H} = 0. \tag{2.6}$$

Wave propagation can thus be characterized by the angular frequency ω and wavenumber $k = \omega\sqrt{\mu\epsilon}$. These values determine the phase velocity of the wave

$$v_p = \frac{\omega}{k} = \frac{1}{\sqrt{\mu\epsilon}}. \tag{2.7}$$

Waves traveling in an infinite vacuum have a phase velocity equal to the speed of light, $v_p = c$. The vacuum permeability and permittivity μ_0 and ϵ_0 are thus related to the speed of light as $c = \frac{1}{\sqrt{\mu_0\epsilon_0}}$. Wave propagation in the presence of losses is described by the complex propagation constant

$$\gamma = \alpha + j\beta = j\omega\sqrt{\mu\epsilon} \tag{2.8}$$

where α is the attenuation constant and β is the phase constant. Equation 2.5 can be rewritten as

$$\nabla^2\mathbf{E} - \gamma^2\mathbf{E} = 0. \tag{2.9}$$

For a wave traveling in z, the solutions have the form

$$E\left(z\right) = E^+e^{-\gamma z} + E^-e^{\gamma z} \tag{2.10}$$

where E^+ and E^- are the amplitudes of the forward- and backward-traveling waves.

The electric and magnetic fields of a wave can be broken up into transverse and longitudinal components with respect to the direction of propagation. Neglecting material losses, a general form is

$$\mathbf{E}\left(x,y,z\right) = \left[\mathbf{E}_t\left(x,y\right) + \hat{z}E_z\left(x,y\right)\right]e^{-j\beta z} \tag{2.11}$$
$$\mathbf{H}\left(x,y,z\right) = \left[\mathbf{H}_t\left(x,y\right) + \hat{z}H_z\left(x,y\right)\right]e^{-j\beta z} \tag{2.12}$$

where the propagation direction is chosen to be $\hat{z}$. These forms can then be used with Equations 2.3 and 2.4 to write the transverse components in terms of the longitudinal components. In waveguides and resonators, the boundary conditions give rise to eigenmodes of these equations. Field solutions exist at discrete frequencies determined by the dimensions of the structure. These modes are classified by their transverse components; transverse magnetic (TM) modes have $H_z = 0$, and transverse electric (TE) modes have $E_z = 0$. When two conductors are present, such as in a coaxial waveguide, transverse electromagnetic (TEM) modes with $E_z = H_z = 0$ are supported.

In the case of accelerator cavities and electron guns, it is best to express these equations in cylindrical coordinates. The transverse components are

$$E_\rho = \frac{-j}{k_c^2}\left(\beta\frac{\partial E_z}{\partial\rho} + \frac{\omega\mu}{\rho}\frac{\partial H_z}{\partial\phi}\right) \tag{2.13}$$

$$E_\phi = \frac{-j}{k_c^2}\left(\frac{\beta}{\rho}\frac{\partial E_z}{\partial\phi} - \omega\mu\frac{\partial H_z}{\partial\rho}\right) \tag{2.14}$$

$$H_\rho = \frac{j}{k_c^2}\left(\frac{\omega\epsilon}{\rho}\frac{\partial E_z}{\partial\phi} - \beta\frac{\partial H_z}{\partial\rho}\right) \tag{2.15}$$

$$H_\phi = \frac{-j}{k_c^2}\left(\omega\epsilon\frac{\partial E_z}{\partial\rho} + \frac{\beta}{\rho}\frac{\partial H_z}{\partial\phi}\right) \tag{2.16}$$

where $k_c^2 = k^2 - \beta^2$. Combined with the wave equations (2.5 and 2.6), these components give general solutions for TE and TM eigenmodes in the transverse plane. The solutions are best written in terms of Bessel functions. The transverse description applies to both waveguides and cavities. In the cavity case, there are also reflective boundary conditions in the z direction which give rise to a standing wave that is a superposition of the backward and forward propagating waves.

A given mode is characterized by the number of nodes/variations in each coordinate direction. This is expressed using indices $nm\ell$ which correspond to azimuthal, radial, and longitudinal variations, respectively, following the naming convention used in [48]. The indices n and m describe the root of the Bessel function in the transverse plane, $J_n\left(p_{nm}\right) = 0$ for TM modes and $J_n'\left(p_{nm}'\right) = 0$ for TE modes. Here J_n' is the derivative of J_n. These determine the propagation constants and β values for the modes. For TM modes

$$\beta_{nm} = \sqrt{k^2 - k_c^2} = \sqrt{k^2 - \left(\frac{p_{nm}}{a}\right)^2} \tag{2.17}$$

and for TE modes

$$\beta_{nm} = \sqrt{k^2 - k_c^2} = \sqrt{k^2 - \left(\frac{p_{nm}'}{a}\right)^2} \tag{2.18}$$

where a is the radius of the cavity or waveguide.

In a cavity, the field in the longitudinal direction varies sinusoidally as $A\sin\left(\beta_{nm}z\right)$ with an arbitrary amplitude A. To satisfy the $E_t = 0$ boundary condition at the length of the cavity L,

$$\beta_{nm}L = \ell\pi \tag{2.19}$$

giving the longitudinal index ℓ.

Eigenmodes are often discussed in terms of the frequency $f = \frac{\omega}{2\pi}$ rather than the angular frequency ω. Values of f are given in units of Hz or cycles per second rather than purely per second. It is also a convenient quantity for calculating the wavelength and energy. The photon energy is given by $E = hf$, where h is Planck's constant, and the free space wavelength λ is defined by $c = f\lambda$.

The resonant frequencies are determined by the propagation constant and the material properties of the structure. They can be written as

$$f_{nm\ell} = \frac{c}{2\pi\sqrt{\mu_r\epsilon_r}}\sqrt{\left(\frac{p_{nm}}{a}\right)^2 + \left(\frac{\ell\pi}{L}\right)^2} \tag{2.20}$$

$$f_{nm\ell} = \frac{c}{2\pi\sqrt{\mu_r\epsilon_r}}\sqrt{\left(\frac{p'_{nm}}{a}\right)^2 + \left(\frac{\ell\pi}{L}\right)^2} \tag{2.21}$$

for TM and TE modes, respectively. In vacuum, $\mu_r = \epsilon_r = 1$.

Cavity modes are also characterized by their quality factor Q. The Q value is a measure of the energy stored versus the power dissipated in the cavity. Accelerator cavities are typically made from a high conductivity metal and operated under vacuum, and thus the Q value is limited by the wall losses. The intrinsic Q value of the mode is referred to as the 'unloaded' quality factor Q_0, given by

$$Q_0 = \frac{\omega_0 W}{P} \tag{2.22}$$

where ω_0 is the angular frequency of the mode, W is the time-averaged stored energy in the electric and magnetic fields, and P is the power dissipated in the walls. In a practical accelerator, the Q value determines the power needed to drive the cavities and the time it takes to reach the maximum field.

Scattering or S parameter measurements can be used to observe the cavity resonances. The S parameters are elements of a scattering matrix which relates input and output voltage waves at an arbitrary number of ports. They are typically written as S_{ji} where i is the driving port and j is the receiving port. Thus the reflected signal at port 1 is measured as S_{11}, and transmission from port 1 to port 2 is S_{21}. The S parameters can be measured using a network analyzer and contain information about both the magnitude and phase of the signal. Cavity resonances appear as peaks in the transmission S_{21} and corresponding dips in the reflection S_{11}. The width of the resonances in the reflection signal can be used to calculate the loaded Q value Q_L and the coupling coefficient β_c, which are discussed in the next section (Equation 2.24).

2.2 Standing wave electron gun principles

2.2.1 Accelerator description

A standing wave accelerator is based on cavity eigenmodes. An accelerator cavity is typically made of multiple cells connected by openings along the beam axis, called irises. The beam travels along the z axis from one cell to another and gains energy from the on-axis electric field. Since the E_z component is responsible for acceleration, accelerator cavities use TM modes. Two primary operating configurations are referred to as the 'o mode' and the 'π mode'. The number of possible modes is equal to the number of cells in the structure. In the o mode, the neighboring cells are in phase with each other and thus electric field oriented in the same direction. In the π mode, the cells are 180 degrees out of phase with their neighbors and the E field orientation flips from one cell to the next. This is the operating mode illustrated in Figure 1.1. The choice of operating mode, accelerating gradient, and beam energy determine the length of the cells and the irises. A series of cells must be designed such that the particle reaches the next cell when the field is in the correct orientation. Arriving too early or too late decelerates the particle. This is illustrated in Figure 2.1. The range of launch phases that successfully result in net energy gain contributes to the energy spread of a given bunch.

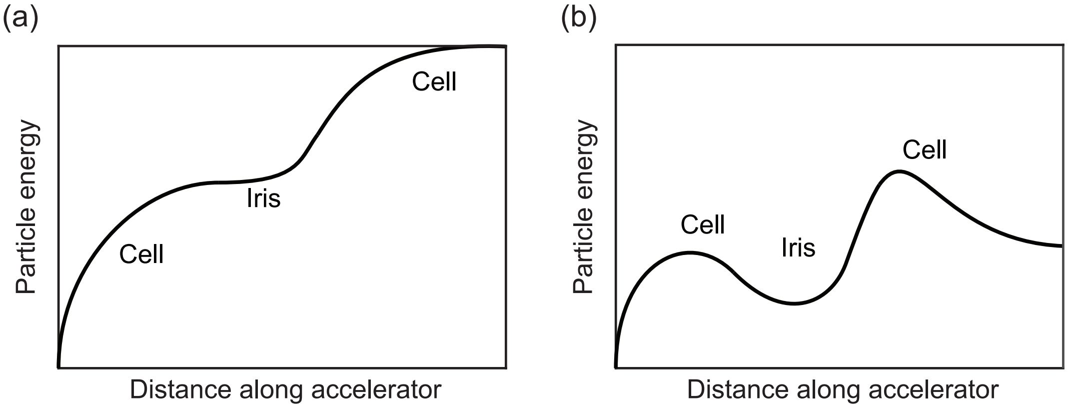

Figure 2.1: Schematic of particle energy as it traverses two accelerator cells. (a) Optimal acceleration, where the particle arrives at the iris before the field changes orientation in the first cell. (b) Sub-optimal acceleration. Here, the particle is decelerated because it does not traverse the cell within a half cycle. Depending on the phase, the particle may still leave the accelerator with some net energy. In other cases, it will be accelerated back into the cathode or attracted to the cavity wall.

Standing wave accelerator cavities in their simplest form can be simple pillboxes as described in the previous section. However, an optimized accelerator cavity can have many shapes depending on the performance requirements. Cavity shaping influences the relative field strengths on surfaces compared to on-axis. These factors affect the efficiency of acceleration and determine values like the shunt impedance and quality factor.

The shunt impedance is a measure of the accelerating field compared to the power dissipated in the cavity. The expression is for the shunt impedance per unit length is

$$r_s = \frac{E_a^2}{dP/dz} \tag{2.23}$$

where E_a is the peak accelerating field and dP/dz is the power dissipated per unit length. Thus the shunt impedance determines the input power necessary to reach a certain accelerating field, and by extension a desired accelerating gradient.

Power is supplied to the cavities from an external source in a waveguide mode. The frequency of this source must correspond to the resonant frequency of the accelerating mode. The coupling between the source waveguide and the cavity is described by the coupling coefficient β_c. This coupling coefficient determines the loaded quality factor Q_L, given by

$$Q_L = \frac{Q_0}{1+\beta_c}. \tag{2.24}$$

The value of Q_L is experimentally measurable and combines the intrinsic cavity properties with those of the feeding network.

The cavities must be powered for many cycles before reaching the steady state standing-wave field. The fill time characterizes the time necessary for the fields to reach $1/e$ of their steady state magnitudes. For a standing-wave structure, the expression is

$$t_F = \frac{2Q_L}{\omega} = \frac{2Q_0}{(1+\beta_c)\,\omega}. \tag{2.25}$$

This fill time determines the necessary source pulse length τ and limits the repetition rate of the accelerator. Many applications require high repetition rate, and thus increasing Q_L and decreasing the fill time are both important design goals.

The source pulse length τ also determines the pulsed heating of the structure. RF pulsed heating occurs when the magnetic field on a conducting surface induces eddy currents that result in Ohmic heating of the material. The timescale of the heating is determined by the pulse length. When the timescale is short compared to the rate of thermal expansion, stresses occur in the material. The cyclic nature of the stress, determined by the repetition rate of the accelerator, can eventually lead to material damage and failure. Recent studies have shown that vacuum breakdowns are tied to pulsed heating [17, 18, 49, 50]. Since vacuum breakdowns are a limiting factor in achieving high gradient acceleration, using shorter pulse lengths could provide access to new operating regimes.

2.2.2 Tuning

The frequency of a resonant cavity mode depends on the enclosed volume, the surface profile, and the material enclosed. Perturbations to the surface/volume are used to shift the frequency and tune accelerator cavities. Material changes such as pumping a cavity down to vacuum from air also change the frequency. It is possible in both cases to calculate the perturbed frequency in terms of the unperturbed values.

In general terms, the unperturbed fields and frequency in a volume V_0 are can be described by

$$\nabla \times \mathbf{E_0} = -j\omega_0\mu\mathbf{H_0} \tag{2.26}$$

$$\nabla \times \mathbf{H_0} = j\omega_0\epsilon\mathbf{E_0}. \tag{2.27}$$

If the surface enclosing the volume is perturbed by ΔS, producing a perturbed volume $V = V_0 + \Delta V$, the perturbed fields in V can be written as

$$\nabla \times \mathbf{E} = -j\omega\mu\mathbf{H} \tag{2.28}$$

$$\nabla \times \mathbf{H} = j\omega\epsilon\mathbf{E}. \tag{2.29}$$

These expressions can be combined to find $\omega - \omega_0$ due to the perturbation. Multiplying the complex conjugate of Equation 2.26 by $\mathbf{H}$ and multiplying Equation 2.29 by $\mathbf{E}_0^*$ gives

$$\mathbf{H} \cdot \nabla \times \mathbf{E}_0^* = j\omega_0\mu\mathbf{H} \cdot \mathbf{H}_0^* \tag{2.30}$$

$$\mathbf{E}_0^* \cdot \nabla \times \mathbf{H} = j\omega\epsilon\mathbf{E}_0^* \cdot \mathbf{E}. \tag{2.31}$$

The vector identity

$$\nabla \cdot (\mathbf{A} \times \mathbf{B}) = (\nabla \times \mathbf{A}) \cdot \mathbf{B} - (\nabla \times \mathbf{B}) \cdot \mathbf{A} \tag{2.32}$$

can be applied when subtracting Equations 2.30 and 2.31 to get

$$\nabla \cdot (\mathbf{E}_0^* \times \mathbf{H}) = j\omega_0\mu\mathbf{H} \cdot \mathbf{H}_0^* - j\omega\epsilon\mathbf{E}_0^* \cdot \mathbf{E}. \tag{2.33}$$

The same process can be applied to Equation 2.28 and the complex conjugate of Equation 2.27 to get a second relation

$$\nabla \cdot (\mathbf{E} \times \mathbf{H}_0^*) = -j\omega\mu\mathbf{H}_0^* \cdot \mathbf{H} + j\omega_0\epsilon\mathbf{E} \cdot \mathbf{E}_0^*. \tag{2.34}$$

Adding these equations and integrating over V gives

$$\int_V \nabla \cdot (\mathbf{E} \times \mathbf{H}_0^* + \mathbf{E}_0^* \times \mathbf{H})\, dv = -j\,(\omega - \omega_0) \int_V (\epsilon\mathbf{E} \cdot \mathbf{E}_0^* + \mu\mathbf{H} \cdot \mathbf{H}_0^*)\, dv \tag{2.35}$$

which can be changed to a surface integral using the divergence theorem. Using the surface integral, the electric field boundary conditions $\hat{n} \times \mathbf{E} = 0$ on the perturbed surface S and $\hat{n} \times \mathbf{E}_0 = 0$ on S_0 can be applied. The result reduces to

$$\omega - \omega_0 = \frac{-j \oint_{\Delta S} (\mathbf{E}_0^* \times \mathbf{H}) \cdot d\mathbf{s}}{\int_V (\epsilon\mathbf{E} \cdot \mathbf{E}_0^* + \mu\mathbf{H} \cdot \mathbf{H}_0^*)\, dV}. \tag{2.36}$$

To get an expression purely in terms of the unperturbed values, it is necessary to assume ΔS is small enough such that $\mathbf{E} \approx \mathbf{E}_0$ and $\mathbf{H} \approx \mathbf{H}_0$. This gives

$$\omega - \omega_0 \approx \frac{-j \oint_{\Delta S} (\mathbf{E}_0 \times \mathbf{H}_0) \cdot d\mathbf{s}}{\int_V \left(\epsilon \left|\mathbf{E}_0\right|^2 + \mu \left|\mathbf{H}_0\right|^2\right) dv}. \tag{2.37}$$

Applying Poynting's theorem (power balance), this can be rewritten as [48]

$$\frac{\omega - \omega_0}{\omega_0} \approx \frac{\int_{\Delta V} \left(\mu \left|\mathbf{H}_0\right|^2 - \epsilon \left|\mathbf{E}_0\right|^2\right) dv}{\int_{V_0} \left(\mu \left|\mathbf{H}_0\right|^2 + \epsilon \left|\mathbf{E}_0\right|^2\right) dv}. \tag{2.38}$$

In terms of the stored energies, this is

$$\frac{\omega - \omega_0}{\omega_0} = \frac{\Delta W_m - \Delta W_e}{W_m + W_e} \tag{2.39}$$

where ΔW_m and ΔW_e are the changes in the cavity magnetic and electric stored energies and $W_m + W_e$ is the total stored energy. Perturbations in the shape can raise or lower the frequency depending on whether they increase or decrease the volume as well as their relative effect on the magnetic and electric stored energies. This method was used to tune the frequency of the gun cells presented in this thesis (see Section 4.5.4).

The same process can be applied to derive the frequency shift due to a material perturbation. Material perturbations can be described as a change in the permittivity $\Delta\epsilon$ and permeability $\Delta\mu$. With initial values $\mathbf{E}_0$, $\mathbf{H}_0$, ω_0, and V_0, the result is [48]

$$\frac{\omega - \omega_0}{\omega_0} \approx \frac{-\int_{V_0} \left(\Delta\epsilon \left|\mathbf{E}_0\right|^2 + \Delta\mu \left|\mathbf{H}_0\right|^2\right) dv}{\int_{V_0} \left(\epsilon \left|\mathbf{E}_0\right|^2 + \mu \left|\mathbf{H}_0\right|^2\right) dv} \tag{2.40}$$

or in terms of the stored energy,

$$\frac{\omega - \omega_0}{\omega_0} = -\frac{\Delta W_m + \Delta W_e}{W_m + W_e}. \tag{2.41}$$

From these expressions, it is clear that an increase in either ϵ or μ from a material change will lower the resonant frequency.

2.2.3 Electron guns

Standing wave electron guns combine a cathode with accelerating cavities to generate bunches of electrons. The cathode is located in a cell or half cell such that electrons emitted from the cathode at the correct phase of the electric field will be quickly accelerated away from the surface. Particles emitted at incorrect phasing will not gain enough energy to be accelerated beyond this first cell. This creates an inherent bunch length limited by the $1/(2f)$ period of the field.

In a photoemission gun, the emission is driven by an input laser pulse. This timing of the pulse must be synchronized with the phase of the electric field. In a field emission gun, as introduced in Section 1.2.2, the electric field in the cavity is responsible for the emission. This limits difficulties with the phasing and timing. The emission varies directly with the electric field strength over the course of each cycle. The cathode and cavity geometry can be designed such that the majority of emission occurs at the optimal phase for acceleration without any further external control.

2.3 Field emission

Electrons in a metal can be described as a uniform Fermi gas. In the free electron model, electrons exist in a potential well with a density of states described by Fermi-Dirac statistics.

The supply function for electrons incident on the barrier is

$$N(T, E_F, W)\, dW = 4\pi mkTh^{-3} \times \ln\left[1 + \exp\left(\frac{-(W - E_F)}{kT}\right)\right] dW \tag{2.42}$$

where m is the electron mass, T is the absolute temperature, E_F is the Fermi energy for the metal, k is Boltzmann's constant, and h is Planck's constant [51]. W is the kinetic energy of the motion normal to the metal surface, given by

$$W = \frac{p(x)^2}{2m} + V(x) \tag{2.43}$$

where $p(x)$ is the electron momentum normal to the surface and $V(x)$ is the potential energy. In the presence of an applied field E, the potential energy is assumed to be

$$\begin{aligned} V(x) &= -\frac{e^2}{4x} - eEx && \text{for } x > 0 \\ &= -W_a && \text{for } x < 0 \end{aligned} \tag{2.44}$$

where W_a is the potential energy inside the metal. This potential is illustrated in Figure 2.2. The potential near $x = 0$ is assumed to smoothly connect the two regions.

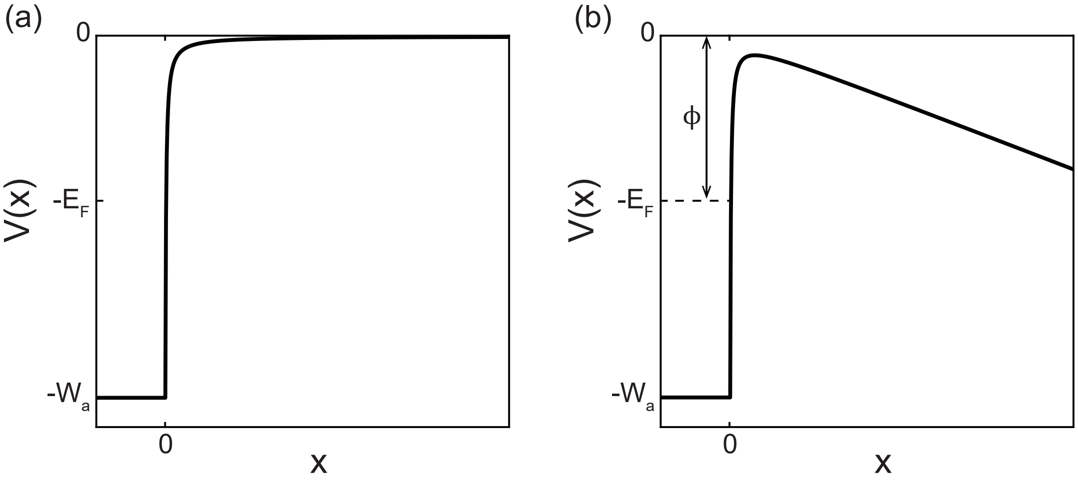

Figure 2.2: (a) Potential in the case with no applied field ($E = 0$). (b) Potential when $E \neq 0$. The applied field tilts the barrier making it possible for electrons to tunnel out of the surface. Here, the work function ϕ is equal to the Fermi energy E_F.

This description can be used to calculate the probability of an electron tunneling through the barrier with a given temperature T and field strength E. Murphy and Good [51] derived expressions for the current in two regimes: the high temperature, low field region (thermionic emission) and the low temperature, high field region (field emission). The current in the field emission region is given by

$$j = \frac{E^2}{16\pi^2 \phi t^2} \left[\frac{\pi ckT}{\sin(\pi ckT)} \right] \exp\left(-\frac{4\sqrt{2}\phi^{\frac{3/2}{v}}}{3E} \right) \tag{2.45}$$

where ϕ is the work function of the material and t and v are dimensionless elliptic functions of E and ϕ. At low temperature satisfying $\pi ckT/\sin(\pi ckT) \approx 1$, Equation 2.45 reduces to the Fowler-Nordheim equation for cold field emission [52]. In practical units, this can be written as

$$j_F = \frac{1.54 \times 10^{-6} \times 10^{4.52\phi^{-0.5}} E^2}{\phi} \exp\left(-\frac{6.53 \times 10^9 \phi^{1.5}}{E} \right) \ \left[\mathrm{A/m^2}\right] \tag{2.46}$$

with E in units of V/m and ϕ in units of eV [53]. The current for a given emission area A_e can be written as

$$I_F = \frac{1.54 \times 10^{-6} \times 10^{4.52\phi^{-0.5}} A_e \beta^2 E^2}{\phi} \exp\left(-\frac{6.53 \times 10^9 \phi^{1.5}}{\beta E} \right) \ [\mathrm{A}]\,. \tag{2.47}$$

where β is the field enhancement factor over A_e. The field enhancement factor is a measure of the microscopically enhanced field value due to surface features versus the theoretically ideal field value. It can be expressed by

$$\beta = \frac{E_m}{E} \tag{2.48}$$

where E_m is the enhanced field and E is the ideal field. Field enhancement can arise both from microscopic irregularities in the material like surface roughness and from intentionally-designed features like nano-tips. Based on Schottky's conjecture, the total field enhancement $\beta = \beta_0 \beta_S$ where β_0 denotes the material contribution and β_S is the tip shape contribution [54, 55].

For a time-varying electric field as in an RF electron gun, the current will vary with the strength of the surface electric field throughout the RF cycle. It is also possible to calculate a time-averaged current assuming a field varying as $E_0 \sin(\omega t)$:

$$\begin{aligned} \bar{I}_F &= \frac{1}{T} \int_0^T I_F(t)\, dt \\ &= \frac{5.7 \times 10^{-12} \times 10^{4.52\phi^{-0.5}} A_e \left(\beta E_0\right)^{2.5}}{\phi^{1.75}} \exp\left(-\frac{6.53 \times 10^9 \times \phi^{1.5}}{\beta E_0} \right) \ [\mathrm{A}]\,. \end{aligned} \tag{2.49}$$

From Equation 2.47, it is clear that the emission will be maximized when the field is highest. Following a sinusoidally varying field, this occurs at $\omega t = \pi/2$ and $\omega t = 3\pi/2$. Only one of these phases will have the electric field oriented to accelerate emitted particles. This behavior is what limits the bunch length of an RF field emission electron gun and directly ties the emission to the correct phase for acceleration, as discussed in the previous section.

2.4 Electron beam physics

Describing the physics of an electron beam in a particle accelerator requires discussing the forces exerted on the particles by the externally applied fields as well as the interparticle interactions. This section will review the fundamental equations necessary to describe this behavior and introduce relevant quantities used to characterize beams in an accelerator.

2.4.1 Electron motion in electromagnetic fields

The Lorentz force on a single charged particle in the presence of electric and magnetic fields was given in Equation 1.2:

$$\mathbf{F} = q\left(\mathbf{E} + \mathbf{v} \times \mathbf{B}\right).$$

As described in Section 1.3, the force on the particle from the electric field is responsible for energy gain in an accelerator. The magnetic field acts perpendicular to the velocity and thus changes the trajectory of the particle without changing its kinetic energy. As a result, magnets are used to steer, focus, and bend particle beams within an accelerator.

When the energy of a particle approaches or exceeds its rest mass energy, equations for energy and momentum are described by the theory of special relativity. The rest mass energy of an electron is

$$E = m_e c^2 \approx 511 \text{ keV}. \tag{2.50}$$

Most electron accelerators generate beams with much higher energies, extending into the MeV and GeV ranges. Thus, beam dynamics in particle accelerators is described using relativistic equations. The momentum is given by

$$\mathbf{p} = \gamma m_e \mathbf{v} \tag{2.51}$$

where γ is the Lorentz factor

$$\gamma = \frac{1}{\left(1 - \beta^2\right)^{1/2}} \tag{2.52}$$

and $\beta = v/c$.

The equations of motion in electromagnetic fields can be derived in a variety of frameworks. These full derivations are beyond the scope of this thesis, but a few key equations will be presented here. The Lagrange function for a generalized potential is

$$L = T - U^* \tag{2.53}$$

where T is the kinetic energy and U^* is the velocity-dependent potential. The potential is determined by the electric and magnetic fields. A common formulation is to use a vector potential $\mathbf{A}$ where

$$\mathbf{B} = \nabla \times \mathbf{A} \tag{2.54}$$

which combined with Maxwell's equations (Equation 2.1) gives

$$\mathbf{E} = -\nabla\phi - \frac{\partial \mathbf{A}}{\partial t}. \tag{2.55}$$

Here, ϕ is the scalar potential which is related to the vector potential by the Lorenz gauge condition

$$\nabla \cdot \mathbf{A} + \frac{1}{c^2}\frac{\partial \phi}{\partial t} = 0 \tag{2.56}$$

It follows that for a relativistic charged particle in an electromagnetic field, the Lagrangian is

$$L = mc^2\left[1 - \left(1-\beta^2\right)^{1/2}\right] - q\phi + q\mathbf{V}\cdot\mathbf{A} \tag{2.57}$$

From this, the equations of motion can be derived in various coordinate systems and field conditions [56, 57].

2.4.2 Emittance

As introduced in Section 1.2.1, the emittance describes the area of the phase space distribution of an electron beam. The beam occupies a 6D phase space consisting of spatial coordinates x, y, and z, and momentum coordinates p_x, p_y, and p_z. In the absence of dissipative and nonlinear forces, the particles obey Liouville's theorem [58]. Liouville's theorem states that the density of particles in phase space remains constant, and thus for a fixed number of particles, the phase space volume they occupy also remains constant.

Liouville's theorem does not strictly hold when the interactions between particles are significant compared to the forces from external fields. When space charge forces are dominant (discussed in the following section), it is necessary to define a higher dimensional phase space. It is generally assumed that the intrabeam particle interactions can be neglected compared to the external fields when the interparticle distance is much smaller than a Debye length, defined by

$$\lambda_D = \left(\frac{\epsilon_0 m\gamma^3\tilde{v}_x^2}{q^2 n}\right)^{1/2} \tag{2.58}$$

where $\tilde{v}_x \ll c$ is the rms random velocity for a thermal distribution of particles and n is the particle number density [56].

Because of this conservation law, it is useful to describe a beam by its emittance rather than its physical size. Emittances can be defined in a number of ways. In the geometric case, the emittance is the area of the beam in the trace space planes as shown in Figure 2.3. The trace space plane uses x-x' rather than x-p_x, where x' is the angular divergence. As a beam propagates through a beam line, steering and focusing elements will change the orientation of the ellipse without changing its size. This is illustrated in Figure 2.3. As a result, the emittance is a more consistent measurement of the beam's properties than its spatial size. The boundary of this ellipse can be defined in multiple ways. A common choice is to use the standard deviation of the particle positions σ. Another is to choose the ellipse enclosing 95%

of the particles. Emittance can also be defined statistically using moments of the particle distribution in trace space. For example, the rms emittance in the x-x' plane is defined as

$$\bar{\epsilon}_x = \left(\overline{x^2}\;\overline{x'^2} - \overline{xx'}^2\right)^{1/2} \tag{2.59}$$

for a general particle distribution [56].

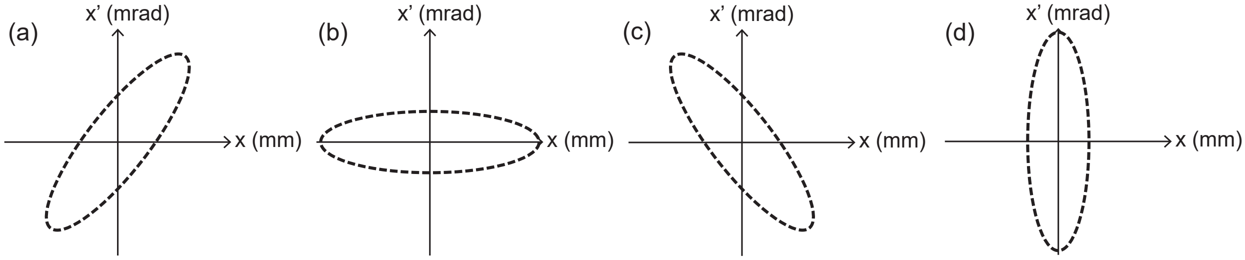

Figure 2.3: Example evolution of the beam distribution in the trace space x-x'. The x axis represents the spatial coordinates and y axis represents the angular coordinates or divergence x'. As the beam propagates through the accelerator, the spatial distribution can be focused and defocused, but this does not correspond to a change in the emittance. A diverging beam is shown in (a), (b) shows a beam with large spatial spread but low divergence, (c) shows a converging beam, and (d) shows a focused beam, where the spatial extent is minimized but divergence is maximized. In each case, the area of the ellipse is conserved.

The conservation of the trace space (geometric) emittance is only valid when the beam energy is not changing, such as passing through focusing magnets. During acceleration, the transverse geometric emittance shrinks as p_z grows. This is illustrated in Figure 2.4. It is useful to define a normalized transverse emittance that is invariant during acceleration. The normalized emittance is defined as

$$\epsilon_N = \beta\gamma\epsilon \tag{2.60}$$

which includes the relativistic β and γ.

In the case of electron sources, Liouville's theorem imposes a fundamental limit on the phase space area and therefore the minimum emittance. The phase space area of the bunch is set by the emitter and thus the emittance can not be reduced without advanced techniques like beam cooling or emittance exchange. This limit motivates much of the research in creating nano-emitters and developing photocathode materials with lower intrinsic emittance.

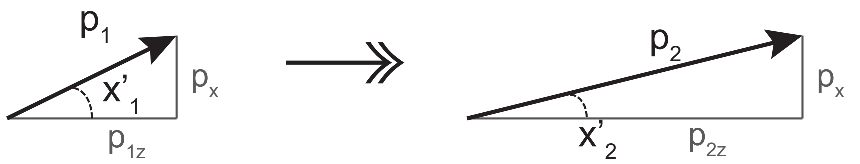

Figure 2.4: Example of how geometric emittance changes during acceleration. The longitudinal momentum p_z increases but the transverse component p_x does not change. This decreases the angle x' which would lead to a decrease in the geometric emittance.

2.4.3 Space charge

Charged particle beams produce electromagnetic fields called self-fields. These self-fields consist of competing electric and magnetic interactions from both the beam itself and its surroundings. The forces generated by the beam itself are called space charge forces and depend on the charge, current, distribution, and energy of the beam. Coulomb repulsion between like charges is counteracted by the focusing force of currents moving in parallel. A beam traveling within a metallic cavity experiences image charge forces from the walls. The net effect can cause beam degradation via emittance growth and energy loss.

Space charge forces are a major determinant of beam quality in certain regimes. Self-field behavior can be divided into two regimes: collisional and collective. A beam is in the collisional regime when interactions between neighboring single particles dominate. This region requires the Debye length (Equation 2.58) to be on the order of the interparticle distance l_p, which occurs at very low temperature or very high density (both of which reduce the Debye length) [56]. The beam temperature refers to the random transverse motion within the beam, characterized by $\tilde{v}_x$. In this regime, the space charge forces are non-uniform over the beam and effects such as intrabeam scattering become significant.

If instead $\lambda_D \gg l_p$, Debye shielding limits the impact of nearest neighbors and collective behavior arises. In Debye shielding, effects of a charge on a neutral plasma are screened over a distance λ_D. Charged particle beams are non-neutral plasmas, but Debye shielding still takes place due to the restoring force of magnetic focusing. The resulting space charge forces can be described by a smooth distribution over the beam.

The Debye length also characterizes whether self-fields are significant with respect to externally applied fields. When the λ_D is large compared to the size of the beam, the effects of space charge are limited. This occurs when beams have sufficiently high energy, as λ_D scales with γ. When the opposite is true, space charge fields can dominate. This is a significant concern in electron sources, since the beam is inherently non-relativistic as it is created. The desire to reach high γ quickly to prevent degradation from space charge is a strong motivator for high gradient accelerator R&D, as discussed in Section 1.3.2.

2.5 High gradient structure testing

The experimental operation of high frequency cavities with very high surface fields and accelerating gradients is largely uncharted territory. Theoretical predictions indicate an increase in the breakdown voltage scaling with frequency, as discussed in Section 1.3.3. However, experiments are needed to verify these scalings.

One such experiment was performed using normal conducting W-band (75–110 GHz) copper cavities [59, 46]. These measurements provide a basis for the work presented in this thesis. The test structures consisted of three coupled cells with the π mode at 110 GHz. The structures were designed to have the majority of the field concentrated to the center cell to approximate a single cell structure [60]. This field balance and the overall design of the structures are intended to directly scale from structures used for breakdown tests at lower frequencies, such as [17, 61].

The measurements consisted of 'processing' the structure and monitoring the breakdown rate. In accelerator cavity processing, power is first supplied at an low value for many pulses. Initially, there is a high breakdown rate due to small imperfections. The power is increased once the breakdown rate stabilizes below an acceptable threshold. Measurements were performed with up to 575 kW of RF power dissipated into the copper structure. Power was supplied in 10 ns pulses. The structure was processed to this power with more than 10^5 pulses and achieved gradients up to 230 MeV/m with statistical breakdown rates of roughly 10^{-3} per pulse. The achieved gradient indicates the peak surface electric fields likely exceeded 500 MV/m. The peak pulsed heating was calculated to be less than 40 °C, which is below the threshold of expected damage based on previous experiments [18].

The primary limitation in these results was the available source power and repetition rate. The measurements indicate that the structure was still processing at the conclusion of the run and the breakdown rate is expected to decrease further with additional shots. Experiments at lower frequencies have reached 100 MeV/m gradients with sufficient breakdown rates below 10^{-6} per pulse after 10^8 shots [62]. The measurements performed at 110 GHz reached this threshold after only 10^4 shots. The fast processing of the structure to gradients above 100 MeV/m matches with the expected improvements at high frequency. These measurements demonstrate the feasibility of sustaining very high surface fields and gradients in room temperature copper structures when operating at high frequency.

The high power experimental setup designed for this thesis (presented in Chapter 5) is based on this experiment. High power was provided by a 110 GHz gyrotron. Gyrotrons are RF sources similar to klystrons that use an electron beam to produce electromagnetic waves. Unlike klystrons, they can produce high power at hundreds of GHz because they are fast wave devices. The generation of the electromagnetic waves is the result of stimulated emission from electrons moving in cyclotron orbits in a strong magnetic field. More details of the 110 GHz gyrotron are discussed in Section 5.2.

Measurements of the forward power from the gyrotron in this experiment can be used to calculate the expected surface fields in the gun cells. Figure 2.5 shows an example input power pulse and the resulting surface electric field on the cathode tip. For this particular input pulse, the cavity is not fully filled and the peak surface field is 3.4 GV/m. A slightly longer pulse at 500 kW will allow the gun to reach the design value of 3.9 GV/m on the tip.

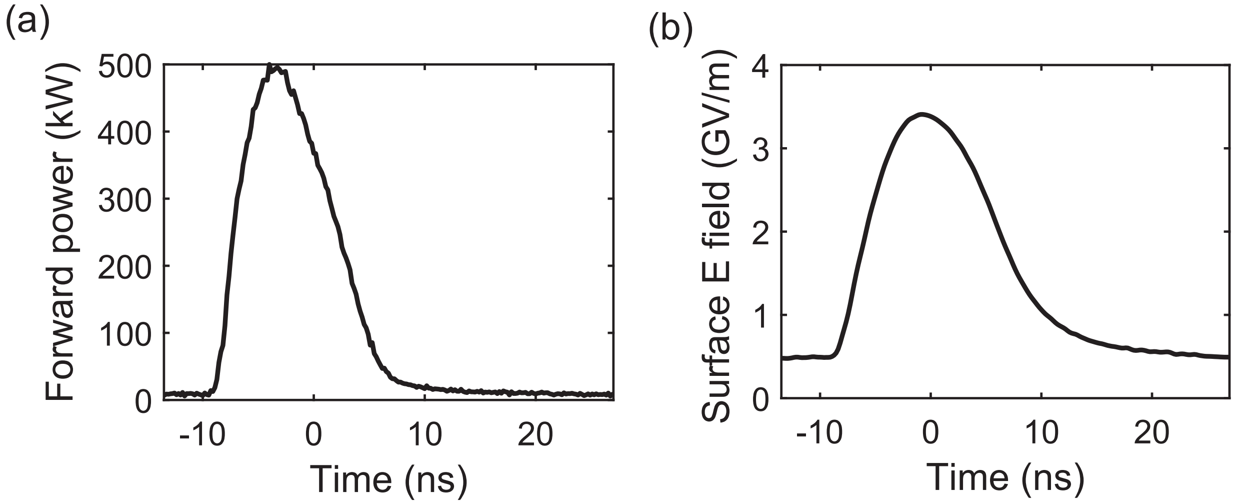

Figure 2.5: (a) Measured forward power of a gyrotron pulse. The forward power is measured after the pulse is shortened by a switch (see Section 5.2). (b) The calculated time-domain surface field on the cathode. The calculations are based on modeled fields in the gun, discussed in Section 3.3. The baseline is above zero because there is leakage in the switch which shortens the gyrotron pulse, so some input power is delivered to the structure before the main pulse.

Chapter 3

Gun design and modeling

3.1 Introduction

As outlined in the previous chapters, there is significant demand for novel electron sources for future accelerators. THz-based accelerators are a promising pathway to achieve high-brightness beams with a compact footprint. To build such an accelerator, there is a clear need for a THz electron gun. This thesis aims to explore the fundamental questions about the design, performance, and fabrication techniques which can render such a gun viable.

The chosen target for a first demonstration was a gun structure capable of producing MeV electrons and reaching GV/m-scale gradients. This energy scale is desirable for use in UED. Based on this target application, a bunch charge on the order of 10-100 fC was chosen. The initial design constraints were not focused on emittance beyond achieving parity with existing photocathodes. The gun was designed to be powered by a 110 GHz gyrotron which is capable of providing up to 1 MW of power. To match this source, the guns were designed to operate in the π mode near 110.08 GHz.

Field emission is a natural choice that would utilize the increased fields already required for high-gradient acceleration. Gun structures were designed for two cathode types: a diamond nano-tip and a larger copper tip. Each design has relative advantages in achievable current, emittance, and ease of use and fabrication. This chapter details the electromagnetic design of each structure including multiple variations which were considered. Particle simulations for both final designs are included, with a primary focus on the copper tip design which was chosen for high power testing.

3.2 Diamond tip gun

3.2.1 Diamond field-emitter arrays (DFEAs)

Field emission cathodes typically use a tip in order to have local electric field enhancement over a small region. The size of the emitting area directly contributes to the emittance. As a result, nanometer-scale tips are of interest in field emission gun design. Nano-tips can also be used in an array to produce patterned beams. Extensive work is underway to develop field emitter arrays based on micrometer-scale diamond pyramids with nano-scale tips [63, 64, 65, 66]. Originally developed by scientists at Vanderbilt University [67, 68], these diamond field-emitter arrays (DFEAs) consist of multiple diamond pyramids and a base layer of diamond bonded to a metallic substrate. After conditioning, single tips can achieve currents as high as 15 μA and emission can occur with fields as low as 10 MV/m.

Modeling of electron emission and corresponding experiments indicate that only a small area on the tip emits [65, 66] leading to a beam with a very small transverse size. The emission and beam performance has been studied under DC fields and 1.3 GHz RF fields [69, 66, 70, 71]. These experiments have measured normalized transverse emittances as low as 0.689 μm-rad. The enhanced surface fields were estimated to be 2 GV/m at the point of the nano-tip.

Due to their small size, DFEAs were chosen as a candidate cathode for this electron gun design. Use in 110 GHz cavities would be a new regime of study for DFEAs. In this structure, the fields would also be much higher than previous experiments. Electromagnetic simulations detailed in the following sections predict the electric field to be hundreds of MV/m across the entire pyramid and diamond base layer. The field values would be even higher locally on the nano-tip after enhancement. Sample cathodes were produced by Simakov *et al.* at LANL consisting of sparse 3×3 grids of pyramids. Three sizes were produced, with pyramid bases of 8 μm $\times$ 8 μm, 18 μm $\times$ 18 μm and 28 μm $\times$ 28 μm. In each case, the spacing between pyramids is 1 mm, allowing for use of a single tip on-axis. A collection of images of these arrays are shown in Figure 3.1.

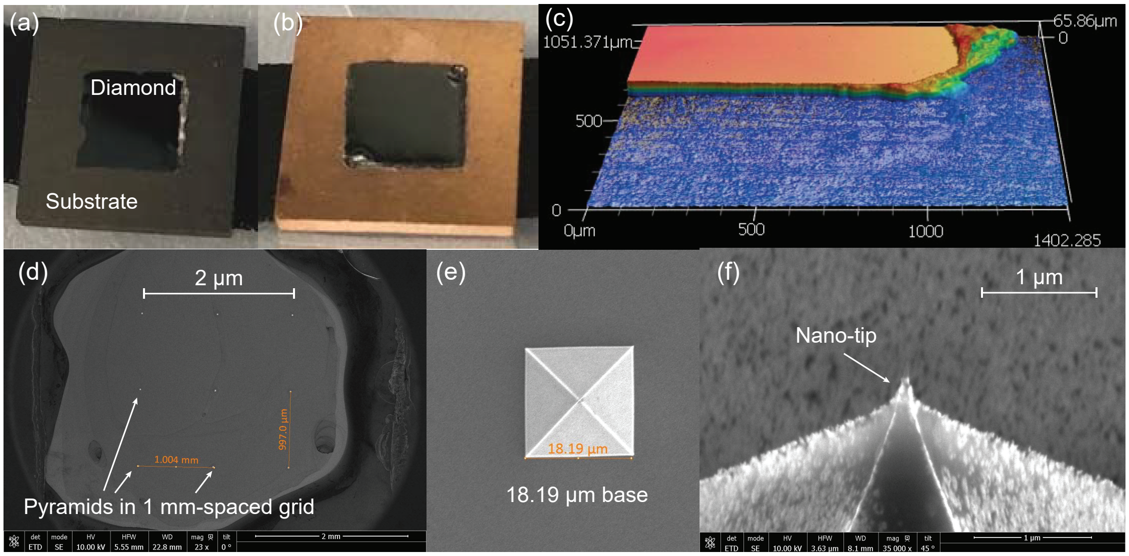

Figure 3.1: (a) Fabricated DFEA consisting of a diamond square with diamond pyramids bonded to a molybdenum substrate. (b) DFEA bonded to copper substrate. (c) Height profile of the diamond layer and braze alloy on a molybdenum substrate, measured using a laser confocal microscope. (d-f) SEM images of the DFEA. (d) The overall array and spacing of the pyramids, (e) a top-down view of a pyramid with an 18 μm base, and (f) an image of the nano-tip at the top of the pyramid taken at a 45 degree angle. SEM images by Dongsung Kim at LANL.

3.2.2 Performance limitations

Electron guns based on DFEAs have the potential to produce low emittance beams due to the small size of the emitter. The low turn-on field means they can produce high currents in many environments. Their small size also makes them attractive for use in THz-frequency structures, where the cell irises and possible beam tunnel sizes are on the order of hundreds of microns. With high current, low emittance bunches accelerated at high gradient, it would be possible to achieve very high brightness beams.

However, limitations arise when attempting to shield the tips from potentially damaging GV/m-scale electric fields. These fields are part of what makes high-gradient acceleration possible at THz frequencies, but DFEAs are untested in this range. More work is needed to determine whether DFEAs can withstand RF fields on the order of GV/m over the entire pyramid. It is likely that emission would occur over a larger area of the pyramid and the diamond base layer, since the field strength is well above the threshold required. This would result in larger emittance and limit the beam quality. The initial designs presented in the following sections limit the fields to order 100 MV/m using a recess to protect the tips.

By placing the tip in a lower field region of the cell, it limits the accessible range of RF phases where electrons achieve significant acceleration. This has the benefit of limiting the length of the bunch, but makes it challenging to operate the structure at low input power. There was an observed tradeoff in shortening the length of the first cell or half cell with the achievable coupling into that cell. When the half cell was too short compared to the other cells, the modes were effectively localized entirely to the full cells. This could potentially be solved by coupling directly into the first cell using rectangular waveguides. The two-cell structure described Section 3.2.4 is a candidate for high power measurements but requires at least 500 kW for any acceleration.

3.2.3 2.5 cell geometry

The most common electron gun design uses a half cell to house the cathode. This places the cathode at a maximum field position which is typically desirable for achieving the correct emission timing. In order to achieve GeV/m-scale gradients, the fields in the cavity must reach GV/m-scale. Thus, a cathode placed in the maximum field region of the cavity would experience potentially damaging multi-GV/m fields. Rather than a true 2.5 cell design, this gun includes a recess to partially shield the tip from the highest fields. This also serves to limit the bunch charge, since unnecessarily high charge will degrade the beam quality from space charge effects. The half cell is slightly shortened compared to the two full cells to account for the low initial energy of the beam.

The 2.5 cell structure was tuned to support the π mode at 110.077 GHz. A model of the structure is shown in Figure 3.2 and the design values are summarized in Table 3.1. Power is coupled into the structure on-axis in a circular waveguide mode. The coupling structure used for all the gun designs is discussed in detail in Section 3.4.

The electromagnetic performance of the gun was modeled using Ansys's High Frequency Structure Simulator (HFSS) [72]. HFSS is a full 3D finite element electromagnetic solver. Initial eigenmode calculations were performed to find the resonances and tune the structure. Driven modal calculations were performed using the on-axis circular waveguide port. To reduce computational complexity, tuning simulations utilized symmetry conditions on a 5 degree wedge of the structure. Figure 3.3 shows the magnitude of the complex electric field on the π mode resonance in the driven simulation.

Using the HFSS results, calculations were performed to model the acceleration a single particle emitted on-axis would experience for all phases of the electric field. The maximum acceleration results for different input powers are shown in Figure 3.4. The electric field experienced by the particle is also shown. For low input power, it is clear that there is some deceleration. The available input power of the gyrotron source planned for high power measurements is currently limited to 1 MW. That input power is not sufficient to accelerate particles in this structure, so it was not chosen to be fabricated. However, this design could prove useful when more input power is available.

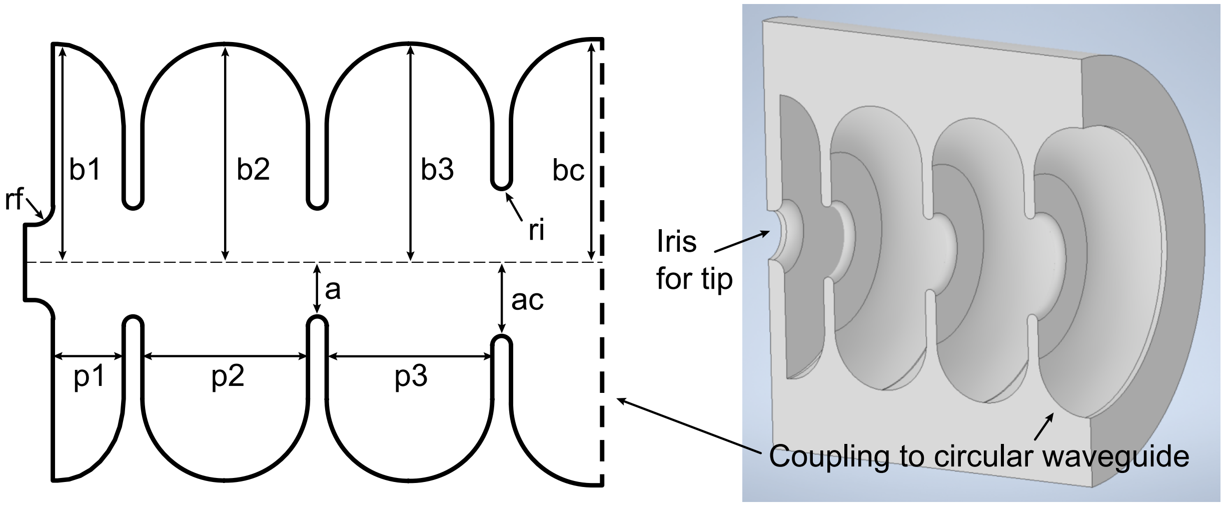

Figure 3.2: Schematic and model of the 2.5 cell structure. The structure is cylindrically symmetric around the horizontal dashed line shown. The parameters of the design are summarized in Table 3.1. The half cell contains an iris to shield the diamond tip from the highest fields. The schematic shows the vacuum space used for electromagnetic simulations. The 3D model shows a cut plane of the structure with the tip location and coupling cell indicated.

Parameter	Value (mm)	Description
a	0.286	Iris radius
ac	0.390	Coupling iris radius
b1	1.160	Radius of first (half) cell
b2	1.160	Radius of second cell
b3	1.162	Radius of third cell
bc	1.185	Radius of input circular waveguide
p1	0.375	Length of half cell
p2	0.88	Length of second cell
p3	0.88	Length of third cell
rf	0.1	Tip iris radius of curvature
ri	0.05	Iris radius of curvature

Table 3.1: Design values of the 2.5 cell diamond tip gun.

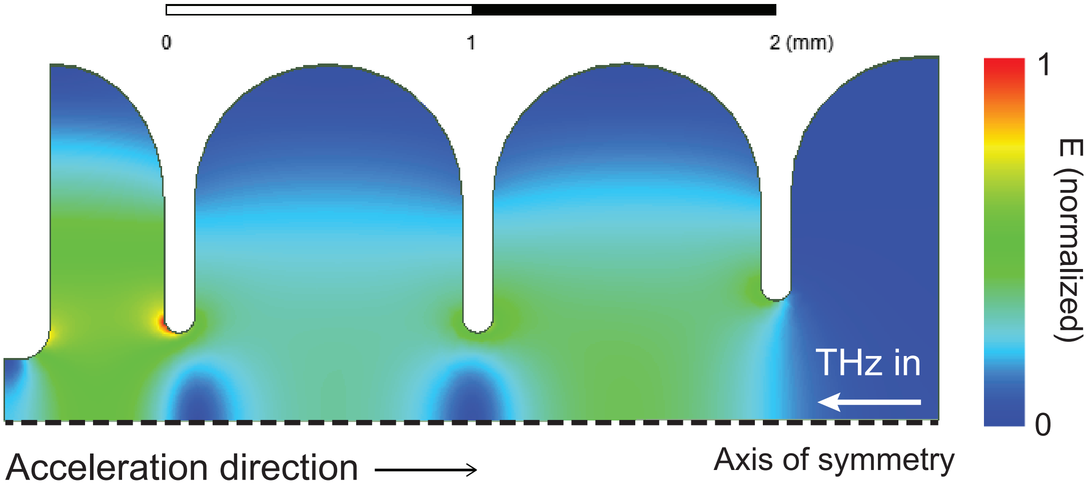

Figure 3.3: Electric field of the π mode in the 2.5 cell structure. The simulation assumes cylindrical symmetry around the dashed line. The electric field is shown in normalized units.

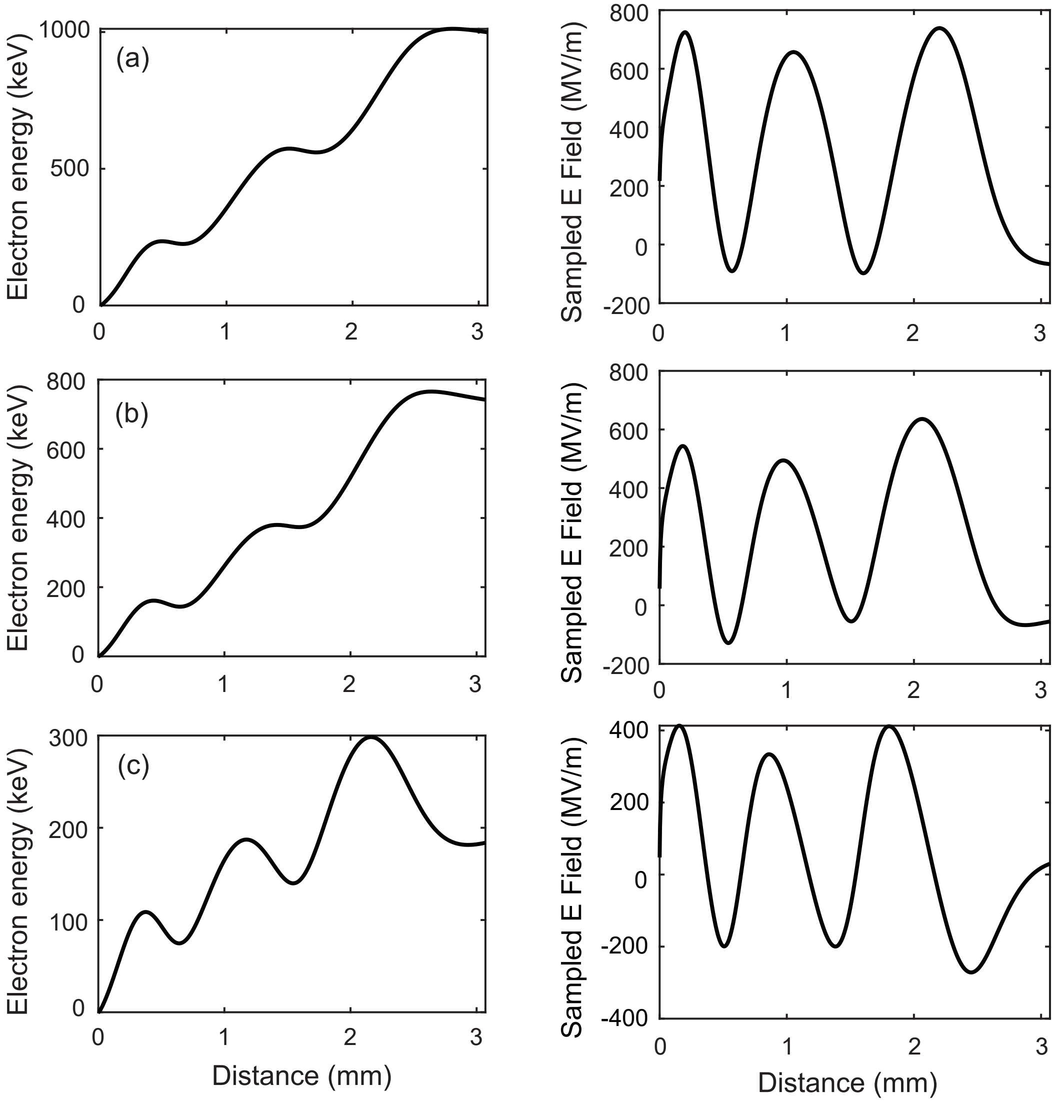

Figure 3.4: Single particle acceleration for various input powers. Each row shows the energy of the electron and the electric field it experiences as it travels down the structure. Row (a) shows results for 3.2 MW of input power. For this input power, it is possible to generate 1 MeV electrons, the initial design target. Row (b) shows results for 2 MW, and (c) shows results for 1.4 MW, the lowest input power that results in particles that gain enough energy to leave the structure. Deceleration is visible in all cases, but is most extreme in the low power case of (c). Deceleration occurs when the particle experiences the incorrect orientation of the electric field. In this plot, a positive field value corresponds to the field pointing towards the tip, which is the direction required for acceleration of electrons.

3.2.4 2 cell geometry

The primary drawback of the 2.5 cell design, aside from the high power needed to achieve reasonable acceleration, was the small size and sharp corner required in the half cell. Since the design aims to shield the diamond tip using an iris, a second design using 2 full cells was developed. Instead of a recess in a half cell, the tip sits in an iris at the start of the first cell. In this version, the irises were thickened to make them easier to fabricate and the cells were shortened. A schematic and model are shown in Figure 3.5 and the design values are summarized in Table 3.2.

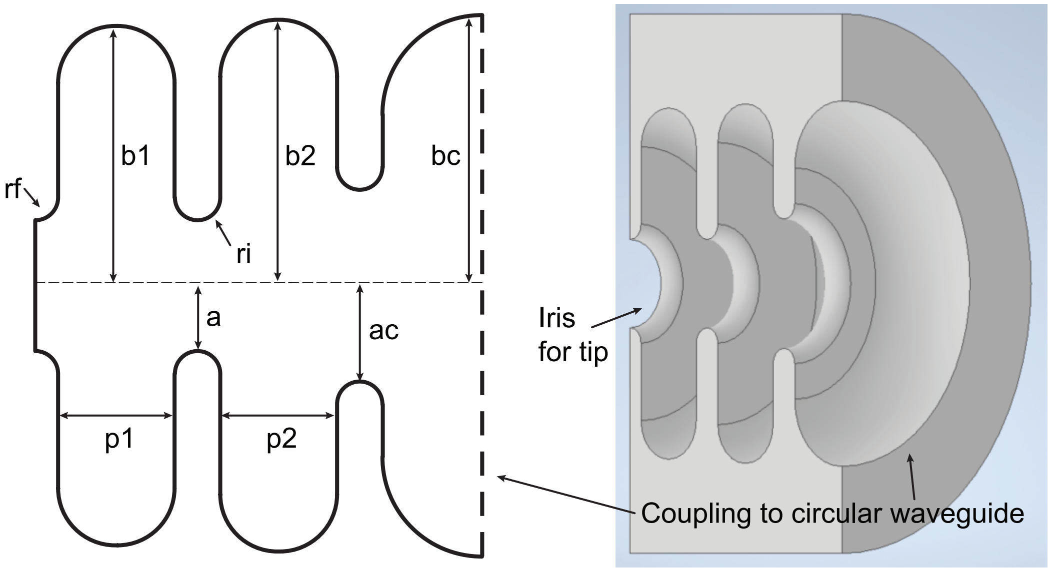

Figure 3.5: Schematic and model of the 2 cell structure. The structure is cylindrically symmetric around the horizontal dashed line shown. The parameters of the design are summarized in Table 3.2. The irises are thicker than in the 2.5 cell design and the cells are shortened. The 2 cell version utilizes an iris to shield the diamond tip.

The two cell design was tuned to ~ 110 GHz for the π mode. Eigenmode and driven modal simulations were performed in HFSS to calculate the fields. The first cell is significantly smaller in radius than the second. This makes the field stronger in the first cell and near the tip, which is the balance required for good acceleration. The calculated electric field magnitude is shown in Figure 3.6. The results of single particle calculations based on this field are shown in Figure 3.7.

The 2 cell structure performs better at low input power, making it a candidate for testing with the available source. This improvement comes primarily from the shortened cells and reduced length of the structure. The gun achieves reasonably good acceleration for 1 MW of input power, but it is possible to achieve acceleration over a limited range of launch phases

Parameter	Value (mm)	Description
a	0.286	Iris radius
ac	0.419	Coupling iris radius
b1	1.138	Radius of first cell
b2	1.165	Radius of second cell
bc	1.185	Radius of input circular waveguide
p1	0.51	Length of first cell
p2	0.51	Length of second cell
rf	0.1	Tip iris radius of curvature
ri	0.1	Iris radius of curvature

Table 3.2: Design values of the 2 cell diamond tip gun.

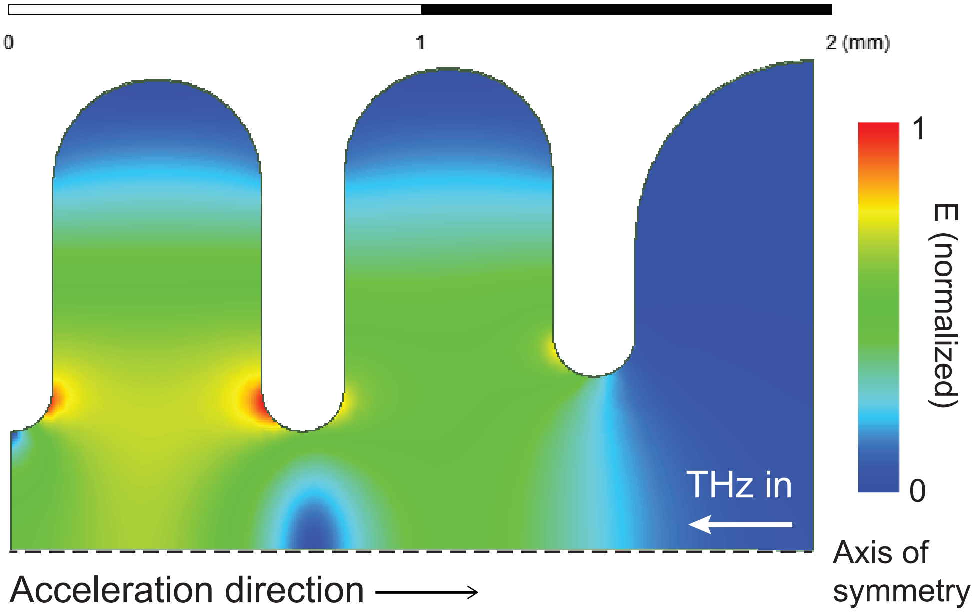

Figure 3.6: Electric field of the π mode in the 2 cell structure. The simulation assumes cylindrical symmetry around the dashed line. The electric field is shown in normalized units.

with 500 kW of input power. For 2 MW of input power, the 2 cell structure produces 650 keV electrons after 2 mm of acceleration. By contrast, the 2.5 cell structure produces slightly higher energy electrons (750 keV) over 3.1 mm. This design was chosen to be fabricated to test with the available DFEA samples. However, limitations in the currently available gyrotron power make it less attractive for a first round of high power testing than the copper cathode design discussed in the next section.

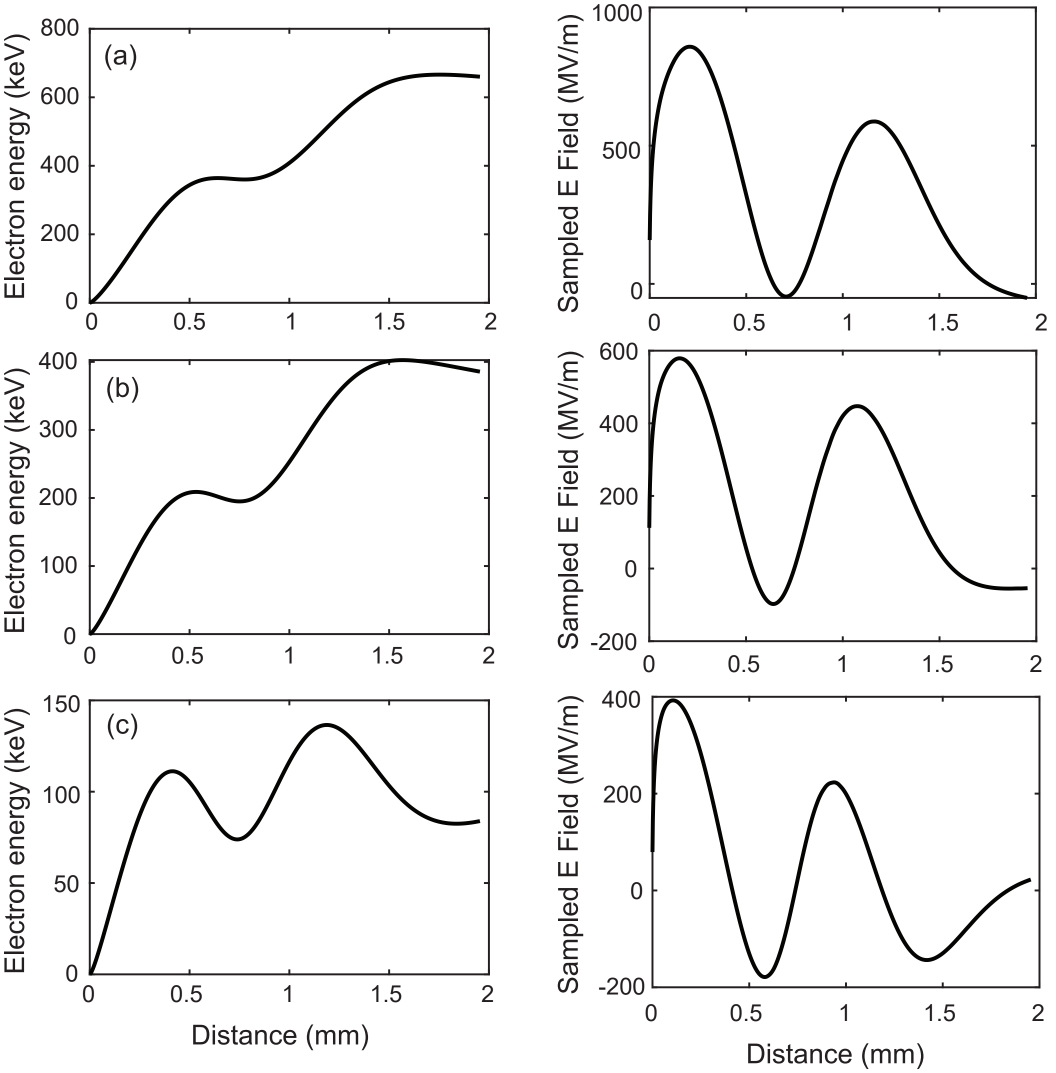

Figure 3.7: Single particle acceleration for various input powers. Each row shows the energy of the electron and the electric field it experiences as it travels down the structure. Row (a) shows results for 2 MW of input power and row (b) shows results for 1 MW. Row (c) shows results for 500 kW, the lowest input power that results in particles that gain enough energy to leave the structure.

3.3 Copper tip gun

Copper was identified as another possible field emission source. Normal conducting RF devices are typically made from copper due to its high conductivity, which limits losses. High gradient measurements of copper THz cavities have shown that it can tolerate surface fields on the order of a GV/m [46]. This makes it possible to insert a copper cathode into a high field region for better acceleration. After field enhancement, the fields on the tip are multiple GV/m, which is sufficient for field emission but low enough to be sustainable. By using a larger, rounded tip rather than a sharp nano-tip, field enhancement and the resulting bunch charge can be limited to reasonable values.

The copper tip design uses a rounded tip inserted halfway into the first cell. This maximizes the surface field on the tip for emission and good acceleration. The geometry of the cells was chosen to be similar to the diamond tip two cell design since the feature sizes were already determined with fabrication constraints in mind. A schematic of the design is shown in Figure 3.8 and the parameter values are summarized in Table 3.3.

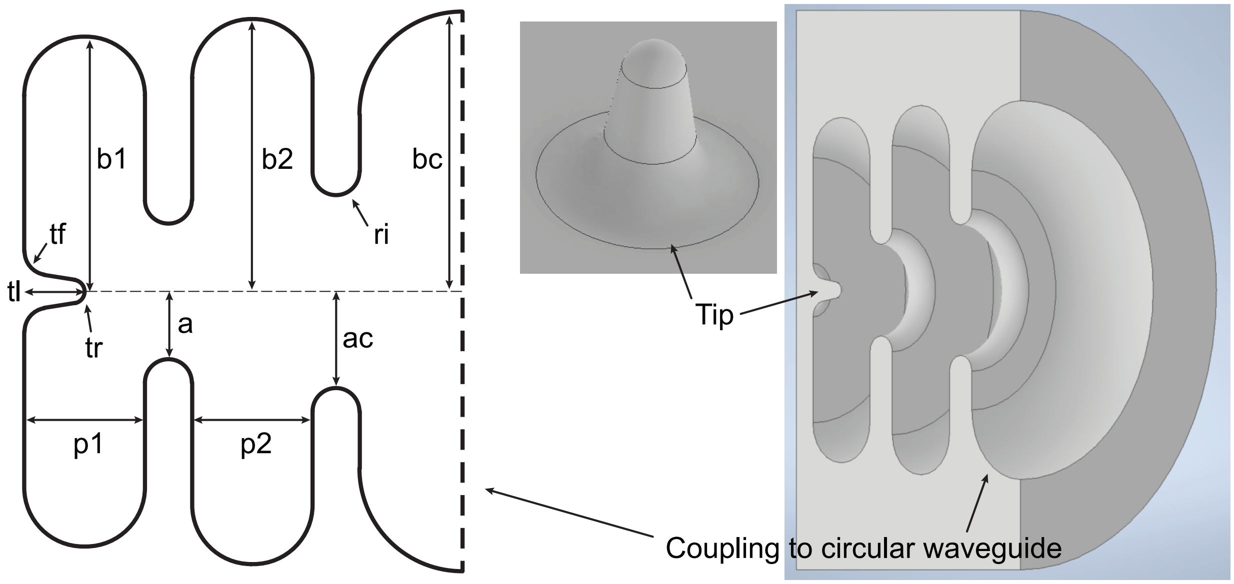

Figure 3.8: Schematic and model of the copper tip gun. The structure is cylindrically symmetric around the horizontal dashed line shown. The parameters of the design are summarized in Table 3.3. The overall design is similar to the 2 cell diamond tip structure, but instead uses a μm-scale copper tip inserted halfway into the cell.

The copper tip is much larger than the DFEAs discussed in the previous section. This will inherently result in a larger emittance, but is required for fabrication feasibility. The structure was designed to be electroformed as one monolithic piece, meaning there are no joints inside the geometry shown in Figure 3.8. Other designs were considered that would allow

Parameter	Value (mm)	Description
a	0.286	Iris radius
ac	0.408	Coupling iris radius
b1	1.080	Radius of first cell
b2	1.155	Radius of second cell
bc	1.185	Radius of input circular waveguide
p1	0.51	Length of first cell
p2	0.51	Length of second cell
ri	0.1	Iris radius of curvature
tf	0.1	Tip base radius of curvature
tl	0.255	Tip length
tr	0.050	Tip radius of curvature

Table 3.3: Design values of the copper tip gun.

the tip to be inserted through an aperture, similar to the diamond tip 2 cell design. These designs all achieve similar performance based on electromagnetic simulations. Ultimately the monolithic design was chosen because it was the best fit for electroforming.

Electromagnetic simulations were performed to identify and tune the resonances. The π mode was designed to be 110.01 GHz. Figure 3.9 shows the calculated electric field magnitude when the cells are driven by the on-axis circular waveguide port. The field is strongly enhanced at and around the tip. Figure 3.10 shows the field values the particle experiences for various input powers. For 1 MW of input power, the maximum field on the tip is as high as 5.75 GV/m.

Based on this strong field enhancement, it is possible to operate the copper tip gun at much lower input powers than either of the diamond tip designs. For just 1 MW of input power, electrons can be accelerated to energies up to 500 keV in 1.6 mm. Electrons in the 2 cell diamond tip structure only reach about 380 keV for the same input power; the 2.5 cell diamond tip structure cannot be operated with 1 MW.

An input power of 500 kW was chosen as the nominal operating point. This is roughly the maximum power used in breakdown studies of THz W-band cavities thus far [46] and is readily available from the gyrotron source. However, the structure still performs very well with as low as 50 kW of input power. Figure 3.10c shows that there is very little deceleration even for such low input power and the surface field on the tip reaches 800 MV/m.

The excellent acceleration performance at a variety of input powers made the copper structure the ideal candidate for the first round of high power measurements. This additional degree of freedom makes it possible to study the emission and beam properties over a

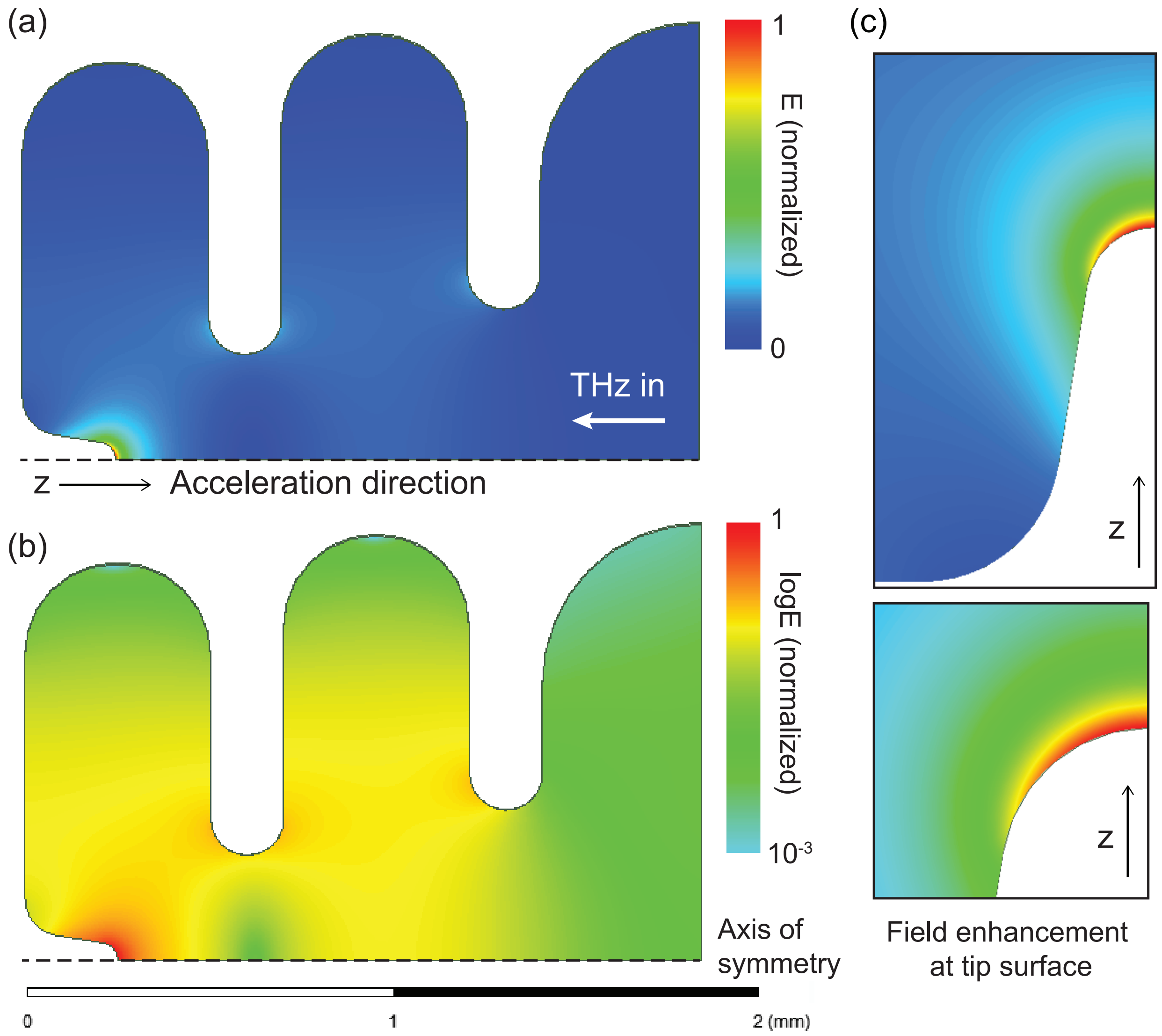

Figure 3.9: Electric field of the π mode in the copper tip structure. The simulation assumes cylindrical symmetry around the dashed line. The electric field is shown in normalized units. (a) The magnitude of the complex electric field on a linear scale and (b) on a log scale. The field is strongly enhanced around the tip, which is desirable for field emission. The maximum field magnitude on the tip is roughly 4.5 times the maximum surface field on the iris. (c) Zoomed view of the enhanced field on the tip. The strong field on the surface itself is responsible for field emission, and the enhanced field on-axis ensures rapid acceleration.

range of operating points for comparison with simulations. The beam characterization setup described in Chapter 5 was designed to take advantage of this possible range of operating

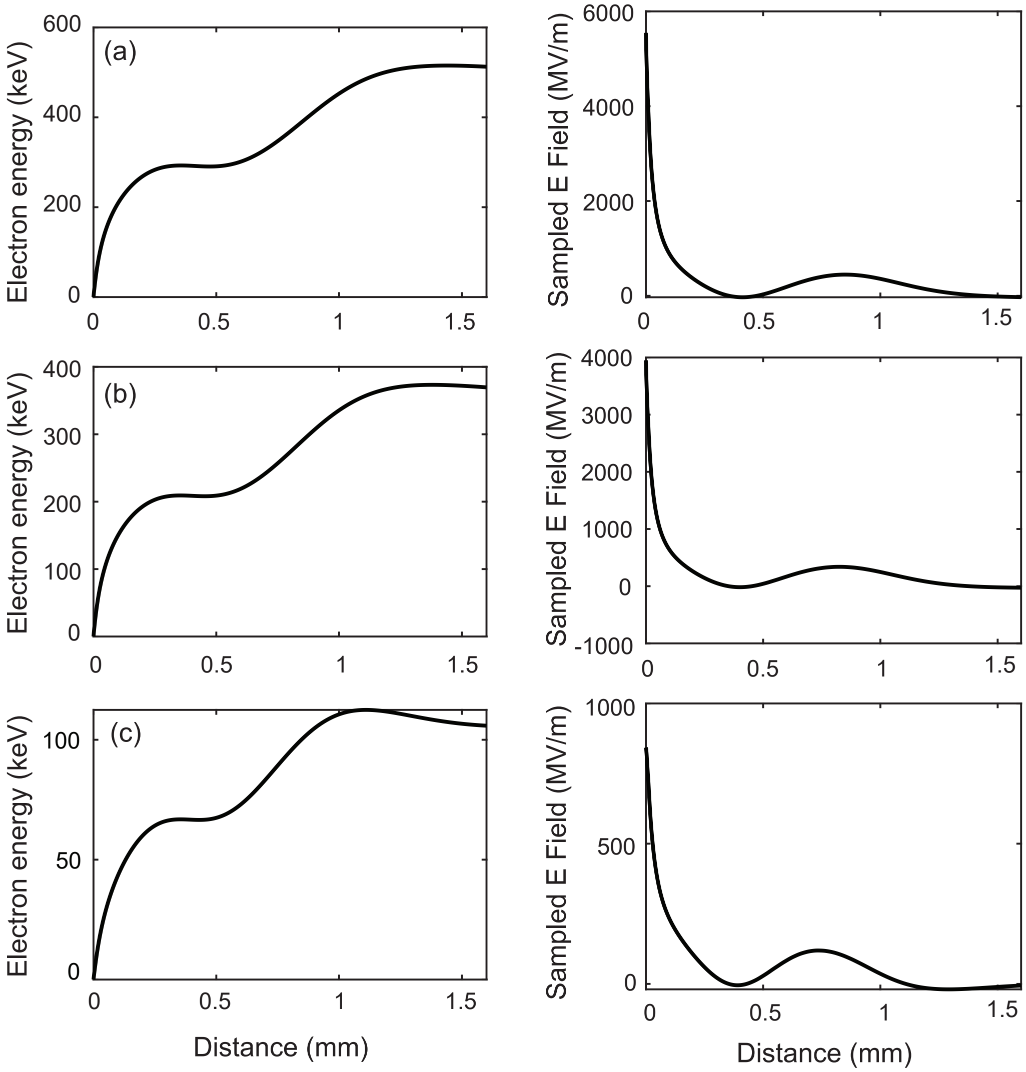

Figure 3.10: Single particle acceleration for various input powers. Each row shows the energy of the electron and the electric field it experiences as it travels down the structure. Row (a) shows results for 1 MW of input power. Row (b) shows results for 500 kW, a source power reliably available from the gyrotron. Row (c) shows results for 50 kW, the lowest input power that results in particles that gain enough energy to leave the structure.

points. The strong fields on the tip will also provide a useful new data point to study the breakdown scaling discussed in Section 1.3.2.

3.4 Input coupling and beam tunnel

All of the designs presented are powered by an on-axis circular waveguide with a radius of 1.185 mm. Simulations are based on input power in the form of the TM_{01} circular waveguide mode. This cannot be provided directly by the gyrotron, which operates in the $TE_{22,6,1}$ mode [73, 74] and is transported in the HE_{11} mode of a corrugated waveguide [75]. The HE_{11} mode is Gaussian-like and thus couples to a Gaussian free-space mode outside of the waveguide. Further details of the gyrotron transmission are discussed in Section 5.2.

To couple the gyrotron output into the structure, a Gaussian horn and mode converter was designed. The input THz beam is focused onto a Gaussian horn which converts to the TE_{11} circular waveguide mode. A mode converter with a 90 degree bend converts from the TE_{11} to the TM_{01} mode. This mode converter has been demonstrated to couple well to similar W-band cavities and has a 97% conversion efficiency [59].

The geometry of the horn and mode converter is shown in Figure 3.11. There is a beam tunnel through the wall of the mode converter which does not impact the performance. There is also a rectangular waveguide WR-8 (90–140 GHz) port off of the beam tunnel. This is a weakly coupled port which will serve as a diagnostic measuring the transmitted power.

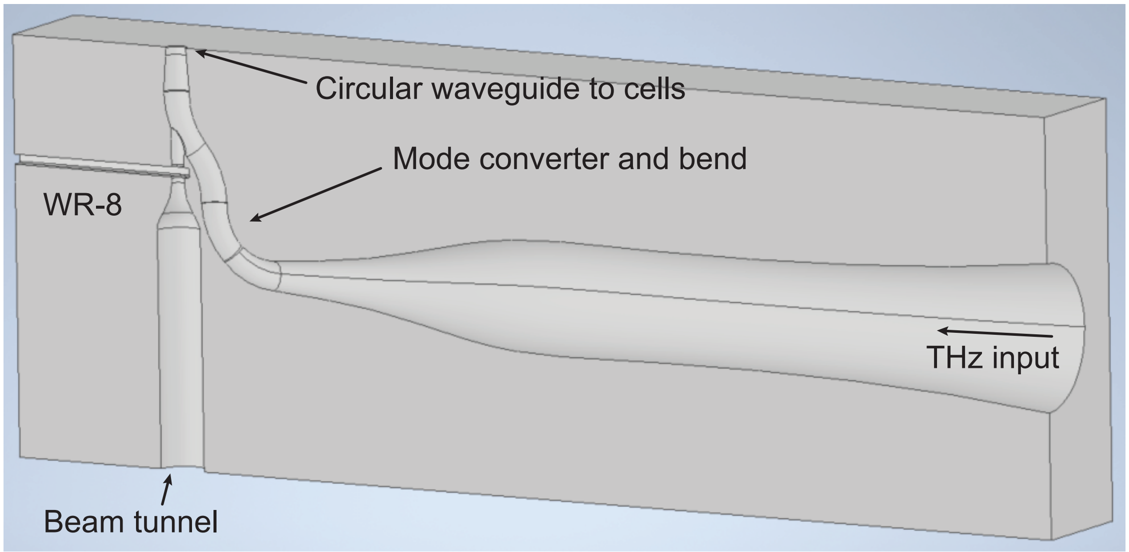

Figure 3.11: Model of one half of the Gaussian horn and mode converter. The other half is a mirror image. The beam tunnel, WR-8 diagnostic port, and the circular waveguide that couples to the cells are indicated.

Simulations were performed focusing on the mode converter, beam tunnel, and gun structure region. The performance of the Gaussian horn is well established by previous work [59, 60] and was not included to reduce the simulation time. Figure 3.12 shows the fields in the structure on the π mode resonance, and Figure 3.13 shows the S parameters for the two port network. The fields are strongly localized to the cells.

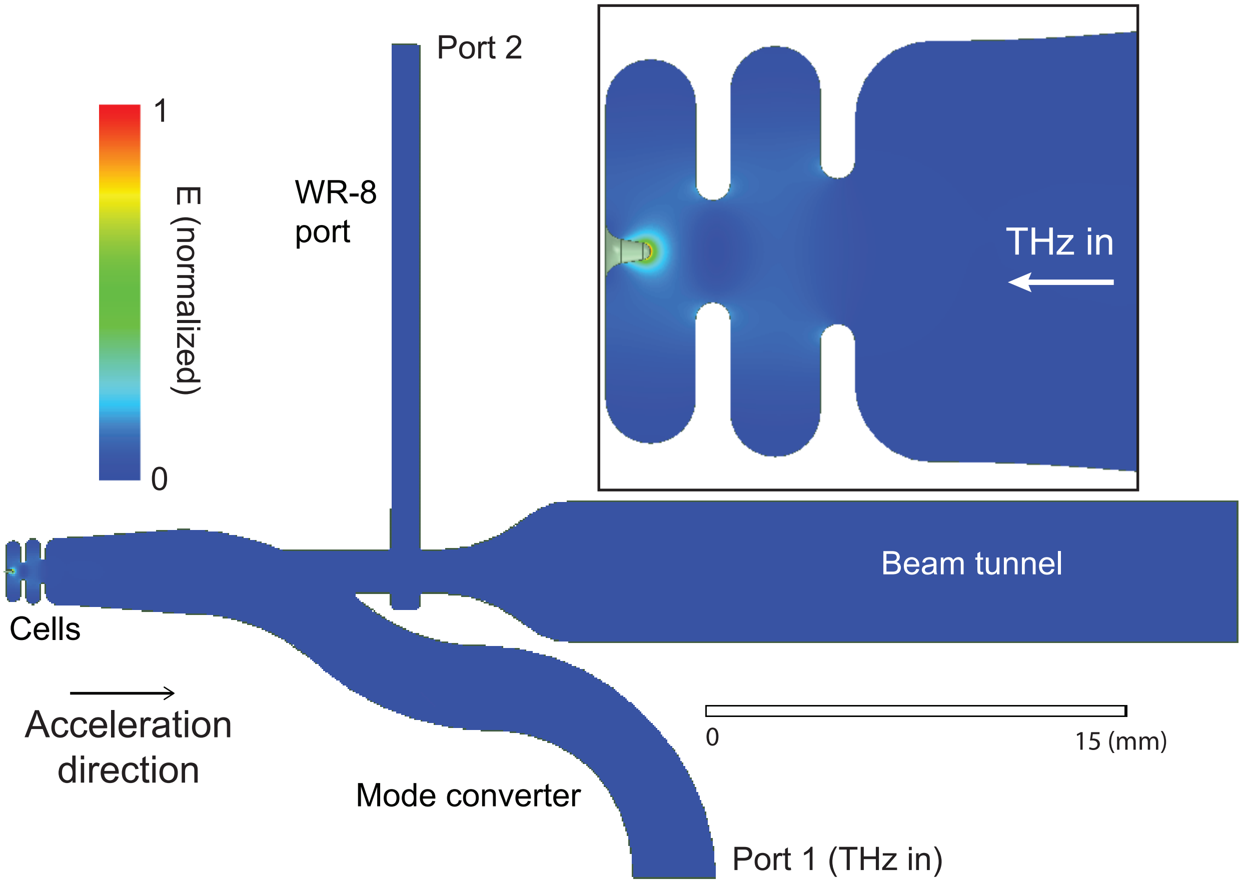

Figure 3.12: Electric field of the mode converter and copper tip structure on the π mode resonance. The simulation assumes mirror symmetry across the plane shown. The electric field is shown in normalized units. Power is input from port 1 and coupled into the cells. The inset shows that the field profile in the cells matches the cell-only simulation, Figure 3.9.

The horn and mode converter block is designed to be fabricated in two halves and brazed together. The cell structures are not bonded to the block and are fully demountable. The standardized block allows for multiple gun structures to be tested interchangeably with the same setup. Full details of the cell mounting can be found in Section 5.3.

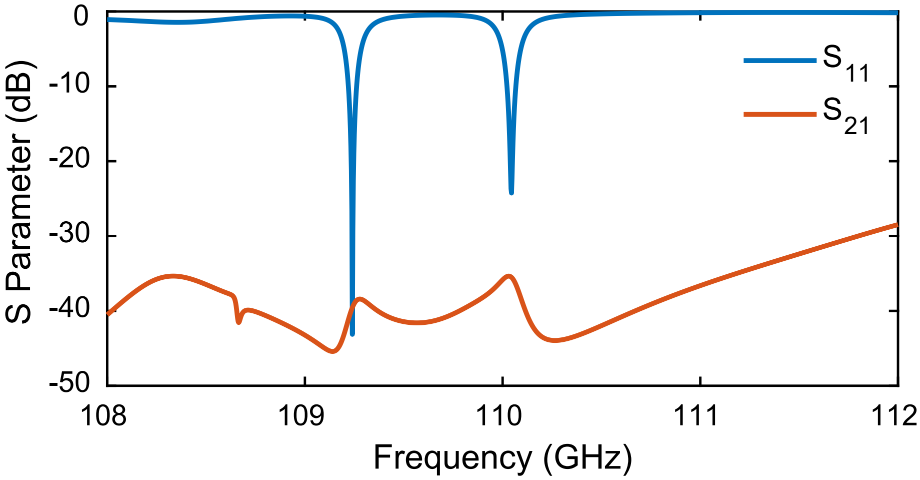

Figure 3.13: S parameters driven from the mode converter (port 1). S_{21} shows the coupling from the horn to the diagnostic port (port 2). The o mode and π mode resonances are visible.

3.5 Particle simulations

Modeling of the electron beam was performed using General Particle Tracer (GPT) [76]. Simulations were performed in 3D using the cavity fields exported from HFSS. Both the 2 cell diamond tip and copper tip structures were modeled. The GPT simulations include the beam dynamics in HFSS fields of the cells and transmission through the beamline to the electron detectors. This section will focus on the beam modeling in the gun cells. The simulations of the magnets and detectors are detailed in Chapter 5.

GPT does not contain any built-in field emission models. Instead, two models were written based on the Fowler-Nordheim equation (Equation 2.46) and the available literature on field emission in the two materials. The results were input as the starting beam parameters in GPT. To limit computational complexity, the majority of simulations were restricted to one RF cycle of emission.

3.5.1 Diamond tip

As DFEAs are fairly new, their emission characteristics have not been fully studied. There can be variation in the turn-on field and performance depending on the crystal structure and material preparation. The effective emission area and field enhancement also varies. A simple model was developed to estimate the emission in a THz field.

While in lower field cases emission should largely come from the nano-tip as described in Section 3.2.1, the high surface fields in the THz gun make it likely that some or all of the diamond base layer will also emit. Figure 3.6 shows that the surface field is nearly constant across the iris aperture. The diamond base layer has surface roughness that will cause further field enhancement. As a result, the the total area πa^2 of the iris was used as the emission area. A total emission current was calculated using this area and a uniform surface field.

The calculation of current versus field was based on the extensive modeling by Huang *et al.* [65]. The DFEAs modeled in this paper are the same type as those which will be used in the diamond tip gun. Their numerical modeling determined that the emitted current density from the bulk is fit by

$$J = 11.35 \times \exp\left(0.01141 \times E\,[\mathrm{MV/m}]\right) \tag{3.1}$$

where E in MV/m is the surface field. This modeling is consistent with Fowler-Nordheim behavior and matches with measured emission performance. Current density values were calculated based on this model and measured emission data at 11.4 MV/m. Typical emission values are roughly 14 μA/tip over an estimated area of 2–8 $\mu\mathrm{m}^2$ [64, 65]. These values match with Fowler-Nordheim predictions using $\phi = 1.5$ eV and significant field enhancement values of order 45–55, depending on the assumed emission area. This model takes into account more details about the material's emission properties, such as emission from the bulk. In contrast, the material properties in the Fowler-Nordheim equation are described solely by the work function ϕ.

Fields on the surface were exported from HFSS at 1 degree phase steps over one RF cycle. Using the full iris area and assuming no field enhancement, the net charge emitted was calculated to be 103 fC from Equation 3.1 for 1 MW of input power. Using the Fowler-Nordheim equation directly with no field enhancement, the charge predicted is $Q = 46.4$ fC. In reality, there will be some field enhancement due both to surface properties of the diamond and the shape of the pyramid. Plots of the emission versus RF phase are shown in Figure 3.14. The primary difference is that the pure exponential scaling of Equation 3.1 gives a larger range of phases for emission. Equation 3.1 and the results of [65] were chosen as the primary model for this work, since their modeling includes a more detailed representation of the DFEA emission.

To initialize the beam in GPT, the phase space distribution was assumed to be a uniform hemisphere over the iris radius a and 2π sr of initial angle. All particles were assumed to be born with 0.4 eV of kinetic energy, corresponding to $\gamma \approx 1$. Figure 3.15a and b show these distributions. The emission versus phase was applied in GPT as a time profile for initiating the beam. Figure 3.15c shows the build up of charge versus time.

The particles were accelerated using the full 3D, time-dependent fields exported from HFSS. Copper scattering boundaries were included to model the cell walls and apertures from the irises. Space charge effects were included using the built-in mesh-based routine. The resulting energy spread and transverse phase space distributions are shown in Figure 3.16. Significant energy spread arises from the particles emitted at non-optimal phasing. The maximum gamma is 1.725, which matches the prediction from the single particle model (Figure 3.7) at about 370 keV. However, most particles do not reach the maximum energy. Instead, the 'peak' with the maximum number of particles is slightly lower in energy. This

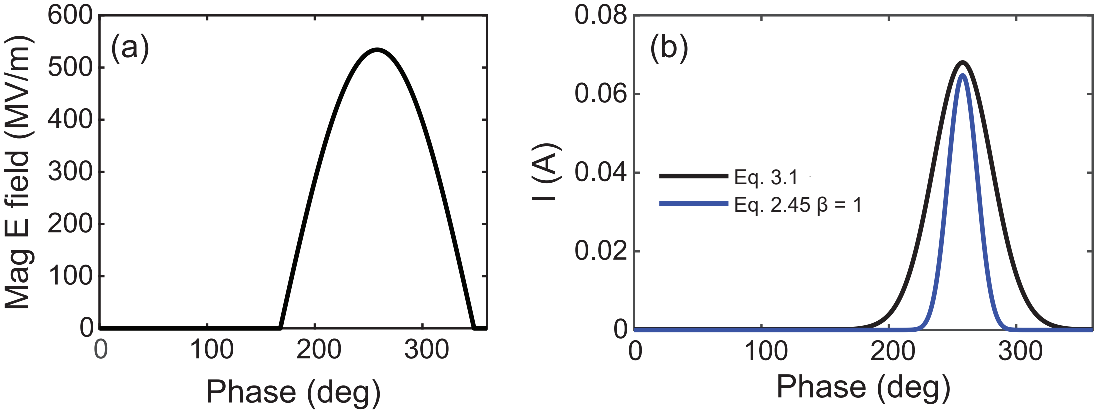

Figure 3.14: (a) Magnitude of the electric field on the diamond surface. Only half of the RF cycle is shown, corresponding to the correct direction for emission. (b) The current versus phase based on the field values shown in (a). Equation 3.1 predicts emission over a wider range of phases. The Fowler-Nordheim equation with $\phi = 1.5$ eV is also shown for $\beta = 1$, which represents an idealized case with no field enhancement. In reality, there would be field enhancement both from the surface properties and from the nano-tip.

peak corresponds to particles emitted when the field on the tip is close to maximum. In an ideal gun, this would correspond to the best phase for acceleration. In the diamond tip case, they are slightly offset, as discussed in Section 3.2.4. Instead, the peak energy is around 305 keV, with some electrons up to 370 keV and a long, almost uniform tail.

Many particles are lost when they are either accelerated back into the emitter or into a boundary. The large spatial extent of the beam is a direct result of assuming a large emission area. Depending on how the DFEA performs in these high fields, the beam size could be much smaller. Additionally, particles emitted at sub-optimal phases are still accelerated, resulting in significant beam spread in z. With multiple cycles of emission, these outliers effectively become part of the following bunch because their acceleration is largely due to spending more than 1 RF cycle in the structure.

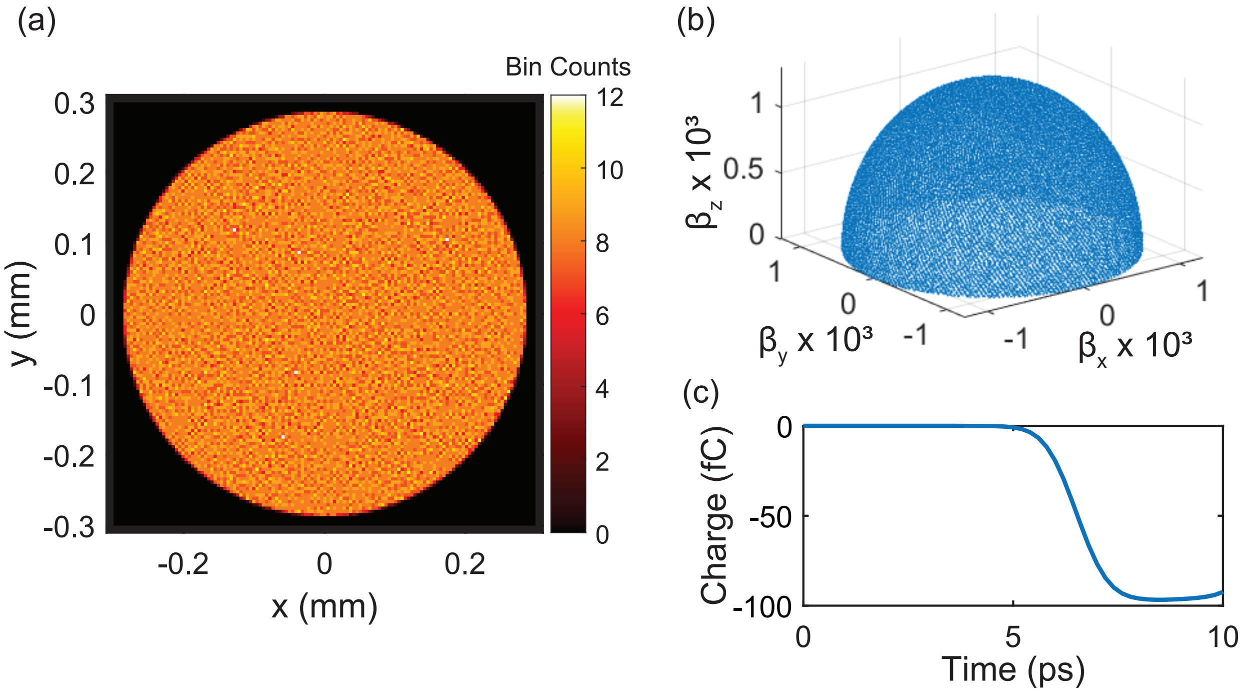

Figure 3.15: Uniform (a) spatial and (b) angular distribution of the beam. This distribution combined with the time distribution are used to generate the beam in GPT. (c) The charge buildup during emission. The full value of 103 fC is not quite reached due to some of the particles emitted at poor phases being lost almost immediately.

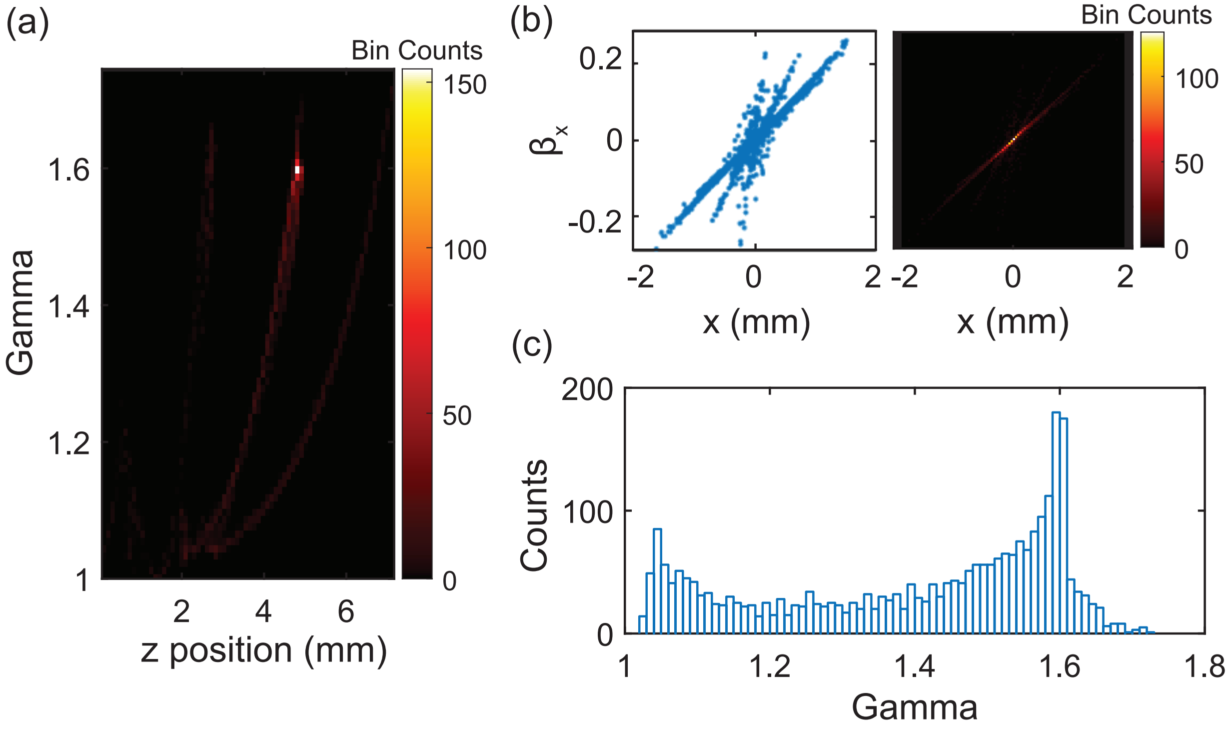

Figure 3.16: (a) Longitudinal phase space after acceleration and a drift. Emission is only modeled for one RF cycle, but takes place over a large range of sub-optimal phases which results in the large spread in z. (b) Scatter and density plots of the transverse phase space after acceleration and a drift. The beam is diverging, which is expected because there is no attempt at focusing within the gun cells. The beam is symmetric in x and y and thus only x-β_x is shown. The large spread in z is visible in the different phases visible in the scatter plot. (c) Histogram of the final energy distribution. The clear peak is at around $\gamma = 1.6$ or 305 keV, rather than the maximum achievable value.

3.5.2 Copper tip

Field emission from copper is well-described by the Fowler-Nordheim equation. An emission model for the copper tip was developed based on calculating the current from the Fowler-Nordheim equation at discrete points on the tip surface. The model uses each point to represent a segment of surface area on the tip hemisphere. The net charge is calculated based on the sum over all the phase and space steps. Figure 3.17 shows the distribution of the points along the tip, from the center to the end of the 50 μm rounded portion. Figure 3.18 shows the emission at each point versus phase.

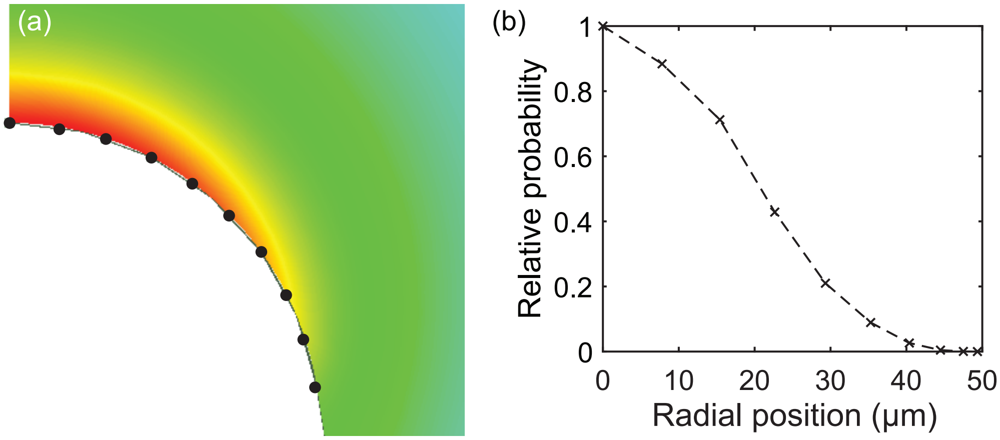

Figure 3.17: (a) HFSS electric field on the tip showing the points which were used to discretize the emission area. (b) Relative probability of emission at those points based on the current density calculated from the Fowler-Nordheim equation.

The emission area is considered to be the full hemisphere of the 50 μm radius tip. Each line in Figure 3.18 represents a ring of surface area between two points. The charge per cycle for 500 kW of input power was calculated to be 51.3 fC. Averaged over one RF cycle (9.1 ps), this is equivalent to 5.6 mA. This calculation does not include any field enhancement beyond the directly calculated surface field on the tip. In reality, surface finish and small features will cause further enhancement that would raise this value.

The initial beam parameters were set in a similar fashion to the diamond tip model but with added spatial variation. The relative probability of emission versus radius was calculated using the current density at each point from the Fowler-Nordheim equation. This distribution is shown in Figure 3.17b and was used for the radial distribution input in GPT. The fields are low enough at the edge of the tip that there is no significant contribution to the current. The angular distribution was assumed to be uniform in 2π sr. The cumulative spatial and angular distributions of the beam are shown in Figure 3.19. The density of particles is highest at the center, as is expected given the field variation on the tip. The time of emission was set using the normalized emission versus phase at the center, since the

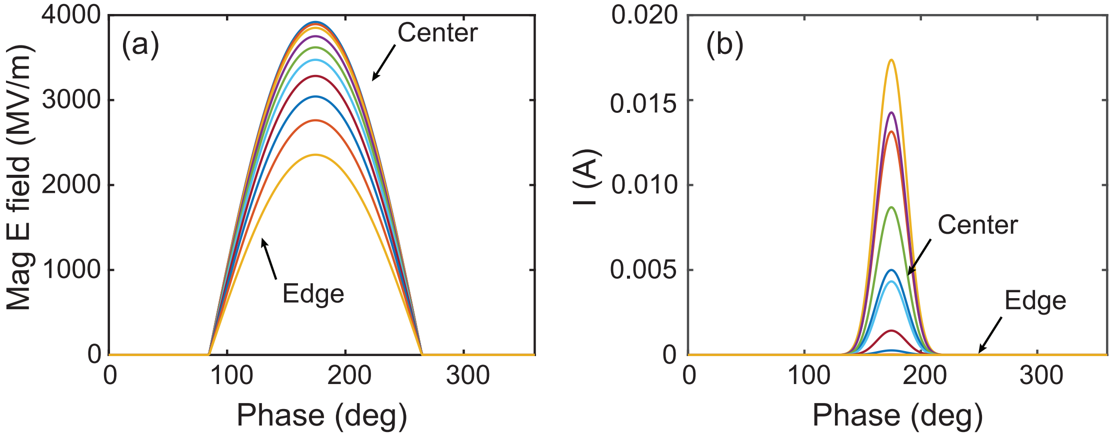

Figure 3.18: (a) Magnitude of the electric field at the points shown in Figure 3.17. Half of the RF cycle is shown which is the right orientation for acceleration. (b) The current versus phase based on the fields in (a). Most emission comes from the center and surrounding area. While the field is highest at the center of the tip, the current is higher at some points because they represent a larger area in a high-field region. The current density is highest at the tip center where the field is highest. The field is low enough at the edge of the hemisphere that it does not significantly contribute to the emission. This is reflected in the radial probability shown in 3.17b.

radial variation is included separately. All particles were assumed to be born at $z = 0$ with $E_0 = 0.4$ eV. Figure 3.19c shows the build up of charge versus time.

Simulations were performed using the full 3D, time-varying fields exported from HFSS. Like the diamond tip simulations, copper scattering boundaries and space charge were included. The results are shown in Figure 3.20. The maximum $\gamma = 1.717$ or 366 keV which matches with the prediction from single particle modeling (Figure 3.10) of 370 keV. There is a lower-energy tail, but it is much smaller than the diamond tip case. Roughly 74% of the particles fall within 5% of the maximum energy, and 85% fall within 10% of E_{max}. The normalized transverse rms emittance was calculated using the built-in GPT routine. The emittance for particles within 5% of the peak energy is $\epsilon_N = 0.88$ mm-mrad and for particles within 10% of the peak it is $\epsilon_N = 1.04$ mm-mrad. This is on par with typical photocathode values and is the expected order of magnitude for a 50 μm radius tip.

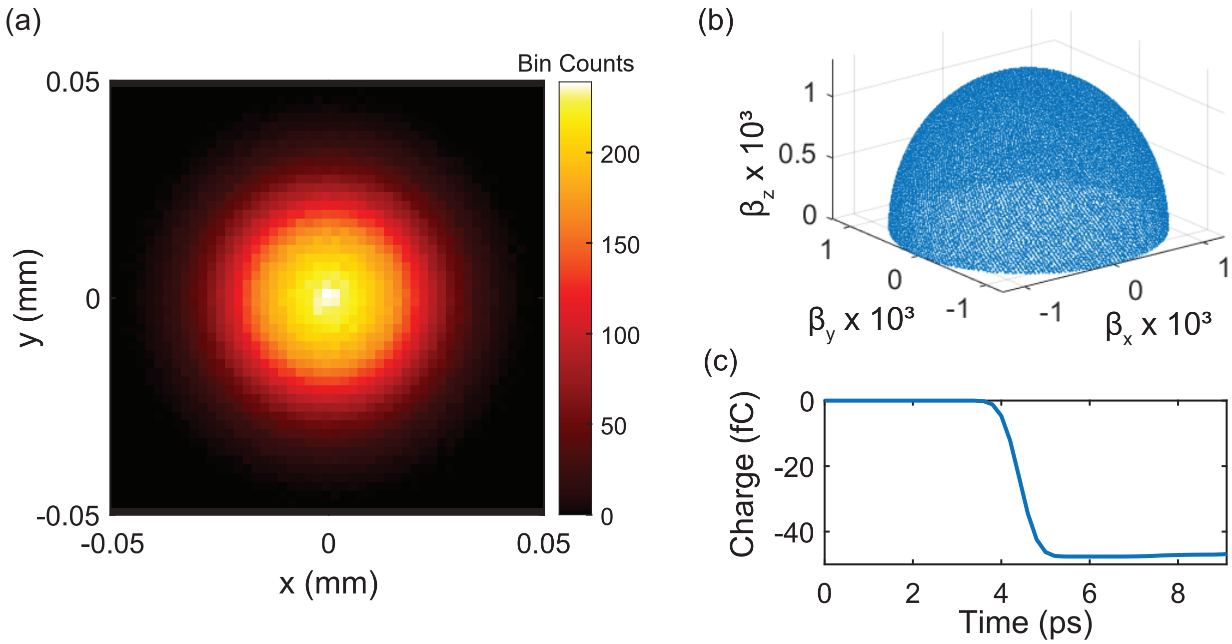

Figure 3.19: (a) Spatial and (b) angular distribution of a beam. The radial distribution is set by the relative probability shown in 3.17b. Emission is concentrated in the center and there is very little emission at the edges. (c) The build up of charge versus time based on the emission versus phase shown in Figure 3.18. As in the diamond tip case, the maximum value is never completely reached because some particles are lost while others are being emitted. One RF cycle is shown.

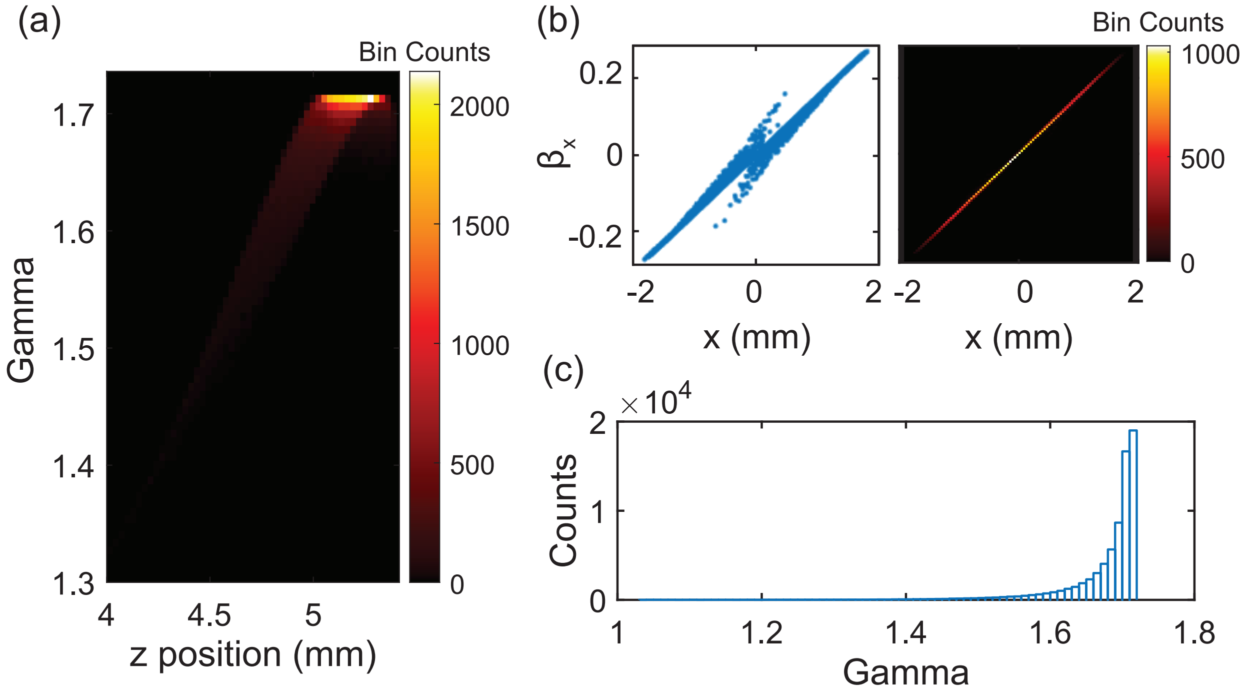

Figure 3.20: (a) Longitudinal phase space after acceleration and a drift. The peak is highly localized near the maximum achievable energy. (b) Scatter and density plots of the transverse phase space after acceleration and a drift, showing the beam diverging. The beam is symmetric in x and y and thus only x-β_x is shown. (c) Histogram of the electron energy distribution. The clear peak is at around $\gamma = 1.71$–1.72 or about 365 keV, very close to the single particle prediction. The energy bins are $\gamma = 0.01$ or roughly 5 keV. The dashed lines indicate the cutoffs for 5% and 10% energy spread from the maximum value.

Chapter 4

Fabrication and cold testing

4.1 Introduction

Fabrication of THz structures is an area of active research in addition to research focused on their use. For devices operating ~ 0.1 THz, the overall structure sizes are large enough to be within the range of conventional machining. While some individual features can be too small to be reliably machined, traditional microwave-like structures perform well and integrate with existing sources at this low end of the THz regime. Successful development of a 110 GHz accelerator or electron gun requires investigation into the fabrication of these components.

Multiple techniques were used in fabricating the structures presented in this thesis. The Gaussian horn/mode converter was fabricated using CNC machining. The gun cells were made from diamond turning and electroforming. Some electrical joints rely on clamping while others require brazing. This chapter discusses the method of fabrication for each structure and characterizes the resulting performance. The structures were measured with low input RF power using a network analyzer, referred to throughout as 'cold testing'.

The mechanical tuning of individual THz-frequency accelerator cells has not been previously demonstrated. An effort was undertaken to study different methods of tuning the gun cells including plating, etching, and mechanical deformation. The results of this study are detailed in this chapter as well as further modeling to understand the causes and effects of various behavior.

4.2 Mode converters

4.2.1 Gaussian horn and mode converter

The electromagnetic design of the Gaussian horn and mode converter was presented in Section 3.4. It consists of a Gaussian horn and a TE_{11} to TM_{01} circular waveguide mode converter and is designed to couple the output of the 110 GHz gyrotron into the gun cells.

The circuit was fabricated in two halves using CNC machining on a copper block. Additional machining was performed after the braze to add alignment features and flange mounts. A model and photo of one half of the block are shown in Figure 4.1. Photos of the completed block compared to the model are shown in Figure 4.2.

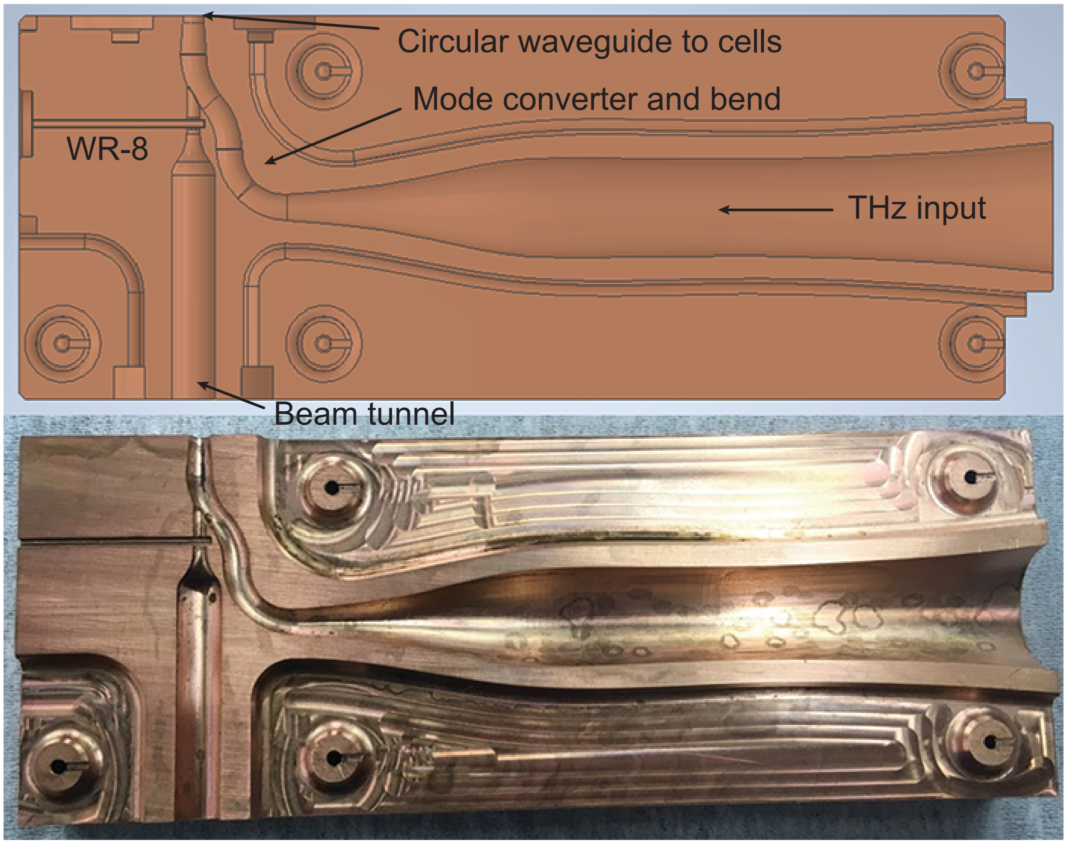

Figure 4.1: Model and photo of half of the Gaussian horn/mode converter block. This model shows features that are post-machined after the block is brazed, including alignment features and flange mounts.

The performance of the horn was characterized by measuring the output of the Gaussian horn excited by the circular waveguide, as indicated in Figure 4.1. The circular waveguide was excited using a coaxial probe. Measurements were performed using a 4-port Vector Network Analyzer (Agilent Technologies N5242A PNA-X) and VDI extender heads with an operating range of 67–115 GHz. Port 1 acted as a transmitter and receiver, while port 2 was a receiver only. The output profile of the Gaussian horn was measured by mounting the receiver head on a 3-axis motorized scanner. A cut WR-10 (75–110 GHz) rectangular waveguide was used on the receiver to sample the field with sub-wavelength resolution. The waveguide orientation provides polarization selectivity but measures all output modes.

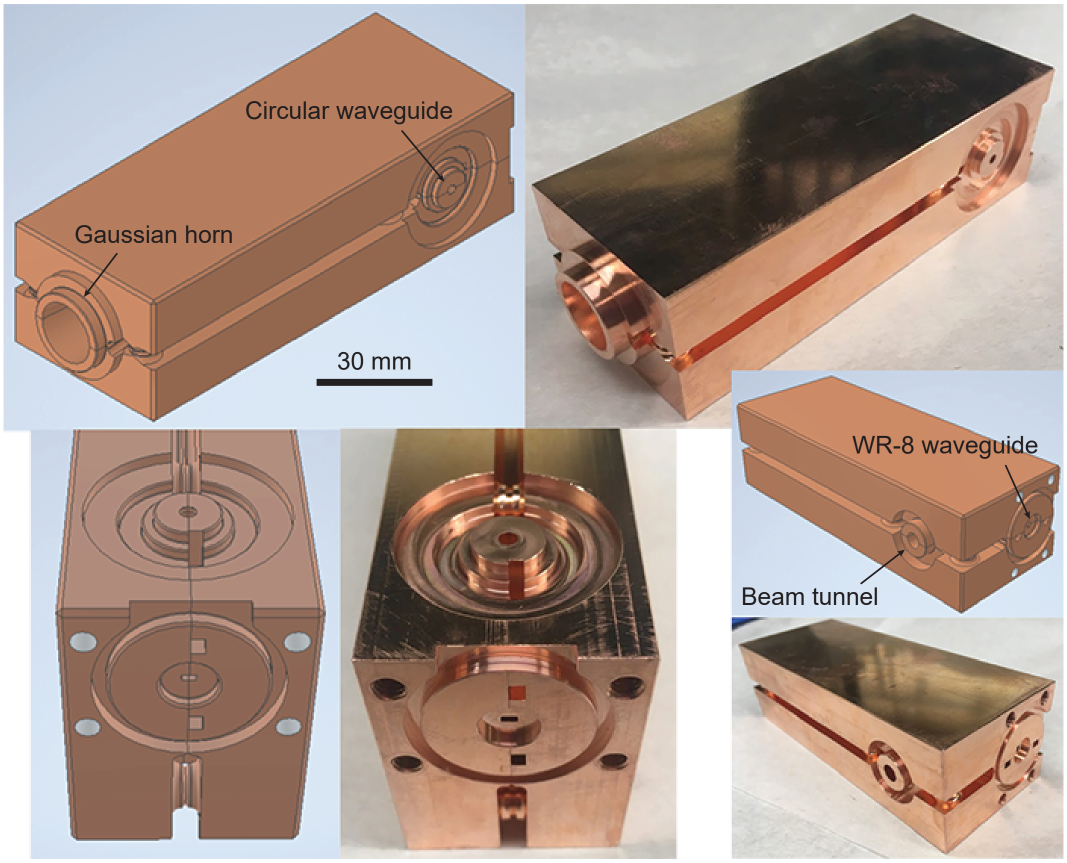

Figure 4.2: Model and photos of the brazed and machined Gaussian horn/mode converter block. The outputs of the Gaussian horn, circular waveguide, beam tunnel, and WR-8 waveguide are indicated. Vents to assist in pumping down are also visible.

Photos of this setup are shown in Figure 4.3.

Measurements were performed in a square x-y grid at a fixed z plane. The direction of propagation was z and the x-y plane was parallel to the horn aperture, as illustrated in Figure 4.3. Multiple scans were performed at different z distances from the horn to characterize the beam's spread. Results of one such scan are shown in Figure 4.4. The size of the Gaussian beam was calculated by summing the data in each direction and fitting it with a Gaussian function. To verify the performance of the horn, the beam was mathematically back-propagated using the measured complex fields and assuming the paraxial approximation. At each z distance in the back-propagation, the calculated field was summed and fit with a Gaussian function to measure the beam size. These results are shown in Figure 4.5. The measurement shown in Figure 4.4 was performed at $z = 38.1$ mm from the horn. Based on the back-propagated Gaussian, the calculated beam waist w_0 at the horn is 4.68 mm. This matches well with the design value of 4.5 mm.

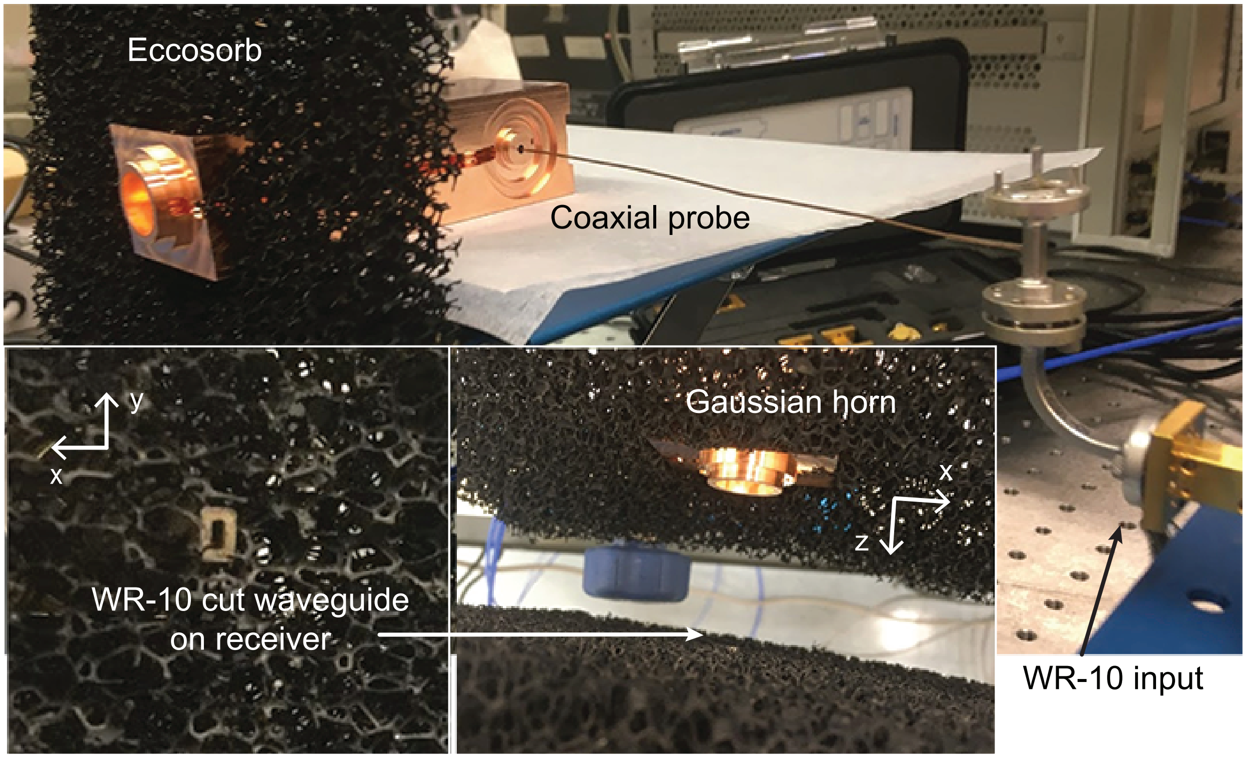

Figure 4.3: Photos of the horn and receiver for 3D scanner measurements. A microwave absorber (Eccosorb) was used to limit reflections.

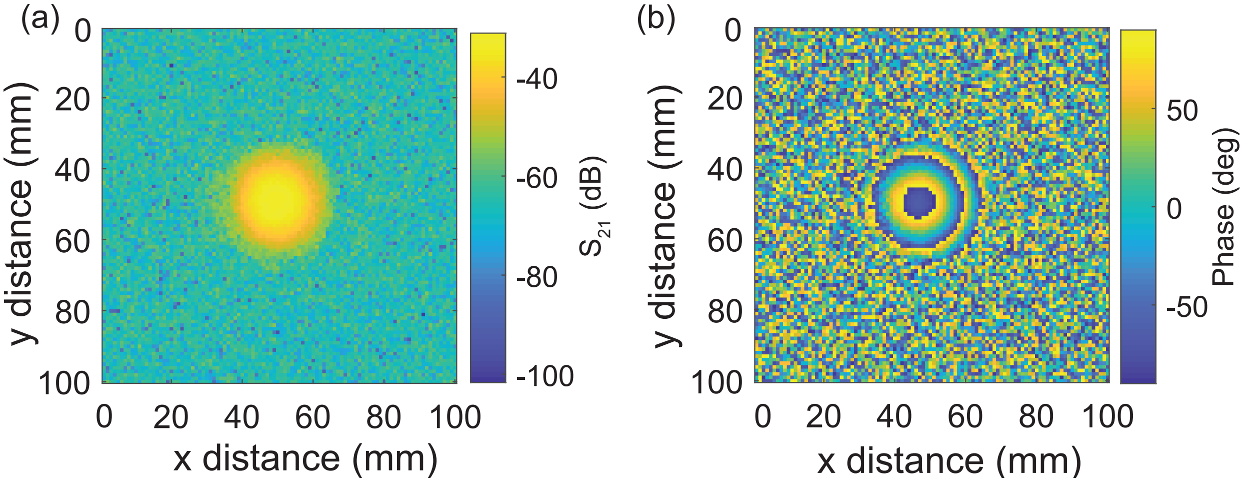

Figure 4.4: (a) Magnitude of transmission (S_{21}) measured at the receiver in dB versus transverse position. (b) Phase versus transverse position. Both plots are at f = 110.08 GHz.

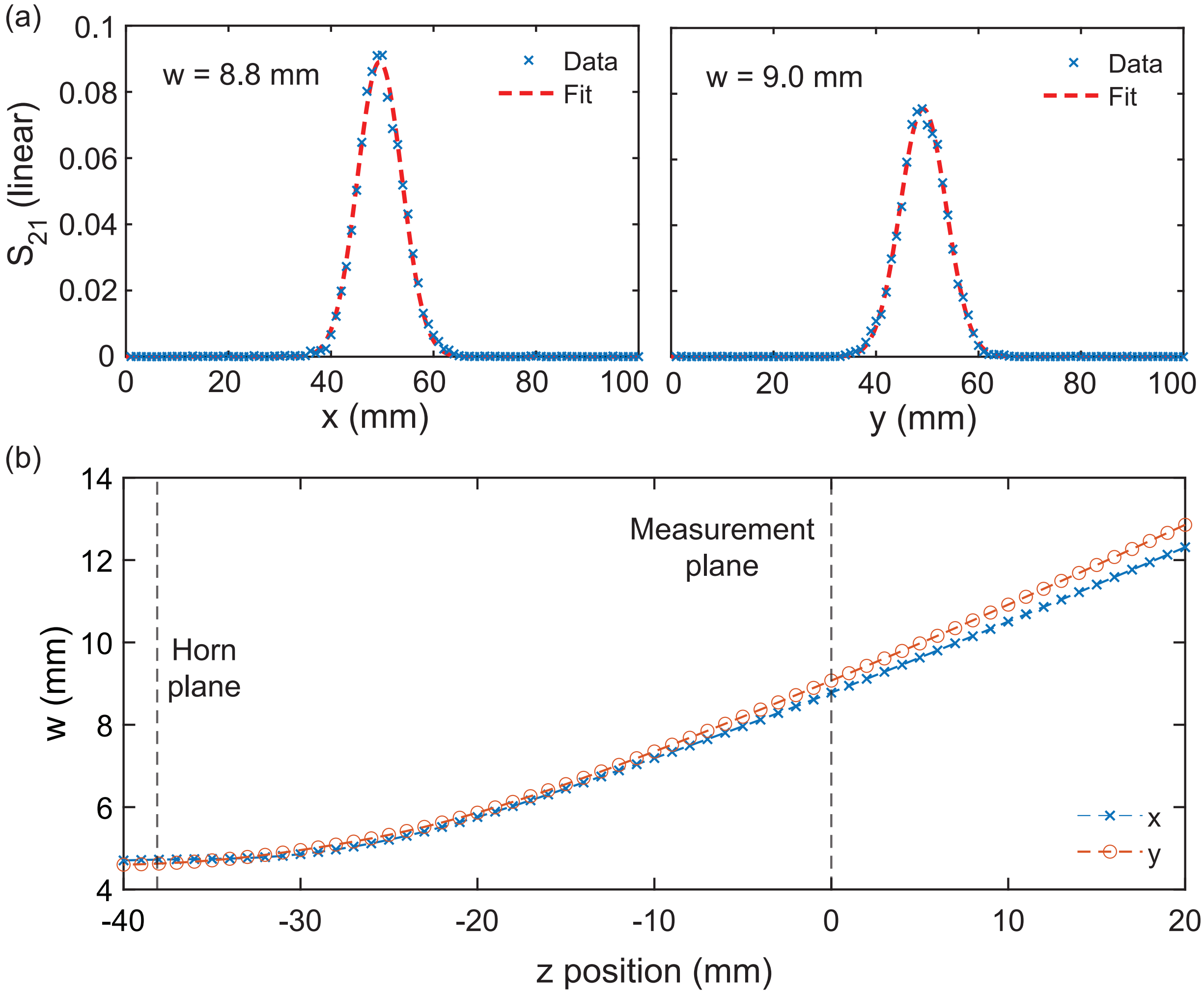

Figure 4.5: (a) Summed data in x and y fit with Gaussian functions. The resulting value for the width is also reported. (b) Back-propagation of the Gaussian data. The dashed lines indicate the measurement plane ($z = 0$) and the horn plane. This measurement was performed 38.1 mm from the horn opening. The resulting $w \approx 9.0$ mm matches well with the expected Gaussian propagation of a $w_0 = 4.5$ mm beam. The value calculated by back-propagating the measurement is $w_0 = 4.68$ mm, which also agrees well.

4.2.2 Cold test mode converter block

In order to cold test the gun cells without the full Gaussian horn and mode converter, a simple rectangular to circular waveguide copper mode converter was designed. The block was CNC machined in two halves which are clamped together for measurements. A model and photos of the block are shown in 4.6. The input port is a WR-10 rectangular waveguide which mates with the VDI extender head. The circular waveguide radius is 1.185 mm which matches the input waveguide on the gun cells. In addition to converting from a rectangular waveguide to a circular waveguide as needed to excite the cells, the mode converter serves as a 90 degree bend. The circular waveguide opening is oriented in the vertical direction so cells can be placed on top. A circular alignment feature is included to center the cells on the waveguide. Figure 4.7 shows the the modeled and measured reflection from the WR-10 port (S_{11}) with the block alone.

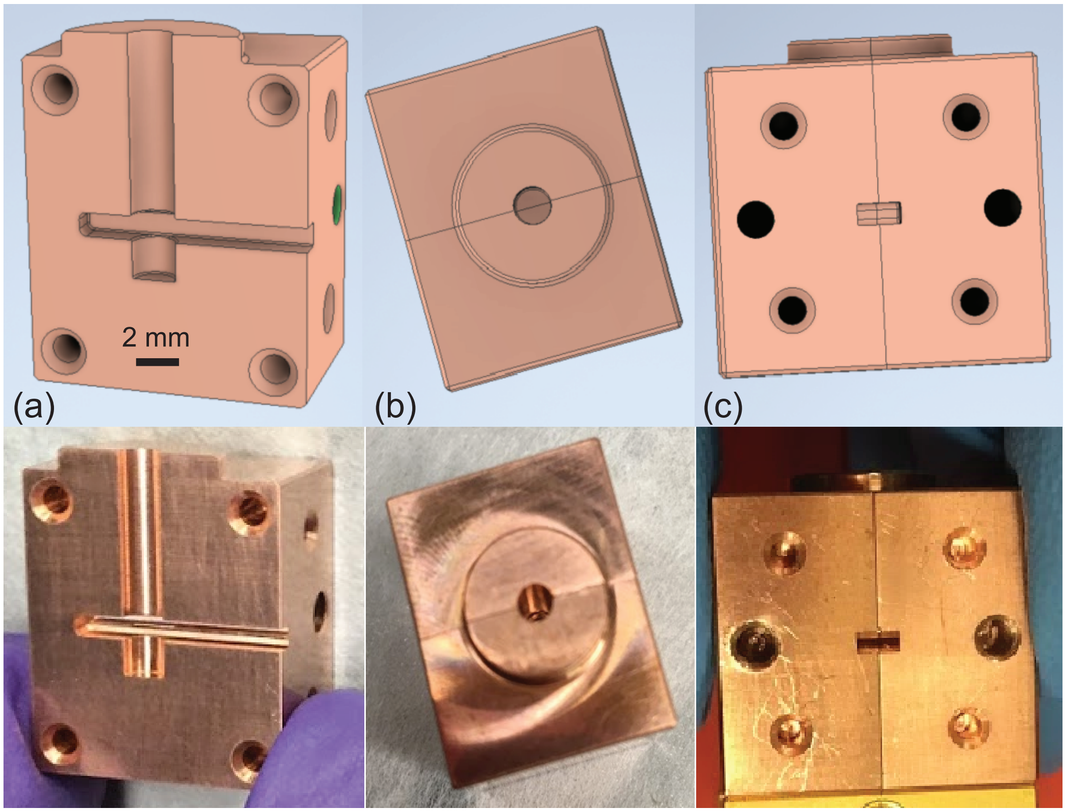

Figure 4.6: Model and photos of the cold test mode converter. (a) Half section showing circular and rectangular waveguide. (b) Top-down view of circular waveguide and alignment feature for gun cells. (c) WR-10 waveguide port.

Two resonances exist in the block that are largely independent of the cavities. The placement of the two modes changed from the initial design value due to necessary rounding

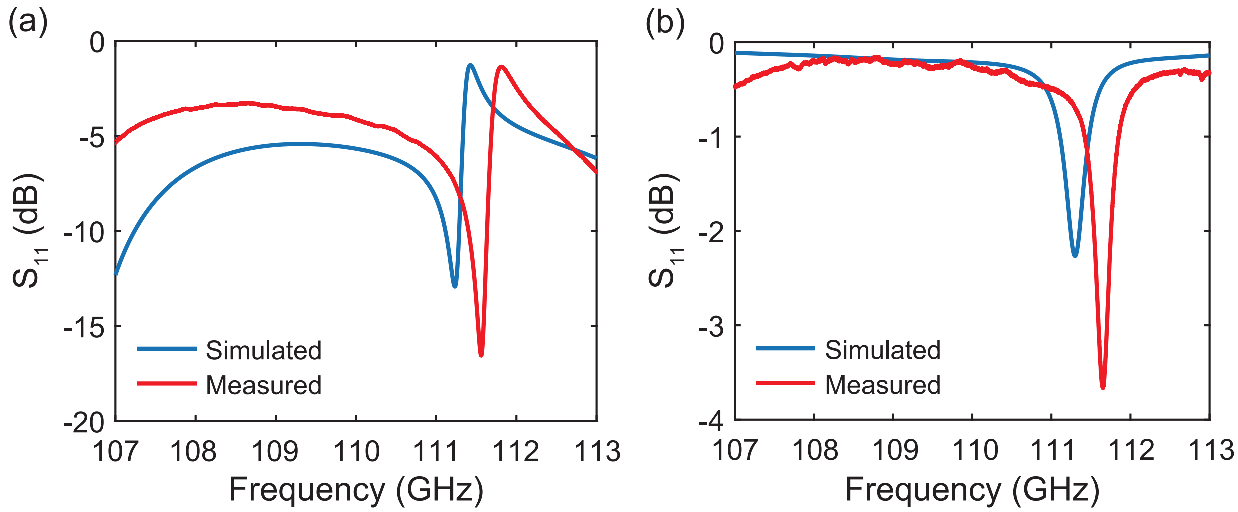

Figure 4.7: (a) Simulation and measurement of S_{11} at the WR-10 port when the circular waveguide port is open. The simulation uses a radiation boundary at the end of the circular waveguide. (b) Simulation and measurement with the circular waveguide shorted. There is a slight shift in the resonance in the measurement and some additional losses.

of edges for machining. While the placement of these modes is not ideal, they provide useful standards to compare with cell resonances because their frequencies are primarily determined by the block. When comparing different methods of tuning and measuring the gun cells after each step as in Section 4.5, the block mode frequencies are the same across all of the structures. The frequencies of the block modes can be shifted by slightly tightening or loosening the clamping of the two halves. The higher frequency block mode remains consistent over all methods of attaching the cells and is visible when the circular waveguide is shorted.

The lower frequency mode arises when the cells are attached and is heavily dependent on the method of attachment. The mode is strongest when the cells are slightly misaligned and there are additional reflections. It also appears at a lower frequency when there is a substantial gap between the cells and mode converter face or when the coupling section of the cells is longer, which is the case for the diamond tip cavities. Both modes appear in simulations, and the resulting field plots can be used to distinguish them from the pure cavity resonances. This is discussed further in Sections 4.3.2 and 4.4.2.

4.3 Diamond tip cells

4.3.1 Fabrication details

The 2 cell diamond tip design described in Section 3.2.4 was selected to be fabricated. The geometry was split in the center of the first cell so the structure could be fabricated in two pieces: a main portion and a half cell plate to attach to the DFEA. The main body consisting of the second cell, coupling cell, and half of the first cell was fabricated using electroforming. First, the negative of the structure (equivalent to the vacuum space) is made as a mandrel using diamond turning. Copper is then electroformed onto the mandrel to the desired thickness. The aluminum mandrel is dissolved using sodium hydroxide. In this structure, the outer diameter of the electroformed piece matches the full size of the alignment feature around the circular waveguide. This should provide a large area of contact between the Gaussian horn/mode converter block and the cells. However, the thickness of copper required by this dimension and the high aspect ratio of the irises caused concern about void formation in the irises. An initial layer of copper on the mandrel forms the surface of the iris. The area between the surfaces should be filled with copper, but gas or solution can be trapped. To counteract this, the iris volumes were back-filled with epoxy.

The other half of the first cell was machined into a thin copper plate. This portion was separated from the main body for the purpose of aligning the DFEA tip in the center of the irises. By keeping the plate separate, multiple methods of bonding the DFEA to the structure could be tested without damaging the other cells. Photos of the fabricated cells and plates are shown in Figure 4.8. In total, 7 cell pieces and 5 plates were fabricated.

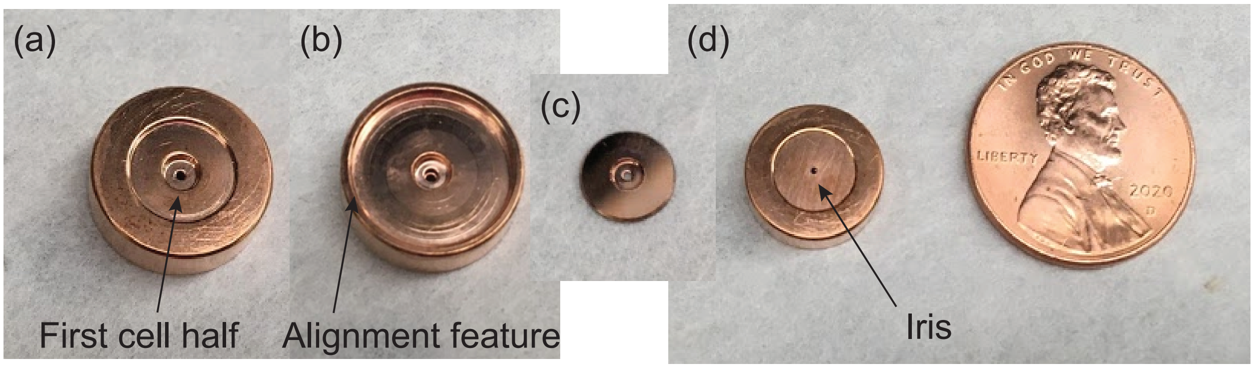

Figure 4.8: Photos of a fabricated diamond tip structure. (a) Main cell body with half of the first cell and iris visible. (b) Main cell body showing coupling side with the alignment feature. (c) Plate containing the other half of the first cell and iris for the diamond tip. (d) Structure with half cell plate in place.

4.3.2 Cold tests with block

Cold test measurements were performed using the mode converter block described in 4.2.2. The WR-10 waveguide on the block was connected to the VDI extender using a straight section of waveguide. Since the main cell body mates with the alignment feature diameter, the structures were placed directly onto the circular waveguide block. Measurements were taken with and without weights to improve electrical contact, which did not have a significant effect. Photos of the cells on the block are shown in Figure 4.9.

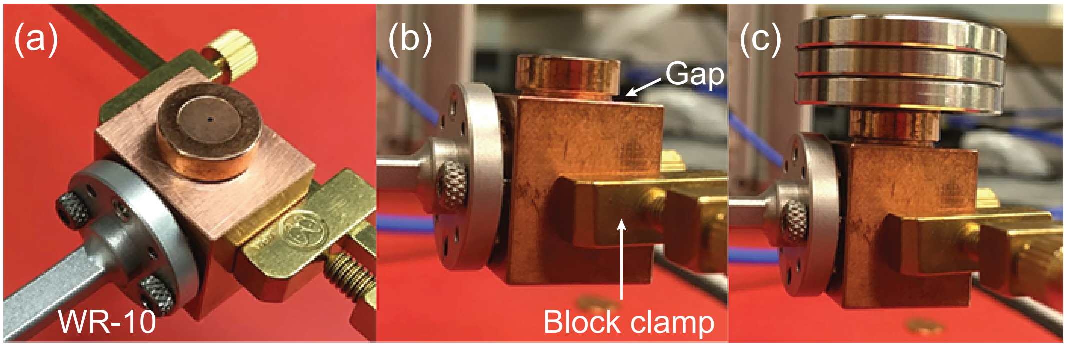

Figure 4.9: (a) Top-down view of the cells on the mode converter block. The half cell plate is visible in place on the main 1.5 cell body section. (b) Side view showing the size of the gap between the structure and the mode converter block. The two edges should be nearly flush for the waveguide sections to be in contact. (c) Side view with weights added for electrical contact. This did not change the measurements from the case with no weights.

On several of the structures, the inner diameter of the alignment feature was slightly undersized, making it difficult to fully mate with the coupler block face. This complicates the cold test measurements by introducing additional reflections which shift the block mode frequencies from their expected values. Overall, only three peaks were observed. The results for all of the structures are shown in Figure 4.10. The shape and placement of the highest and lowest modes indicate they are due to the mode converter resonances and additional reflections. This was confirmed by changing the clamping tightness on the mode converter block which shifts the frequencies of the block modes. These results are shown in Figure 4.11a for structure 7. Structures 2 and 7 fit the mode converter block the best. The difference in the block mode frequencies from measurements of structures 2 and 7 compared to those of the other structures demonstrates the effect of reflections due to misalignments and gaps. All structures were tested with the same half cell plate.

The center mode varies across the 7 structures and appears to be a cavity mode. It does not change frequency when changing the block clamping, which is characteristic of a cavity resonance. Its frequency is below the π mode design frequency of 109.17 GHz, but above the o mode frequency of 108.56 GHz. The range of frequencies is 108.66–109.11 GHz. As an additional test, structure 7 was tested with all 5 half cell plates. This result is shown

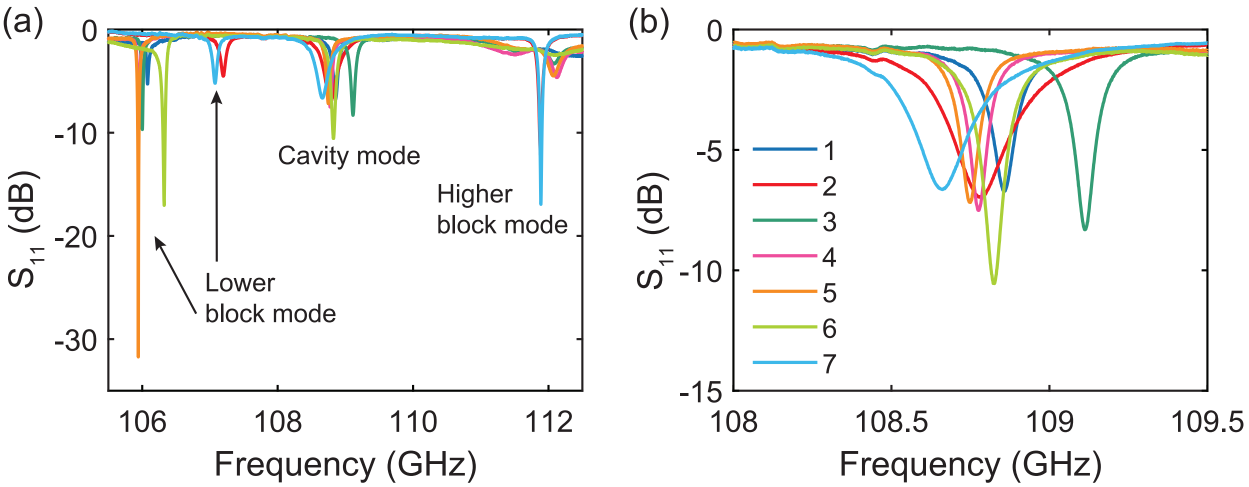

Figure 4.10: (a) Measured S_{11} across a wide window for the 7 structures. There are two resonances which are likely due to reflections and the mode converter block modes. The center resonance appears to be due to the cavity and varies across the 7 structures. The frequencies of the block modes vary because each structure has a different gap between the mode converter and the circular waveguide. (b) Zoomed view of the suspected cavity resonance.

in Figure 4.11b. All 5 plates give the same mode spectrum. The structure was also tested without a half cell plate, using only the main cell body containing 1.5 cells and the coupling section. The result matches the other measurements, indicating that only the 1.5 cell section is contributing to the resonance.

Simulations were performed to verify this hypothesis. Figure 4.12 shows the results of simulations of the diamond tip structure on the mode converter block with and without the half cell section. While the block modes appear at the same frequency, there is one resonance between the o and π mode resonances, which is expected for an effectively one cell structure. In simulation, the block mode frequencies depend on the length of the circular waveguide section. The diamond tip cells contain a longer circular waveguide coupling section than the copper tip cells, and thus the block modes appear at difference frequencies in the two cases (see Section 4.4.2). The lower block mode in the diamond tip measurements appears much lower in frequency, which matches the measurements.

Additional simulations were performed to study the effect of a gap between the half cell and 1.5 cell sections. These results are shown in Figure 4.13 for two types of boundaries. The first had a conductive (reflective) boundary on the edge of the gap, modeling the effect of a gap otherwise surrounded by metal. The second case had a radiation (open) boundary on the edge of the gap. When the gap is left open to radiate, it reproduces the same modes as the 1.5 cell case. The conductive boundary restores two cavity modes, though the gap causes a shift up in frequency. The measurements appear to match the open case, since the

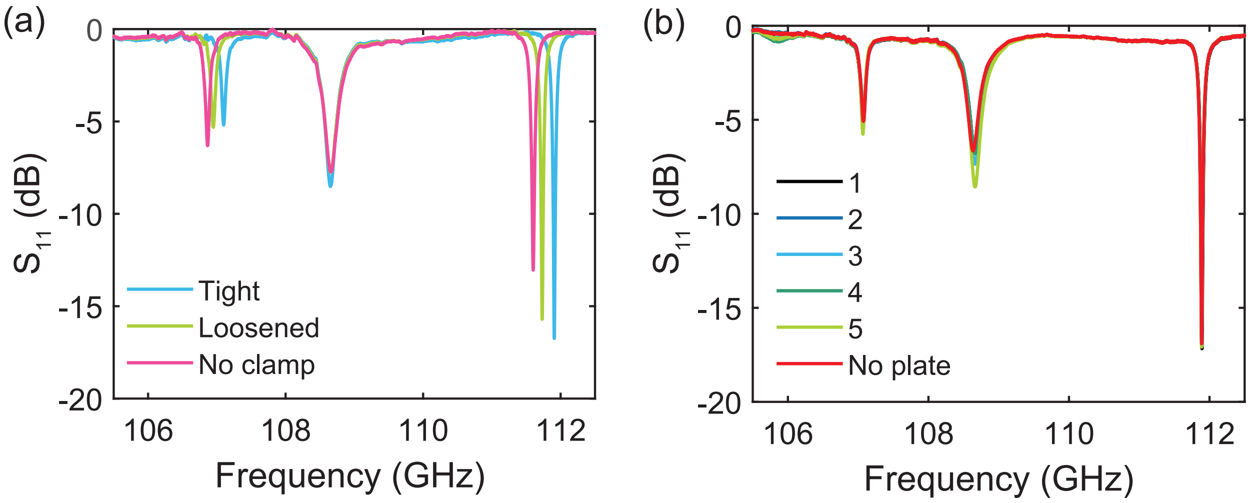

Figure 4.11: (a) Measured S_{11} of structure 7 with varying clamping tightnesses of the mode converter halves. Measurements were taken with the clamp fully tightened, a loosened clamping, and without the clamp. The two suspected block modes tune, indicating that they are in fact due the mode converter resonances. The center mode does not tune, which is expected for a cavity mode. (b) Measured S_{11} of structure 7 with each of the five half cell plates and no half cell plate. The only difference is a small change in the strength of the mode, indicating that this resonance is a result only of the 1.5 cell main body.

resonances with and without the half cell plate reproduce the same modes (Figure 4.11b). However, the o mode frequency in the reflective gap case is similar in frequency to the single mode in the 1.5 cell structure. Thus, it is possible that the π mode is present but too weakly coupled to be measured.

These results indicate the split design of a half cell plate and main electroformed cell body may not be able to reproduce the correct 2-cell resonances. Further measurements with different coupling and methods of ensuring electrical contact between the cell pieces are needed to determine whether the full 2-cell resonances can be restored. The accelerating π mode resonance requires participation from both cells, and the DFEA tip is inserted through the iris in the half cell plate. Thus, these structures could not be operated as a gun without improvements or modifications.

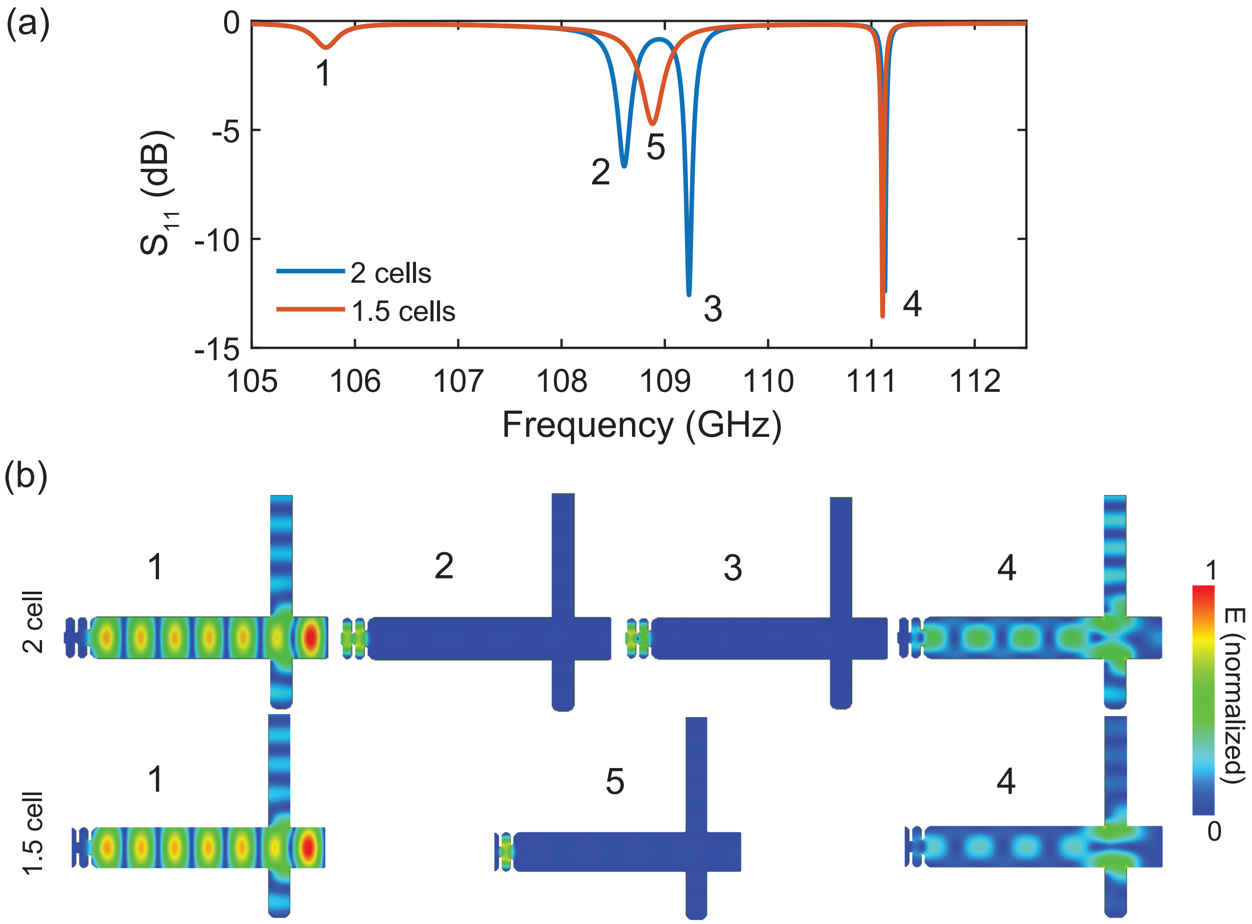

Figure 4.12: (a) Simulated S_{11} with the full two cell structure and without the first half cell. The 1.5 cell simulation used a radiation boundary to model the open face without the half cell plate. The block modes appear at the same frequency, but the sole resonance falls between the design o and π modes. This matches more closely with the measured spectrum. (b) Field plots of each mode. The highest and lowest modes (1 and 4) are the same in both cases and are the resonances in the mode converter block. Mode 2 is the original o mode and mode 3 is the original π mode. When the half cell is missing, there is only one resonance (mode 5).

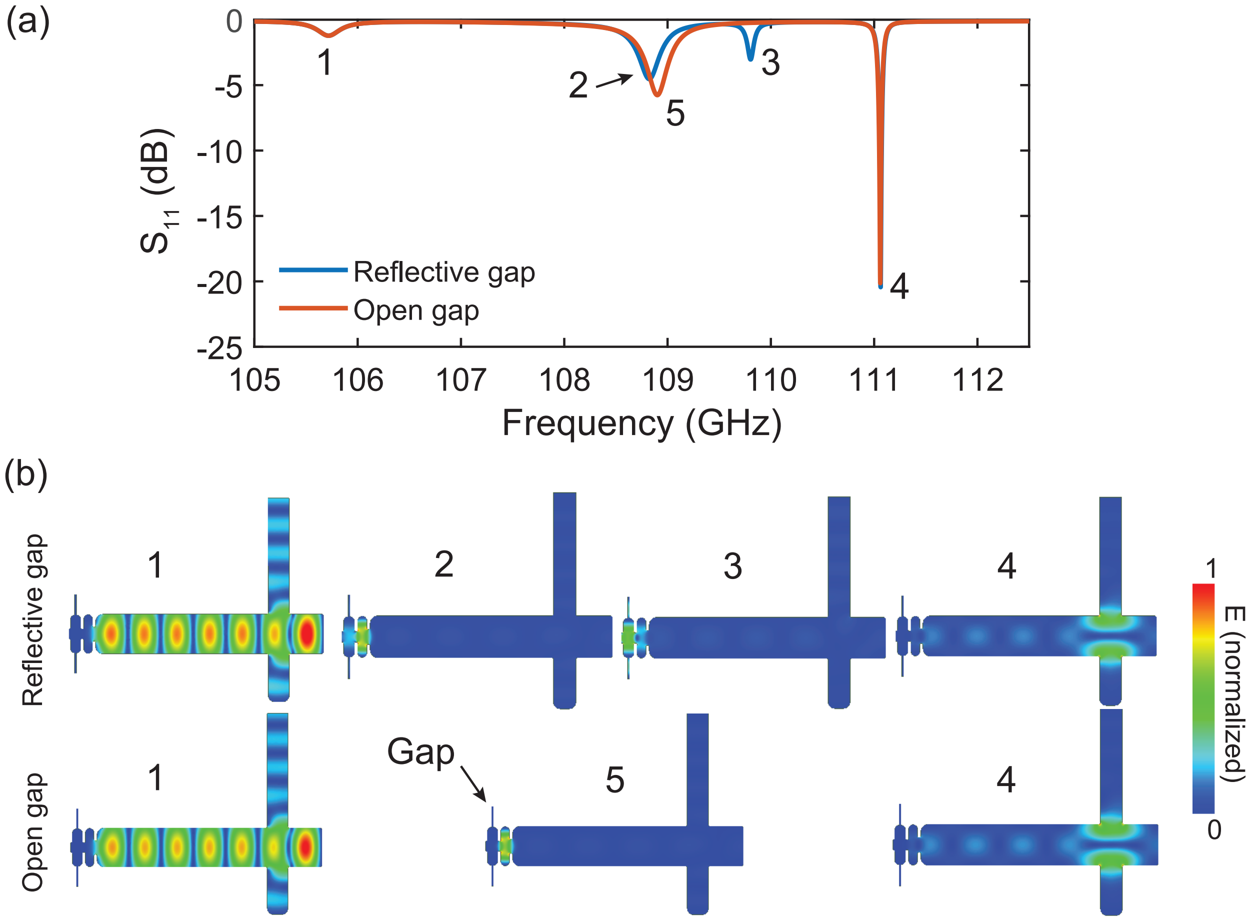

Figure 4.13: (a) Simulated S_{11} with a gap between the half cell and 1.5 cell sections. The reflective case uses a conductive boundary on the outside edge of the gap while the open case uses a radiation boundary. The reflective case preserves two cavity modes, but at different frequencies than the 2 cell modes. (b) Field plots of each mode. The highest and lowest modes (1 and 4) are the same in both cases and are the resonances in the mode converter block. Mode 2 is the o mode and mode 3 is the π mode. The gap changes the field balance between the two cells, but both resonances still appear. When the gap can radiate, only one resonance (mode 5) is supported as in the 1.5 cell case.

4.4 Copper tip cells

4.4.1 Fabrication details

For the copper tip gun structure, the cells and cathode were electroformed as one monolithic piece. The vacuum space (negative) of the cells was diamond turned into an aluminum mandrel. The shape of the tip was removed from the mandrel using electrical discharge machining (EDM). Copper was electroformed around the mandrel and the mandrel was dissolved.

Rather than the large outer diameter which was used for the diamond tip structure, the outer diameter of the copper tip structure was reduced to eliminate concerns about voids. The irises did not require any epoxy. The smaller diameter provides thinner walls which make mechanical tuning possible. This is discussed in further detail in Section 4.5.4. Selected photos of the fabricated structures are shown in Figure 4.14. Eight structures were tested in total.

Figure 4.14: Photos of the fabricated copper tip structures. (a) Cells with the coupling opening pointed up. The coupling iris and inner iris are both visible. (b) Back of the structure showing a divot for centering and alignment in the final assembly. (c) Cell structure upright in an aluminum adapter for cold testing. The adapter mates with the alignment feature on the cold test mode converter. (d) Zoomed photo where inner features are visible. The copper tip is visible in the center and the inner iris is also visible.

Since the outer diameter is much smaller than the alignment feature on the two mode converter blocks, a simple aluminum adapter was designed for cold tests (Figure 4.14c). In the full assembly for high power measurements, there are additional alignment tools and mounting hardware. This is discussed further in Section 5.3.

4.4.2 Initial cold tests with block

Each of the 8 structures was cold tested using the mode converter block described in Section 4.2.2. The block was connected to the VDI extender head using a straight section of WR-10 waveguide. Multiple methods of attaching the structure and adapter to the mode converter were tested to ensure good electrical contact. A clamp was used to lightly press the adapter and structure in place. Small weights were placed on top as an alternative method. Ultimately neither method changed the results of the cold test compared to the case of the structure and adapter resting on the block. However, all of the methods were used throughout cold testing for completeness. Photos of the cold test setup are shown in Figure 4.15.

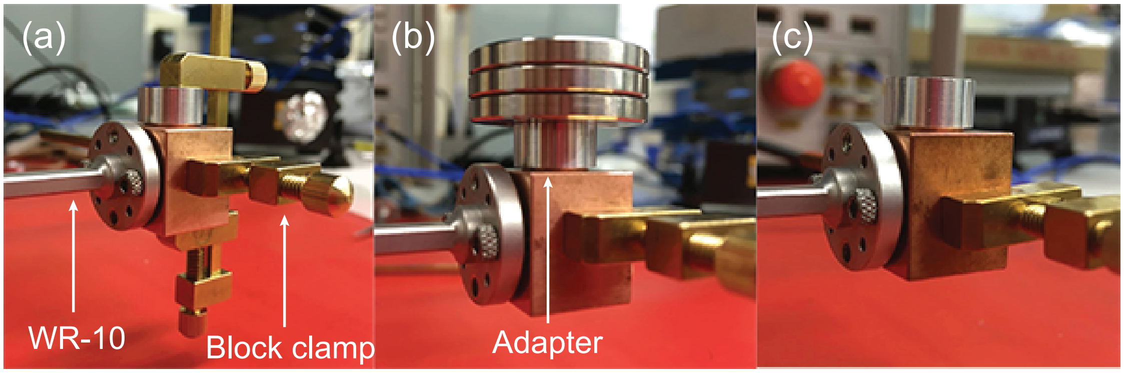

Figure 4.15: Photos demonstrating different methods of testing the copper tip structures: (a) the adapter containing the cells is clamped to the mode converter, (b) weights are placed on the adapter, and (c) the adapter is placed on the block but no additional force is used. No impact on the cavity resonances was observed with the different methods. This indicates there is sufficiently good electrical contact just from the placement of the cells onto the mode converter block.

Measurements of the 8 structures are shown in Figure 4.16. Four modes are visible over a wide window. As discussed in Section 4.2.2, two of these resonances are due to the mode converter block. Simulations were performed to verify the identity of each mode. Figure 4.17 shows the resulting S_{11} and field plots using the design values for the cells and mode converter. The highest and lowest frequency modes are the modes localized in the block. While they couple into the cells, their frequencies are largely determined by the mode converter block, which is clear in the measurements of all 8 structures.

The center two modes are the o mode and π mode resonances in the cells. Both resonances in all 8 structures were lower than their design frequencies. This led to the o mode being

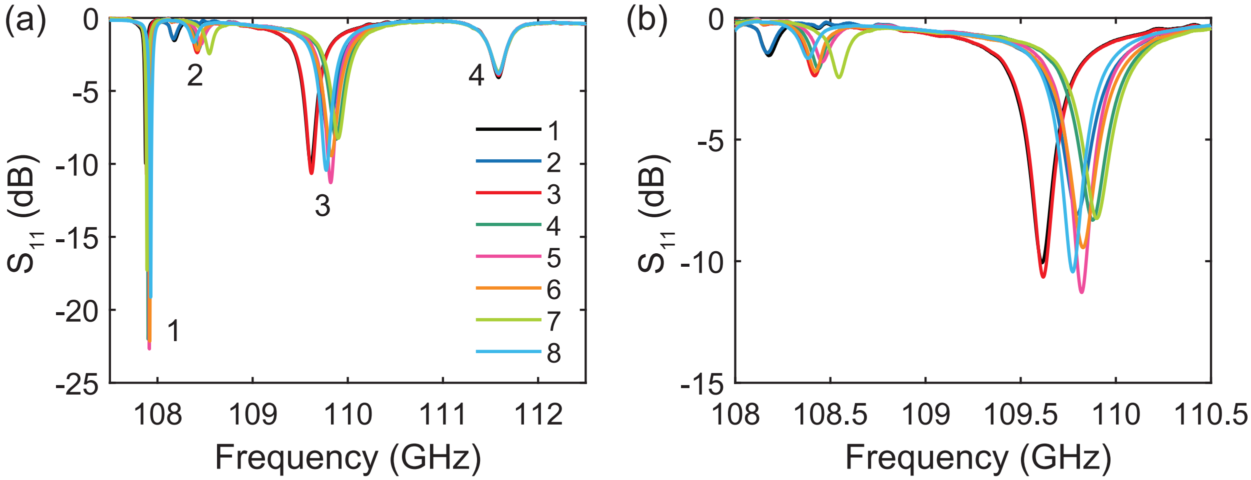

Figure 4.16: Cold test measurements of the copper tip cells. (a) Full window showing the lower block mode (1), the cavity o mode (2), the cavity π mode (3), and the higher block mode (4). The frequencies of the cavity resonances vary across the 8 structures. (b) Zoomed view showing only the cavity modes.

nearly the same frequency as the block mode in some cases, and thus they sometimes appear as one peak. Multiple measurements were performed with different tightening of the block clamping in order to shift the lower block mode and confirm this.

Most notably, the spacing and relative strength of the two cavity modes differ significantly from the design. The two modes are spaced much farther apart in frequency and the π mode is much stronger than the o mode. This was a valuable indicator of which dimensions deviated from the design values. A detailed study to understand this deviation is discussed in Section 4.5.1.

The measured frequencies of the cavity resonances in each structure are summarized in Table 4.1. The range of frequencies of the π mode is roughly 300 MHz. Overall, the highest frequency structure was structure 7 with $f = 109.9$ GHz, still over 100 MHz below the design value of 110.01 GHz. The lowest frequency structure was structure 1 at $f = 109.613$ GHz, roughly 400 MHz below the design value. This indicates that the cell radii are oversized compared to the design value. The difference could be as small as 2–4 μm if the cells are both oversized, or up to 10 μm if one is larger than the other. However, the frequencies do not depend solely on the cell radii. This is discussed in detail in Section 4.5.1.

This section focuses only on the initial cold test measurements of the cells before any alterations were made. Many additional measurements were performed throughout the tuning and characterization process. These are discussed in the following sections of this chapter.

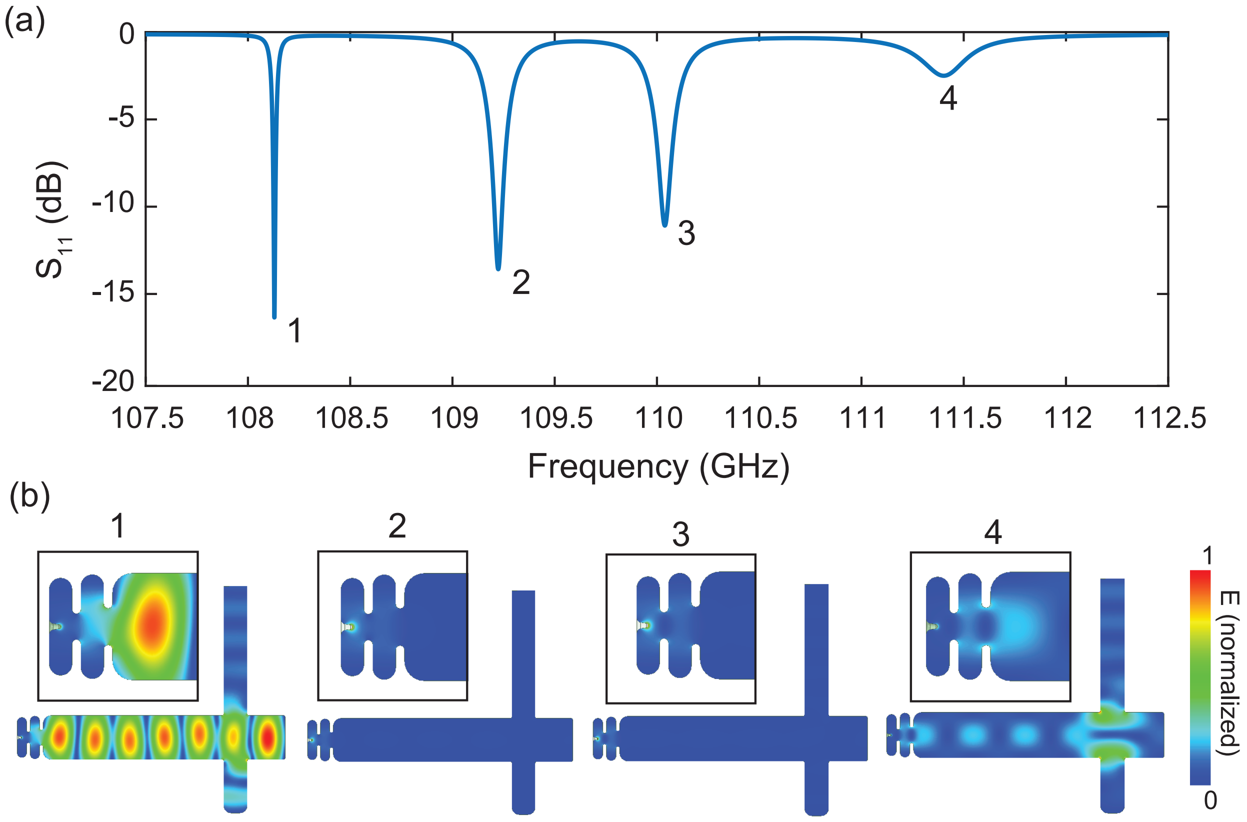

Figure 4.17: Simulation of the mode converter block with the copper tip cells. (a) The simulated S_{11} from the WR-10 port. The modes are numbered 1–4. (b) The magnitude of the electric field at each resonance. The insets show a zoomed view of the cells. The modes localized in the block arise in simulation, confirming the identity of the measured modes. While the block modes do couple into the cells, they only arise due to the geometry of the mode converter.

	Frequency (GHz)	
Structure	π mode	o mode
1	109.613	108.182
2	109.795	108.171
3	109.619	108.422
4	109.878	108.438
5	109.821	108.459
6	109.828	108.422
7	109.900	108.544
8	109.774	108.388

Table 4.1: Initial frequencies of the cavity resonances in the 8 copper tip structures.

4.4.3 Cold test with Gaussian horn

Cold test measurements on structure 5 were performed using the brazed Gaussian horn and mode converter block. These measurements were necessary to ensure the gun was properly coupling to block. The structure was excited using the WR-8 diagnostic port and the output beam profile was measured using the 3D scanner discussed in Section 4.2.1. The diagnostic port was excited using the WR-8 waveguide which is part of the full high power assembly (see Section 5.3). A WR-8 to WR-10 waveguide transition was used to connect to the VDI extender head. The receiver with a cut WR-10 waveguide was mounted onto the scanner. Photos of the setup are shown in Figure 4.18.

S parameter measurements were recorded on the VNA when the receiver was centered with respect to the horn. These measurements are shown in Figure 4.19. The 2D scanner results are shown in Figure 4.20. In the single-position S parameter measurement, there is a clear increase in the transmission (S_{21}) near the π mode resonance. The o mode resonance is not visible, likely because it is not well coupled in the fabricated version.

The 2D output profile of the horn differs significantly from the expected Gaussian profile. This is a result of power coupling into a higher mode of the mode converter and Gaussian horn. In typical operation, power is input in a Gaussian beam which couples to the TE_{11} mode at the start of the mode converter. When the structure is attached and the assembly is driven in reverse (from the diagnostic port), the majority of the transmitted power is in the second mode of the mode converter. This was determined with simulations, shown in Figure 4.21. The second mode of the mode converter section is the TM_{01}, resulting in a dipole-like mode at the output of the horn. The coupling to this mode is stronger or equal to the coupling to the TE_{11} mode over the entire frequency range of the scan, which matches with the observed output profile. The cavity resonances do not appear in the trace of the S_{21} to the second mode. In measurements, it is not possible to separate the S_{21} contribution from each mode, and thus the observed trace in Figure 4.19 is the total for both modes.

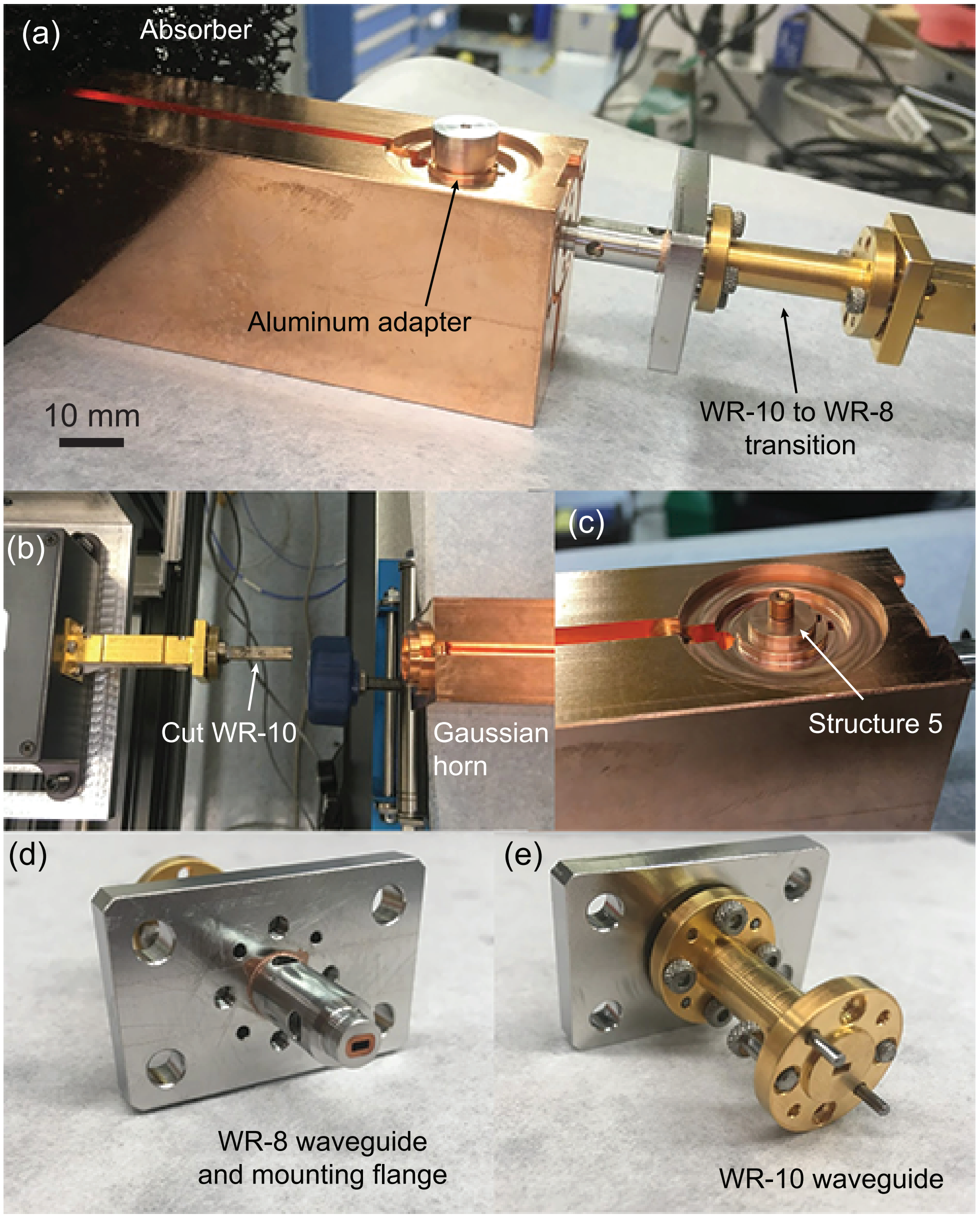

Figure 4.18: Photos of the cell cold test with the Gaussian horn/mode converter. (a) Gaussian horn/mode converter with the aluminum adapter containing the structure. The WR-10 to WR-8 transition and WR-8 waveguide used to excite the diagnostic port are indicated. (b) The cut WR-10 waveguide on the receiver. The receiver is mounted on the 3D scanner stage. This photo was taken while centering the receiver before adding absorbers around the waveguide and horn. (c) Structure 5 on the mode converter with the aluminum adapter removed. (d) The WR-8 waveguide section and mounting flange for the full assembly. (e) The WR-10 waveguide side of the transition.

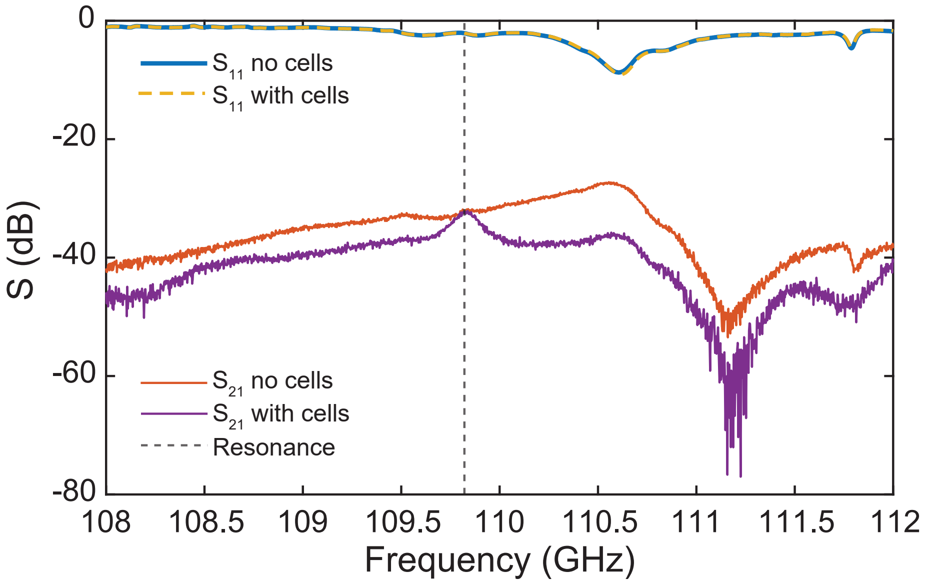

Figure 4.19: S parameter measurements of the Gaussian horn/mode converter block with and without the cells. Port 1 is the WR-8 diagnostic port and port 2 is the WR-10 cut waveguide on the receiver, measuring the output of the horn. There is little change in the S_{11} when the cells are added. However, a clear peak emerges in the S_{21} at the π mode resonant frequency. This measurement was performed with structure 5, which has $f = 109.821$ GHz. This resonance is marked by the vertical dashed line. There is no o mode resonance visible. It would appear at roughly $f = 108.46$ GHz.

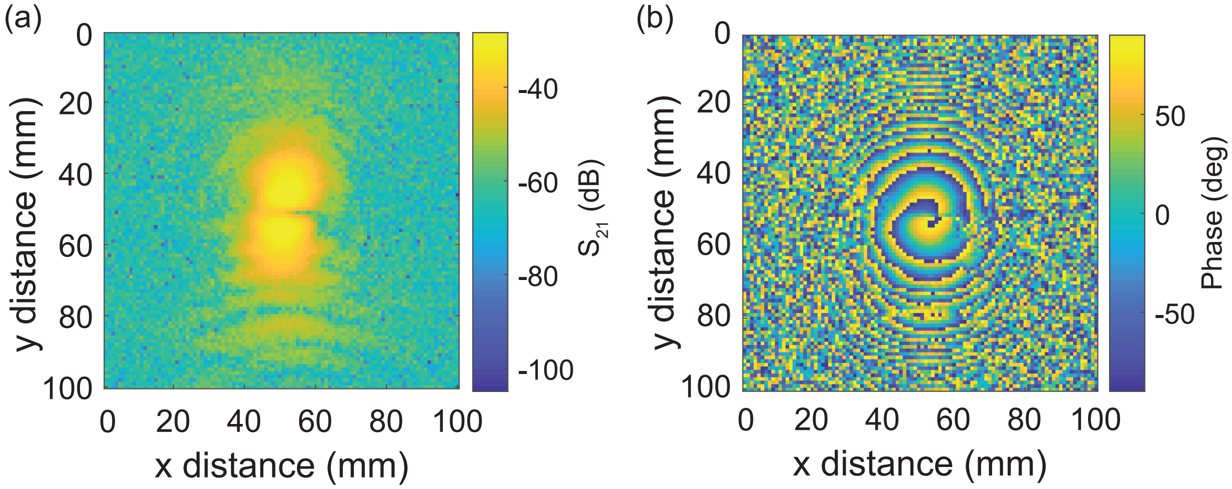

Figure 4.20: Scanner measurements of the Gaussian horn/mode converter with copper tip structure 5. (a) Magnitude of the transmission measured at the receiver versus transverse position. (b) Phase versus transverse position. These measurements are at $f = 109.838$ GHz, the maximum of the peak in S_{21}. This is close to the cavity π mode resonance in structure 5.

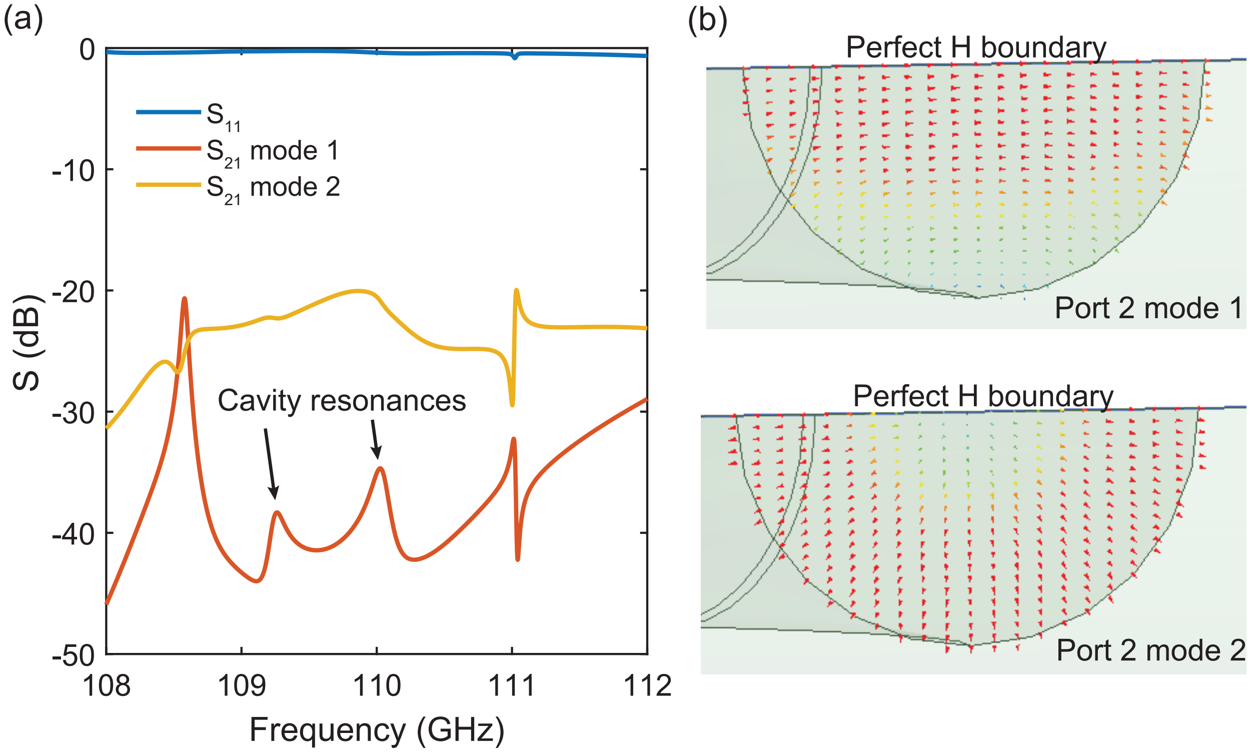

Figure 4.21: Simulation of the copper tip structure on the Gaussian horn and mode converter. (a) S parameters driven by the WR-8 diagnostic port. Here, port 1 is the WR-8 port and port 2 is the output of the mode converter which leads to the Gaussian horn. When the cells are present, power couples strongly into two modes. (b) The two modes in the mode converter. The top is the TE_{11} which the input Gaussian couples to most strongly. The bottom is the TM_{01} mode.

4.4.4 Microscope images and tip profile

Since the structures are electroformed as one piece, it is only possible to view the internal features looking down the axis through the circular waveguide. The coupling iris radius is larger than the inner iris, and so it is possible to view both. A Keyance VK-X1000 laser confocal microscope was used to image all of the structures. This microscope is also capable of collecting surface data which can be used to generate height profiles and measure surface properties. Each of the structures was imaged in detail before and after any alterations were made, such as the tuning discussed in Section 4.5.

Images of several structures are shown in 4.22. There was substantial variation in the surface finish across the 8 structures. There also appeared to be residual material, likely aluminum, left behind from the fabrication process. Some pitting is visible on the iris edges as well as the coupling cell surface. These features are likely a result of the chemical processing used to remove the mandrel. Any sharp edges will be rounded during the cavity high power processing.

The tip profile was also measured. In all 8 structures, the profile matched well with the design. The main variation across the 8 structures was the profile of the rounding at the end of the tip. In some cases, it was slightly flattened, but the overall tip radius still matched well with the design. Figure 4.23 shows an example and images. The dashed lines in the figure indicate 50 μm from the center of the tip and from the maximum height. The top is not a perfect hemisphere, but is close to the 50 μm radius of curvature design value. The height of this tip is 255 μm, which is exactly the design value.

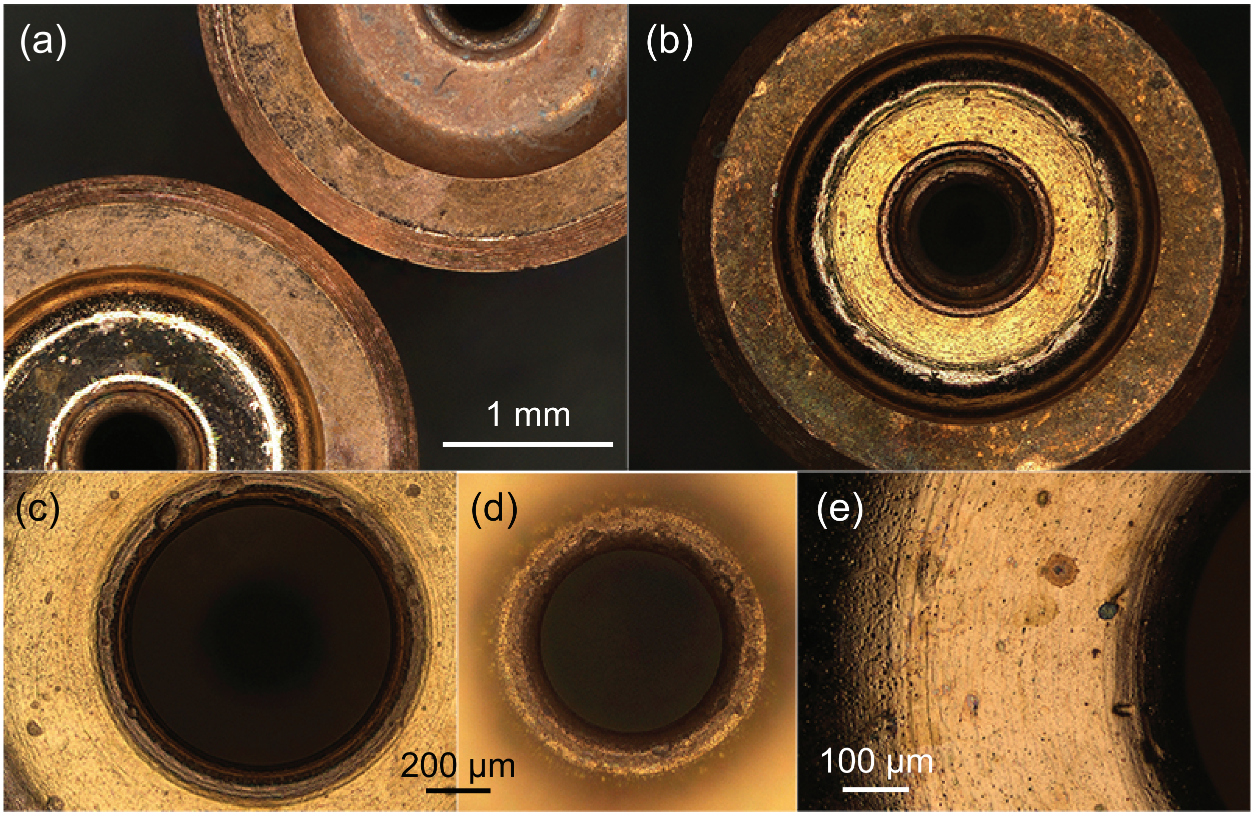

Figure 4.22: Microscope images of different copper tip gun cells. All of the images are stacked focus images. (a) Side-by-side comparison of two structures showing the different surface finishes. (b) Image of a structure showing both irises and the input coupling section. The surface finish on the outer surface which mates with the input waveguide shows more wear-and-tear than the cell surfaces. (c) Zoomed view of the coupling iris. There are pits visible in the iris. These features will likely be smoothed during high power processing. (d) The inner iris, viewed with the same magnification as (c). (e) Close-up view of the coupling iris edge and surface of the coupling cell.

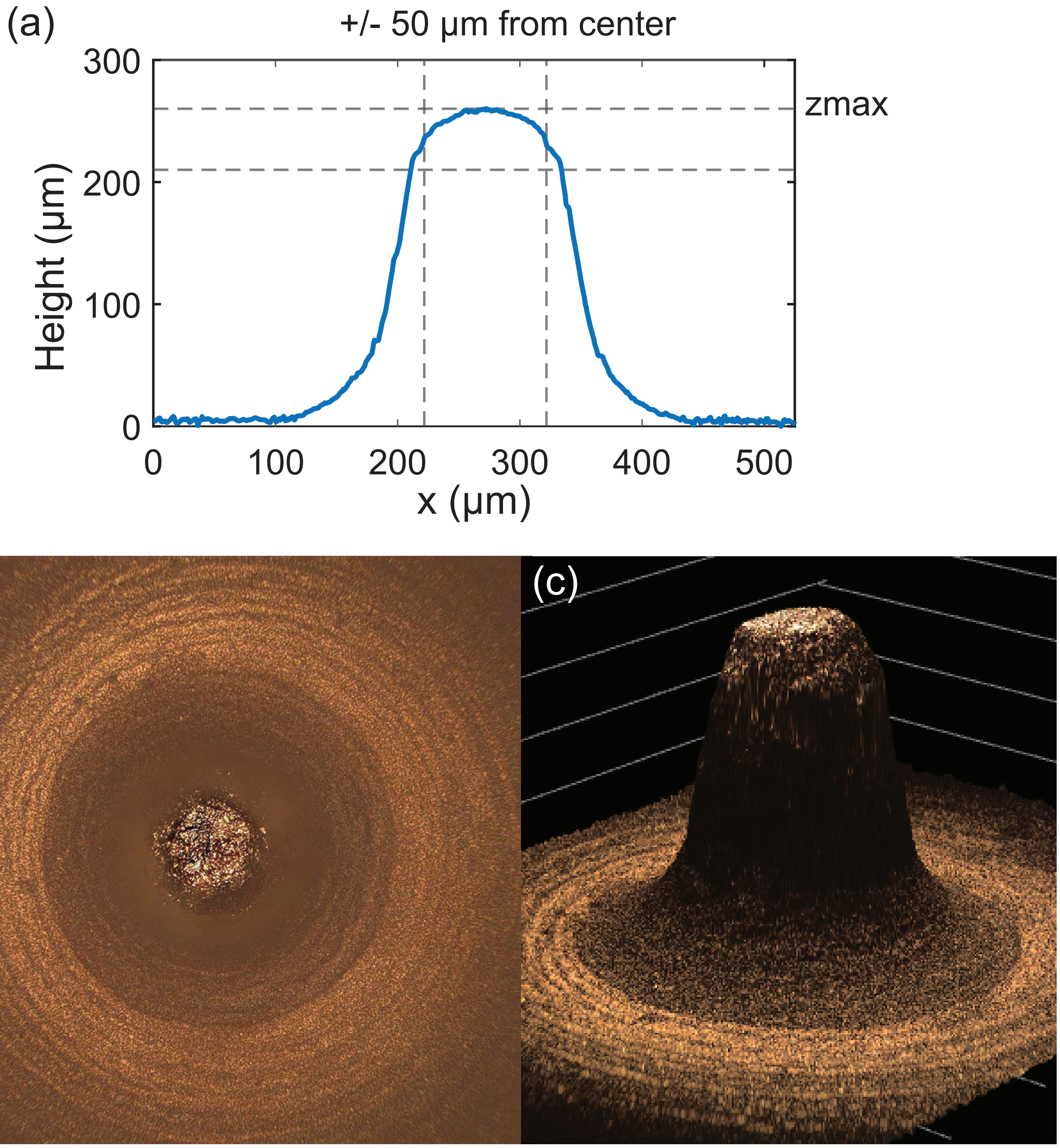

Figure 4.23: (a) Height profile through the center of a copper tip. The dashed lines indicate the height and the distance corresponding to a 50 μm radius. The tip is not a perfect hemisphere, but its overall size matches well with the design. The height from the baseline is 255 μm, which was the design value for the height. (b) Top-down view of a tip in a stacked-focus image. (c) Height data displayed in 3D form.

4.5 Tuning and simulation study

In order to drive the structure during high power measurements, the π mode frequency must be within the tuning range of the gyrotron. The gyrotron operates best between 110.08–110.1 GHz and its highest power operating point is 110.081 GHz. While the gun structure can be slightly tuned with temperature during operation, the measured frequency of the π mode was outside the feasible range in all 8 structures. Tuning of roughly 1.65 MHz/°C is predicted based on modeling of uniform thermal expansion/contraction. Thus, as-fabricated the 8 structures would need to be operated at cryogenic temperatures to be within the gyrotron operating range. This is not compatible with the planned experimental setup.

Mechanical tuning of W-band accelerator cavities has not been previously demonstrated. The standard method of tuning a cell by deforming the wall with a small pin is not compatible with these structures due to their small size. Further, the structures are electroformed rather than traditionally machined into solid copper. It cannot be assumed that the cavities would respond to any processes in the same way, since the electroformed copper may have different properties than solid copper. Several methods were explored to tune the structures in order to address these uncertainties. This section reports the results of these measurements as well as simulations performed to explain the observed changes.

4.5.1 Mode spacing simulations

The measured cold test results shown in Figure 4.16 deviate significantly from the simulated design, Figure 4.17. The net frequency shift indicates the structure is oversized, but the large shift in the mode balance and spacing indicates there are further deviations from the design. In order to understand the source of this disagreement and its potential impact on the gun performance, simulations were performed to recreate the measured result.

Mandrel-based HFSS models

Before the structures were electroformed, quality assurance measurements were performed on 10 fabricated aluminum mandrels. The measurements of the 10 mandrels varied. Overall the structures were undersized, including all of the radii. The inner iris radius had the largest deviation from the design value. There was a clear pattern in the lengths of the cells and irises: the cells were shorter than designed and the irises were thicker. The deviation in the length of the first cell was more significant than of the second.

Initial simulations were performed using the measured mandrel dimensions. Overall these produced higher frequency structures since the internal volume is smaller than the design. However, the actual electroformed structures can be larger than the mandrel due to intermediate layers used in the electroforming process and the chemical processing to dissolve the mandrel. Simulations using the mandrel measurements showed an increase in the mode spacing with a stronger π mode than o mode, though not as extreme as the measurements. A representative mandrel structure was chosen as the basis for a mode spacing study. The

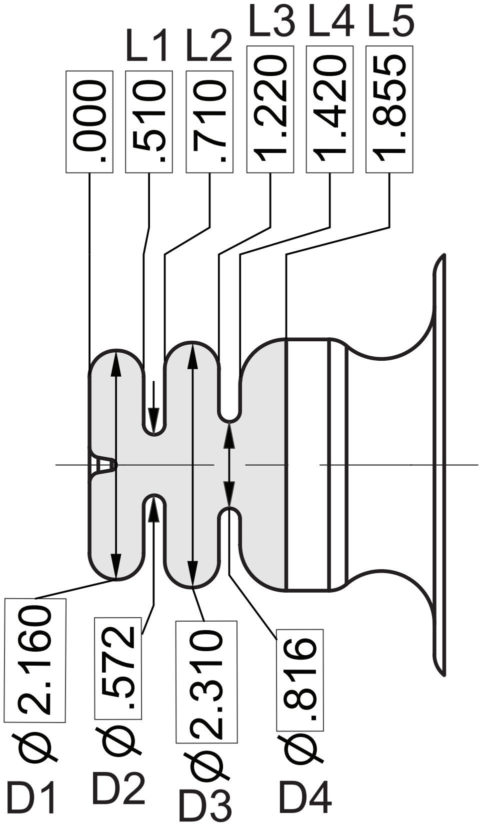

Figure 4.24: Drawing showing the definitions of the measured dimensions on the mandrel. The shaded region is the negative of the gun cells. The numerical values listed are the design values in mm.

Dim.	Meas. (mm)	Scaled (mm)
L1	0.500	0.502
L2	0.724	0.727
L3	1.213	1.218
L4	1.433	1.440
L5	1.802	1.810
D1	2.152	2.162
D2	0.551	0.554
D3	2.294	2.305
D4	0.794	0.798

Table 4.2: Dimensions as measured on the mandrel and scaled. The design values are shown in the figure. The measurements demonstrate that the cell lengths are smaller and the irises are thicker than the design. The cell and iris diameters were all undersized. When the mandrel dimensions are scaled such that the simulated π mode frequency roughly matches the measurements, the first cell diameter is larger than designed and the second cell diameter is smaller. The bolded parameters are those which are larger than the design in the scaled version.

dimensions were scaled to roughly match the resonant frequency of the measured π mode, approximating the fabricated electroformed structure. A schematic of the mandrel and measurement locations is shown in Figure 4.24. Table 4.2 summarizes the measured values for the representative mandrel and the values after scaling. The simulated S_{11} of the scaled and unscaled mandrel are shown in Figure 4.25.

In addition to varying the cell diameters (D1 and D3), sweeps were performed on the first cell length (L1), the inner iris diameter (D2), the second cell length (L3), and the length of the coupling circular section (L5). The length dimensions had the most significant deviations from the design across all of the mandrels. Each parameter was varied independently to see the isolated effect. The overall length of the structure was only changed in the L5 case.

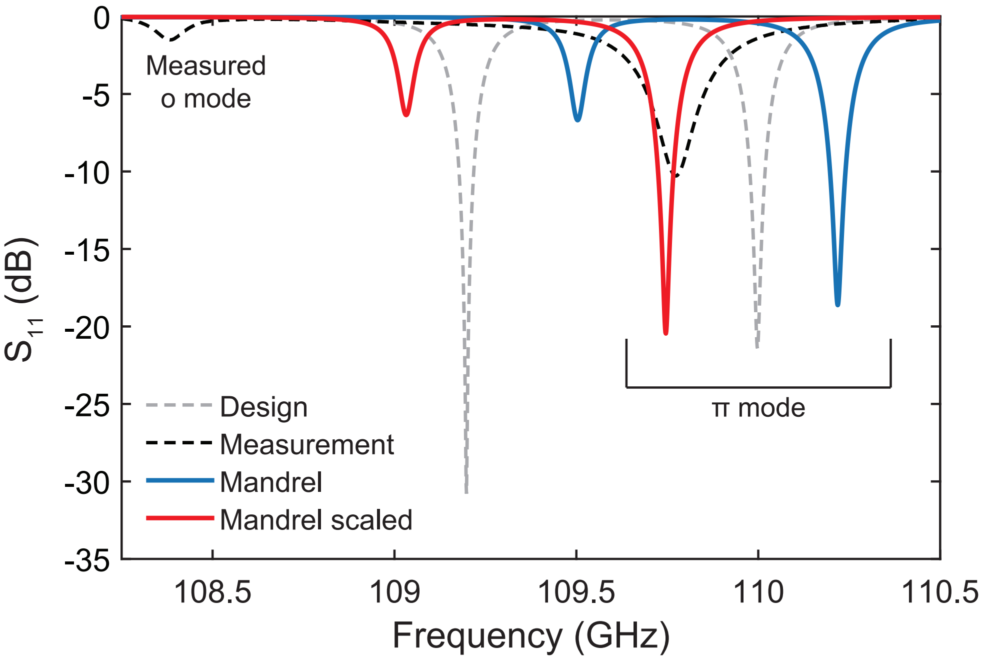

Figure 4.25: Simulated S_{11} of the structure based on the mandrel dimensions before and after scaling. The dashed lines show the design spectrum (gray) and a measurement (black) for reference. It is clear overlaying these four cases that the measured o mode is significantly lower in frequency than either the design case or the simulated mandrel case. Even with the mandrel dimensions scaled to roughly match the π mode frequency, the o mode is significantly higher in frequency and more strongly coupled than in reality.

In the other cases the measured length of the structure was left constant, and so changing one length inherently impacted another. For example, shortening the length of the first cell without changing the length of the second cell corresponds to making the iris between the two thicker. The results are shown in Figure 4.26.

There are two changes which clearly result in a mode balance and spacing similar to the measurements. First, shortening the first cell (L1) and therefore having a thicker inner iris has a significant impact on the o mode without changing the π mode to the same degree. Across the 10 mandrels measured, L1 is consistently small and L2 is consistently large. This dimension alone could be responsible for the measured behavior, especially since the frequency of the π mode is roughly correct with the scaled cell diameters.

The diameters of the two cells (D1 and D3) also have a strong impact when one is changed by a large value. The original design values are D1 = 2.160 mm and D3 = 2.310 mm, but the measured mandrel values were D1 = 2.152 mm and D3 = 2.294 mm. The error in the second cell diameter is twice that for the first cell (16 μm versus 8 μm) for this mandrel, and thus it is expected that the relative mode strength would deviate from the design. When this relative error is increased, either by making D3 smaller for constant D1 or D1 larger for constant D3, the mode spacing increases and the o mode coupling is weakened. Based on the resulting shifts in the π mode, it is more likely that D1 is larger than measured, since D3 being smaller would raise the π mode frequency significantly. The 10 mandrels have substantial variation in the cell diameter errors, both absolute and relative. This difference alone could not be responsible for the shift in every structure, but is likely playing a significant role in many of the structures.

Overall, these simulations indicate that there are a number of imperfections in the fabricated structures that could result in the observed mode spacing and balance. Based on measurements of the mandrels and the simulation results, the size of the first cell in both radius and length is responsible for the majority of the deviation from design.

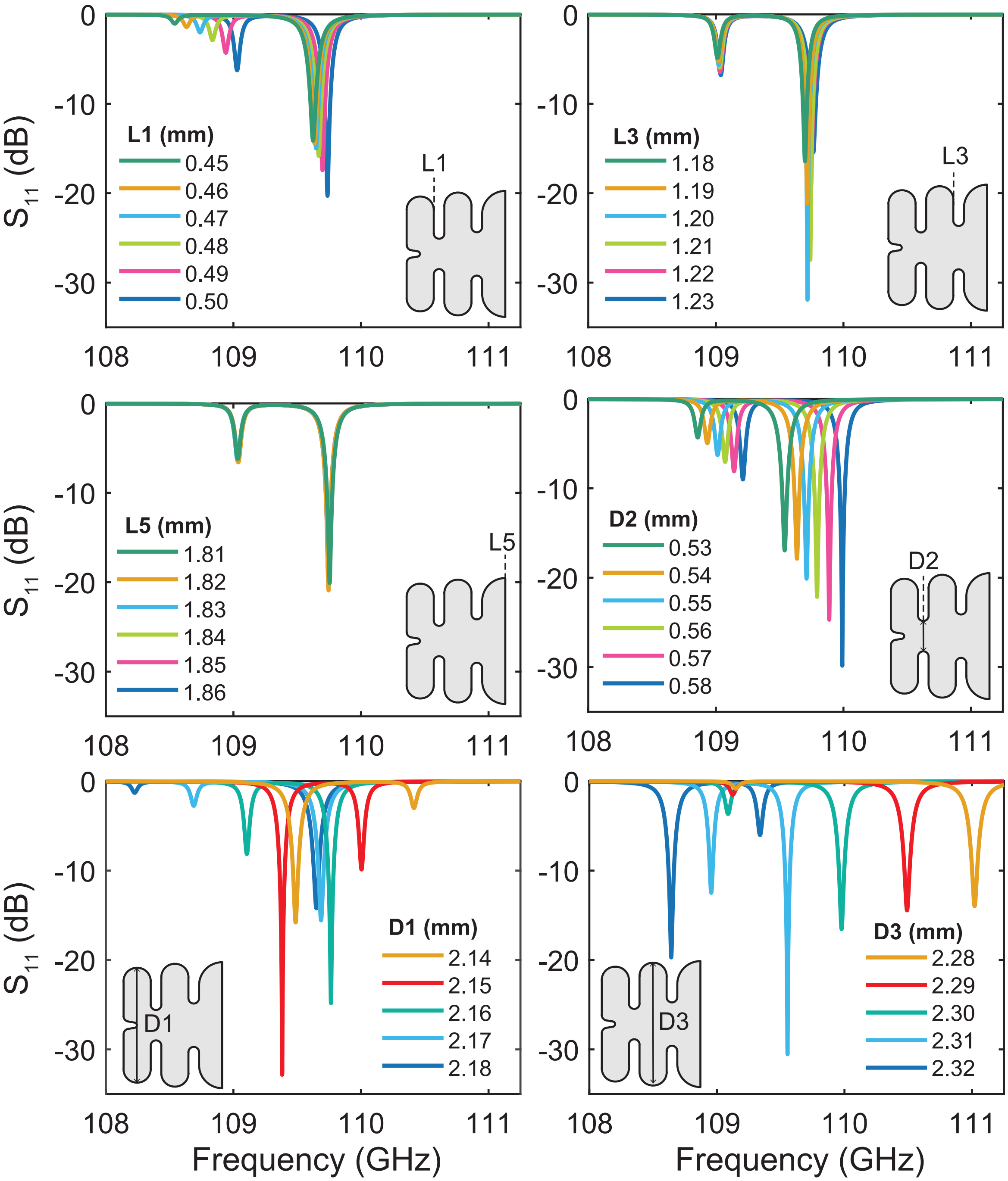

Figure 4.26: Simulated S_{11} sweeping different dimensions on the mandrel while all other values are held constant. See Figure 4.24 for the design values and Table 4.2 for the starting values of the scaled mandrel. The parameter swept in each case is labeled.

Effects on acceleration and emission

The mode balance and spacing is an indicator of the strength of the electric field in the two cells. If the field strength is too strong or too weak in a cell compared to the design, it could hinder the beam acceleration. The field on the tip is also affected, and therefore the field emitted bunch charge would also change.

To understand the potential performance of the structures as-fabricated, values were chosen for the cell diameters and the length of cell 1 to match the measured mode spectrum. The chosen values were D1 = 2.170 mm, D3 = 2.303 mm, and L1 = 0.475 mm. The other dimensions were based on the scaled mandrel measurements, as listed in Table 4.2. This gave a π mode frequency of $f = 109.763$ GHz and an o mode frequency of $f = 108.432$ GHz. These values fall within the middle of the range of the measured values with roughly the correct mode spacing and balance.

The resulting fields were used to calculate the on-axis particle acceleration and electron emission based on the Fowler-Nordheim equation. Sections 3.3 and 3.5.2 have detailed discussions of these models. The resulting acceleration is shown in Figure 4.27.

The maximum field on the tip was greatly reduced for 500 kW of input power. At the center of the tip, the field is just under 1 GV/m, significantly lower than the design value of 3.9 GV/m. There is also a phase mismatch between the maximum energy gain and the maximum field. Both of these factors would limit the emitted electron bunch charge and the fraction of the bunch that is successfully accelerated. Based on these fields, the emitted bunch charge would be effectively zero without considering additional surface field enhancement. However, there will be some surface field enhancement β in a real structure. Relatively modest values of $\beta = 2.5$–3.5 would produce bunch charges on the order of 1 fC per RF cycle, and $\beta = 4$ would reproduce the design bunch charge. The tip profile shown in Figure 4.23 indicates there will be local enhancement both from sharp features on the tip and from the roughness of the surface overall. While the acceleration performance of this structure is not ideal, it should still produce and accelerate measurable electron bunches with just 500 kW of input power.

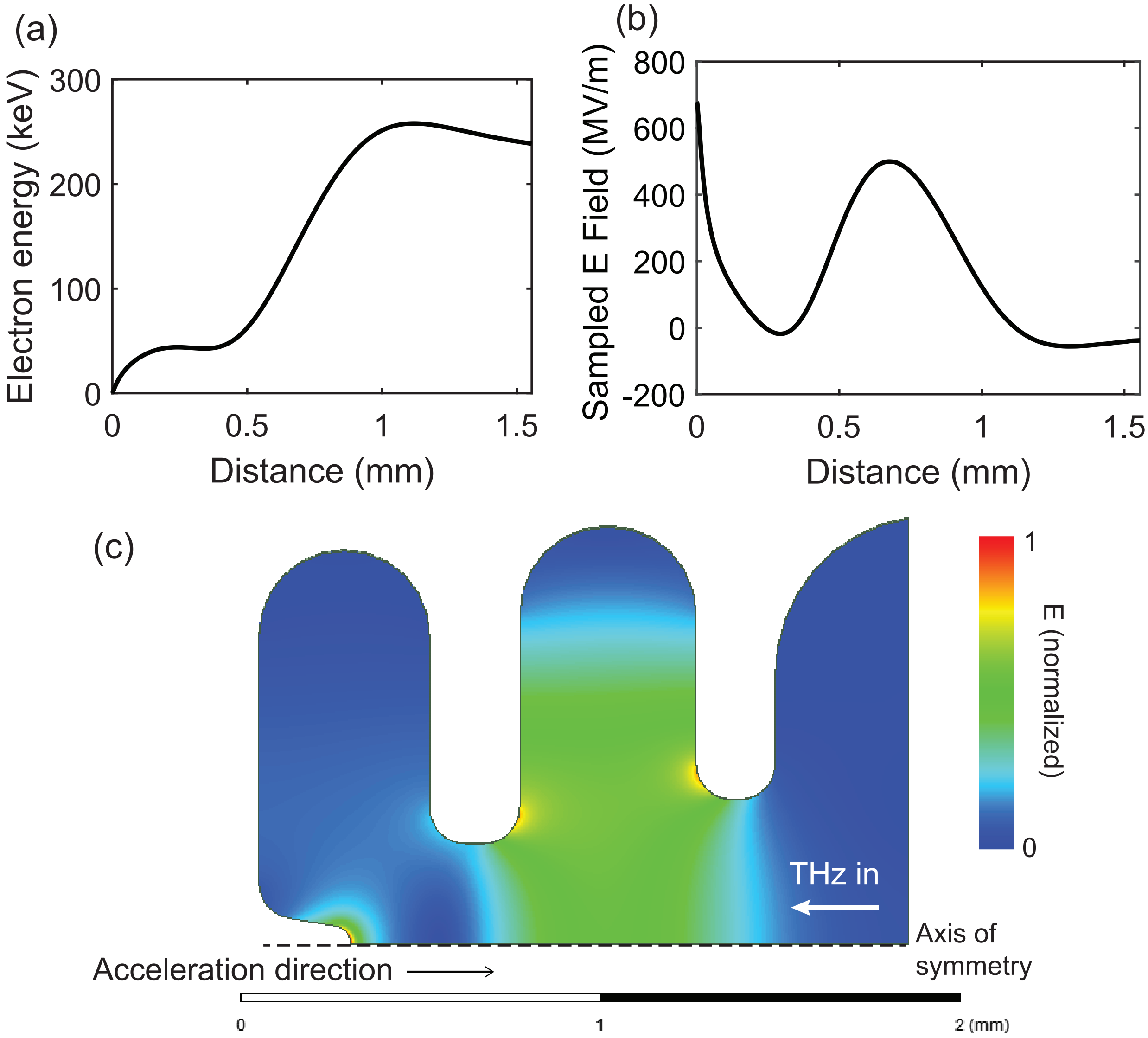

Figure 4.27: Modeled field and single particle acceleration of the scaled structure. (a) The maximum on-axis single particle acceleration with 500 kW of input power. (b) The electric field experienced by the particle. (c) The magnitude of the complex electric field of the π mode. The field is clearly concentrated in the second cell, which provides the bulk of the acceleration. This is in contrast to the design (Figure 3.9) which has roughly equal energy gain in each cell.

4.5.2 Plating

When the frequency of a cavity is low, one possibility to raise the frequency is to reduce the internal volume as discussed in Section 2.2.2. The internal volume can be reduced by localized perturbations in the cell shape, but this is difficult to achieve on this length scale. Another option is to shrink all dimensions in the structure. This is what occurs due to thermal contraction when a cavity is cooled. As explained in the introduction to this section, the frequency shift required is too large for this method.

Plating a thin layer of copper on the inside of the structure could achieve the same effect. HFSS simulations were performed to determine the frequency shift due to a uniform coating on all internal dimensions. These simulations were performed with the mandrel-based model of the structure described in the previous section. The results are shown in Figure 4.28 for coating thicknesses from 1–7 μm. The result is a frequency shift of about 82 MHz/μm.

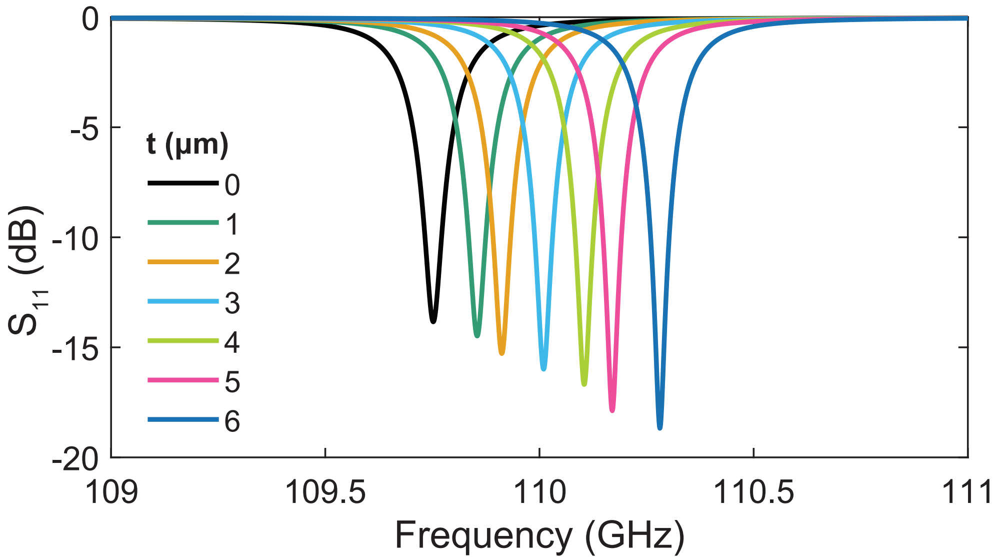

Figure 4.28: Simulated frequency of the π mode versus a uniform coating thickness t. The $t = 0$ μm case is the same as the structure described in section 4.5.1. The shift is on average 82 MHz/μm.

These thicknesses are within the feasible range for electroless copper plating. Thicknesses below 5 μm are common, though up to 10 μm is possible. Thicknesses on the order of 2–5 μm would be sufficient to bring several of the higher frequency structures into the usable range. Four candidate structures were identified for plating: structures 2, 3, 6, and 8. For structure 6, a coating of 3.5 μm was chosen, which would bring the structure within the range of temperature tuning for high power operation. Structure 8 would require 4 μm to reach the same range. These two structures were sent to one company for an initial plating test.

First round of plating

Cold test measurements of the structures 6 and 8 before and after plating are shown in Figure 4.29.

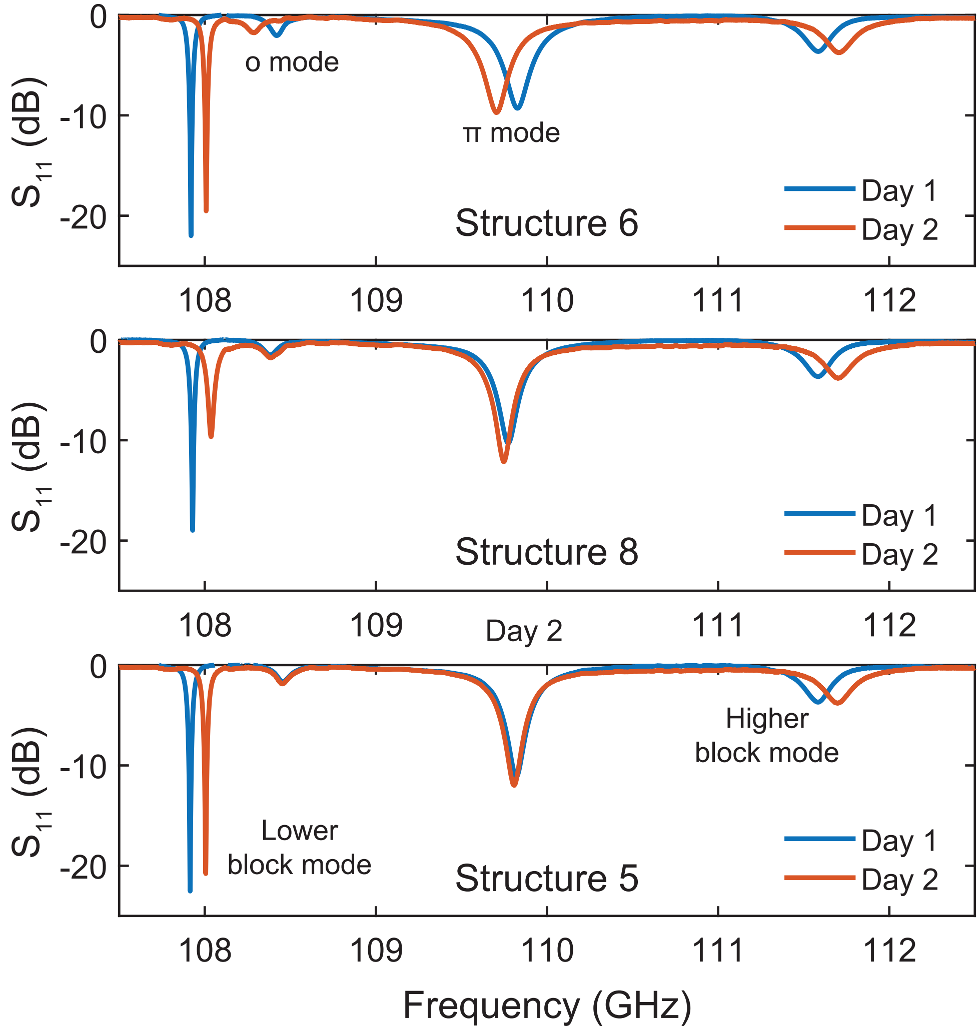

Figure 4.29: Measured S_{11} before (Day 1) and after (Day 2) plating. Structures 6 and 8 were plated. Structure 5 is included as a control. Both the o mode and π mode frequencies decreased after plating for structure 6. The π mode frequency in structure 8 also dropped, but by a smaller amount. The block modes shift frequencies as a result of the block tightening and is not indicative of any change in the structures. This is visible in the structure 5 case, where nothing was changed about the cells. The block mode frequencies have shifted, but the cavity modes are the same on both days. For more details on the block modes, see Sections 4.3.2 and 4.4.2.

Instead of increasing, the frequencies of both modes decreased. Inspecting the structures under the microscope showed significant changes in the surface finish. The copper appeared to be heavily oxidized. The structures were cleaned to remove the oxidation, reported in Section 4.5.3. Images of the structures before and after plating are shown in Figure 4.30.

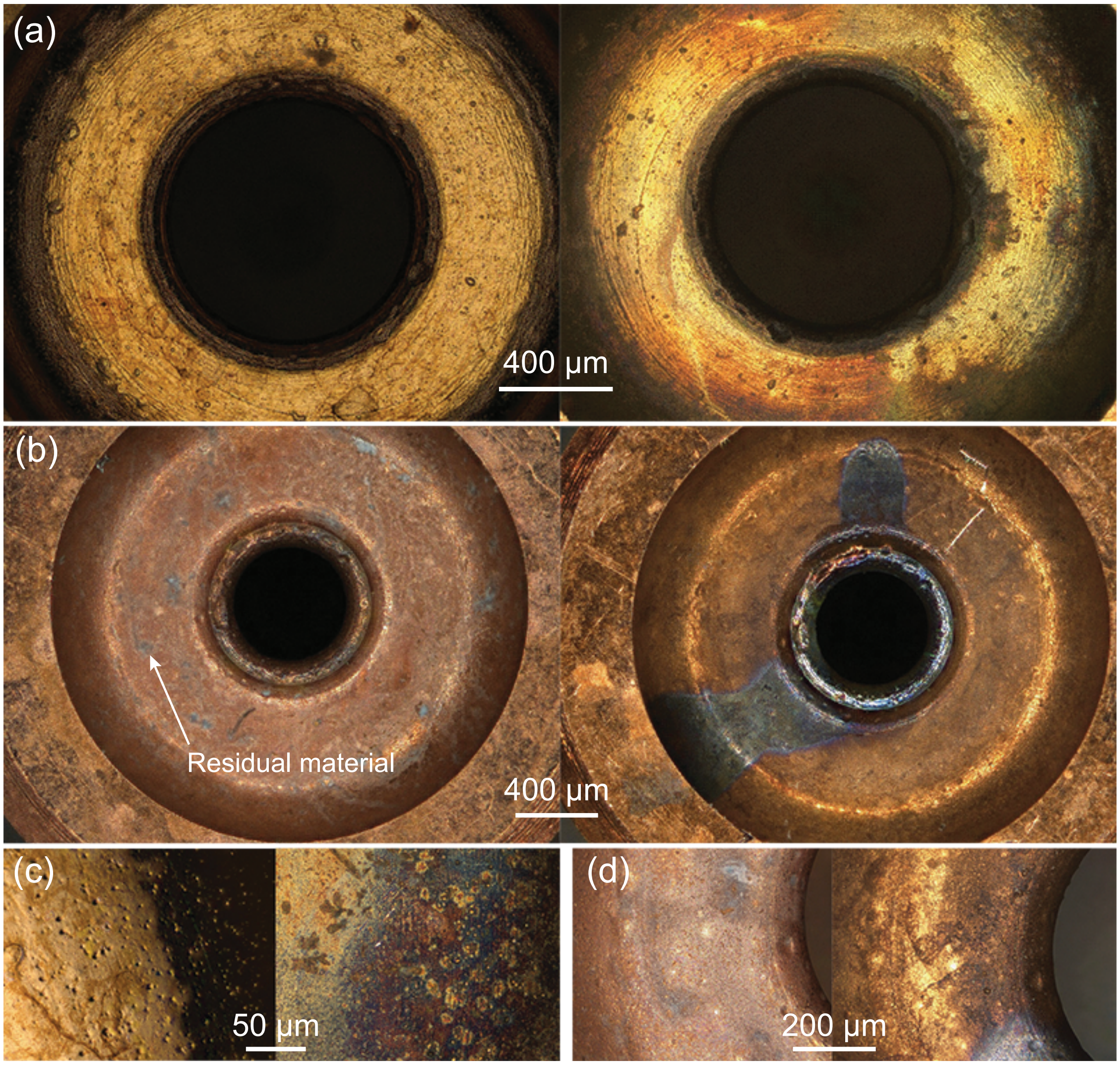

Figure 4.30: Images before (left) and after (right) plating. The images of structure 8 are in the same orientation before and after, but the images of structure 6 are not. (a) Coupling iris of structure 6. Significant discoloration is visible. (b) Structure 8. Both irises are visible. There is clear discoloration on both the coupling and inner irises. Structure 8 appeared to have some residual material left behind from the mandrel before plating. (c) Zoomed view of the coupling iris surface on structure 6. In addition to the discoloration, there appear to be changes in the surface roughness. (d) Coupling iris edge on structure 8.

Second round of plating

After the failure of the first round of plating, a second company was identified to perform another plating test. Structures 2 and 3 were initially among the lowest in π mode frequency. Instead of attempting to bring these structures fully into useable range, the same thicknesses from the first round were repeated. The plating thickness was set as 3.5 μm for structure 2 and 4 μm for structure 3.

In this case, the structures were clearly plated but the plated layer peeled. This caused enough of a perturbation in structure 3 to eliminate the cavity resonances. In structure 2, the frequency did not significantly change. Figure 4.31 shows these results.

Images of the structures before and after plating are shown in Figure 4.32. It is clear that the plating is peeling in both structures. The peeling is much worse in structure 3, which is expected given the cold test results. The peeling is likely a result of a lack of proper surface treatment before plating. Any residual surface contamination could have affected the plating process. There are also bubbles and ridges in the plating visible. Based on the locations of significant holes in the plating on structure 3, it is possible that existing pits on the structure were the cause of some of the peeling.

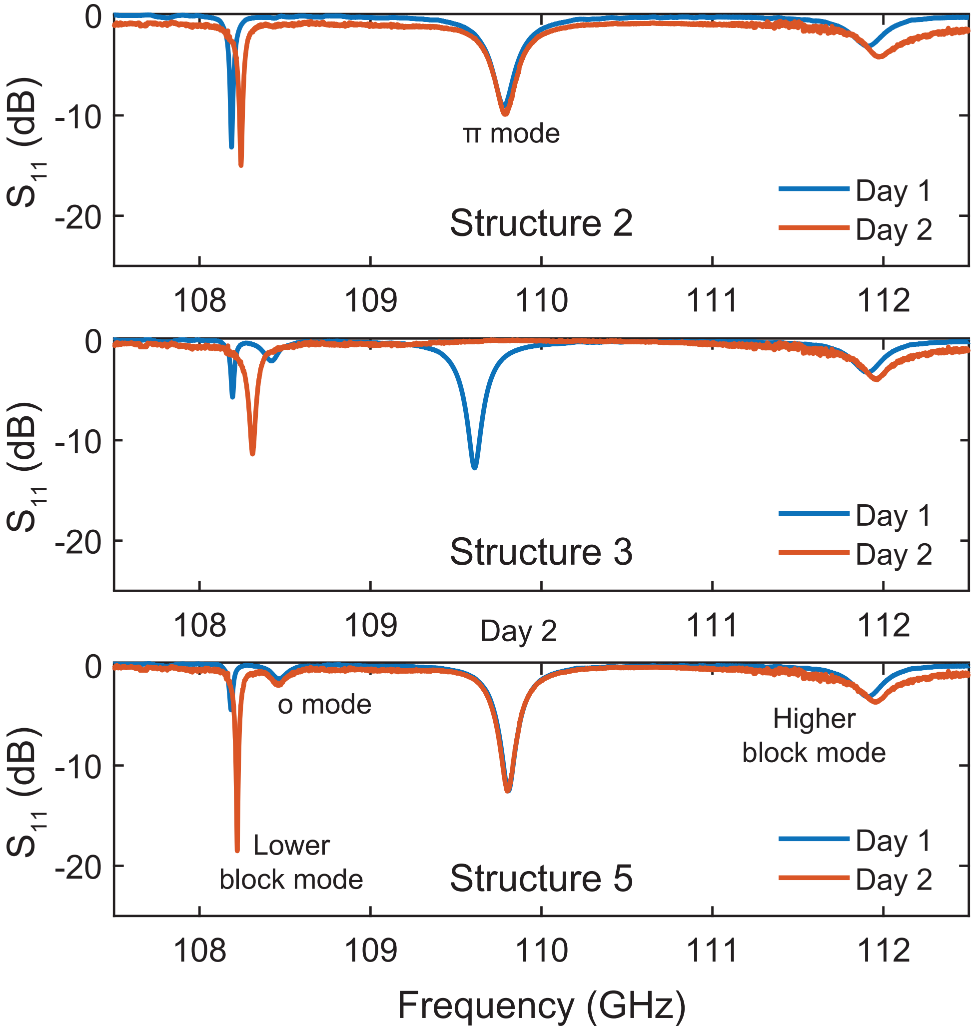

Figure 4.31: Measured S_{11} before (Day 1) and after (Day 2) plating. The measurements were taken on different days than those in Figure 4.29. Structure 2 does not show any significant change in the π mode. The o mode is not visible because it is at roughly the same frequency as the block mode in this case. Both modes were previously visible in structure 3 but are not after plating. Structure 5 is included as a control for reference and was not plated.

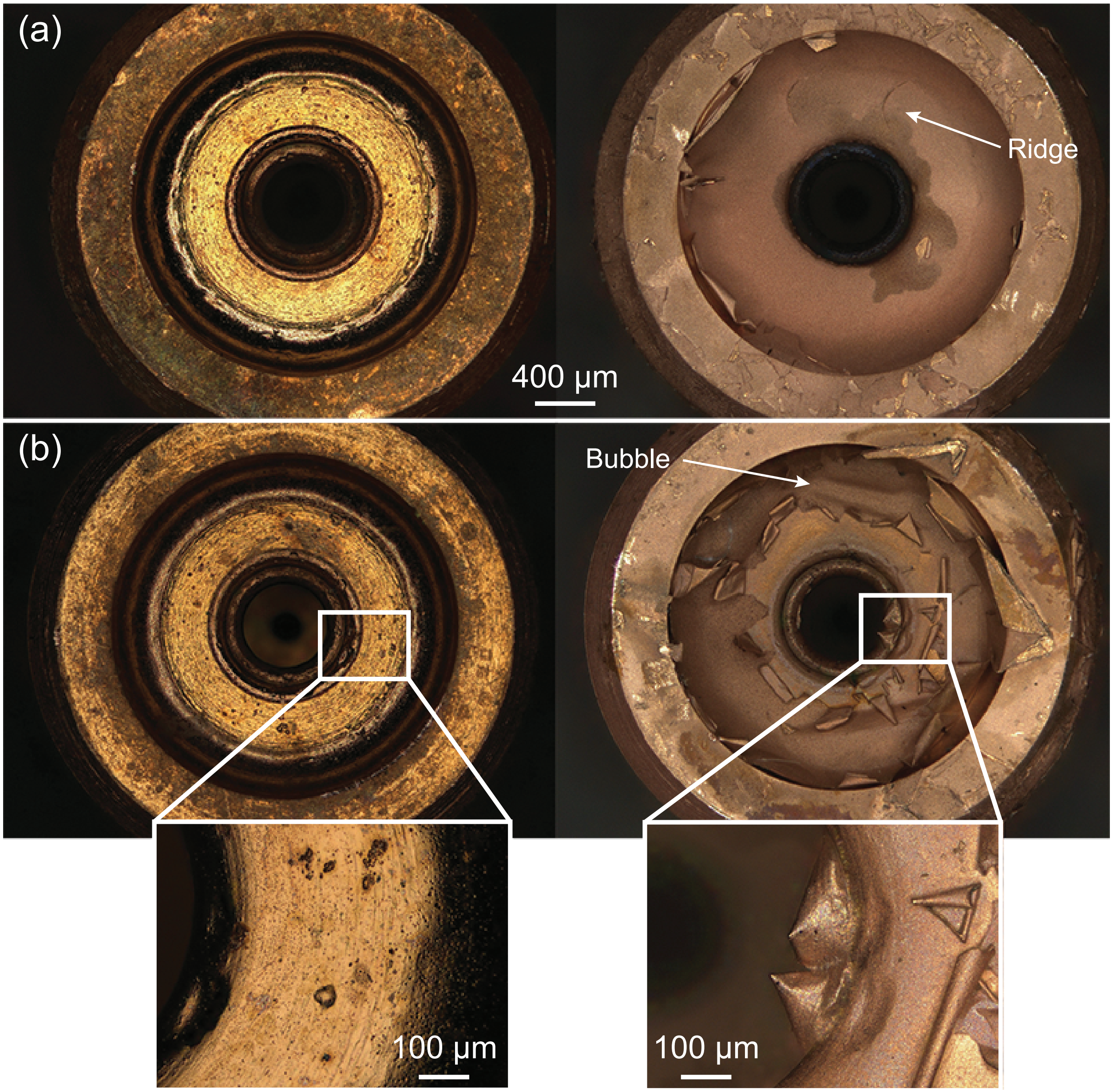

Figure 4.32: Images of the structures before (left) and after (right) plating. All images show the structures in the same orientation before and after. Row (a) shows structure 2, which has a small amount of peeling with no significant change in the frequency. (b) Structure 3, which has a substantial amount of peeling. The insets show a zoomed view of pits on the coupling iris which may have influenced the peeling.

Summary

None of the plating tests resulted in a good quality surface inside the structure. While the resonances were preserved in most of the structures, the desired frequency tuning was not observed. Since the plating itself was not successful, it cannot be concluded whether the frequency tuning shift after successful plating would match the simulations. The electroless copper plating process should theoretically provide better plating quality than observed, so there is the potential to conduct further tests. Further tests are needed to explore what surface preparation is necessary to achieve better plating. Since only 8 structures were fabricated, no further plating tests were performed as part of this thesis.

4.5.3 Etching

Images of some structures—particularly structure 8—showed residual material which was likely left behind from the mandrel. The plated structures 6 and 8 also appeared to be heavily oxidized. Contaminants on the surfaces could reduce the mode frequencies depending on their locations and material properties. Based on the mode spacing simulations described in 4.5.1, it is also possible that large amounts of residual material in the cells could potentially cause the cells to appear shorter and influence the resonances. If this were the case, removing the residual material could increase the resonant frequencies or improve the mode balance.

To test this, three structures were chosen for chemical etching. The HCl etch removes oxidation and aluminum, but should not remove any copper. Structures 6 and 8 were etched along with structure 1. Structure 1 had not received any plating or additional treatment and had the lowest π mode frequency. The etching increased the frequency of all three structures. The results of these measurements are shown in Figure 4.33.

In structures 6 and 8, the resulting π mode frequency was not only higher than the plated value, but also higher than the pre-plating frequency. Structure 1 also saw a significant increase despite never being plated, indicating that the structures as-fabricated contained some residual material. Residual material could raise or lower the frequencies depending on its properties and location inside the cells. Metals—such as pieces of the aluminum mandrel—in a high E field region could lower the frequency by acting as a volume perturbation. In contrast, an inward volume perturbation by the addition of metal in a high H field region would raise the frequency (see Section 2.2.2). Extra material near the irises or on the tip surface would be in the highest E field regions. Removing residual aluminum in these areas through etching could raise the resonant frequencies overall.

Additionally, the o mode frequency shifted by more than the π mode frequency in all three cases, which reduced the mode spacing. As the simulations described in Section 4.5.1 showed, the mode spacing is most heavily influenced by the first cell and the relative cell radii. The observed change hints at there being more material removed in one of these areas than others. If that material was primarily metal removed from the high E field regions around the tip and inner iris within the first cell, it could explain both the overall frequency shift and the change in the mode spacing.

The etched structures also showed visible changes. The majority of the oxidation was removed in the two plated structures. After etching, the surfaces show more scratches. It is possible that these scratches were under the oxidation, or they could have been caused by material dislodged during the etching process. These surface features did not reduce the coupling and are not likely to inhibit operation of the gun. Selected images before and after etching are shown in Figure 4.34. An interesting case is the copper tip in structure 1. While this structure was never plated, there is clearly a change in the profile of the tip and material was removed. The tip surface is the highest E field region, further indicating that residual material was at least partially responsible for the low resonant frequencies.

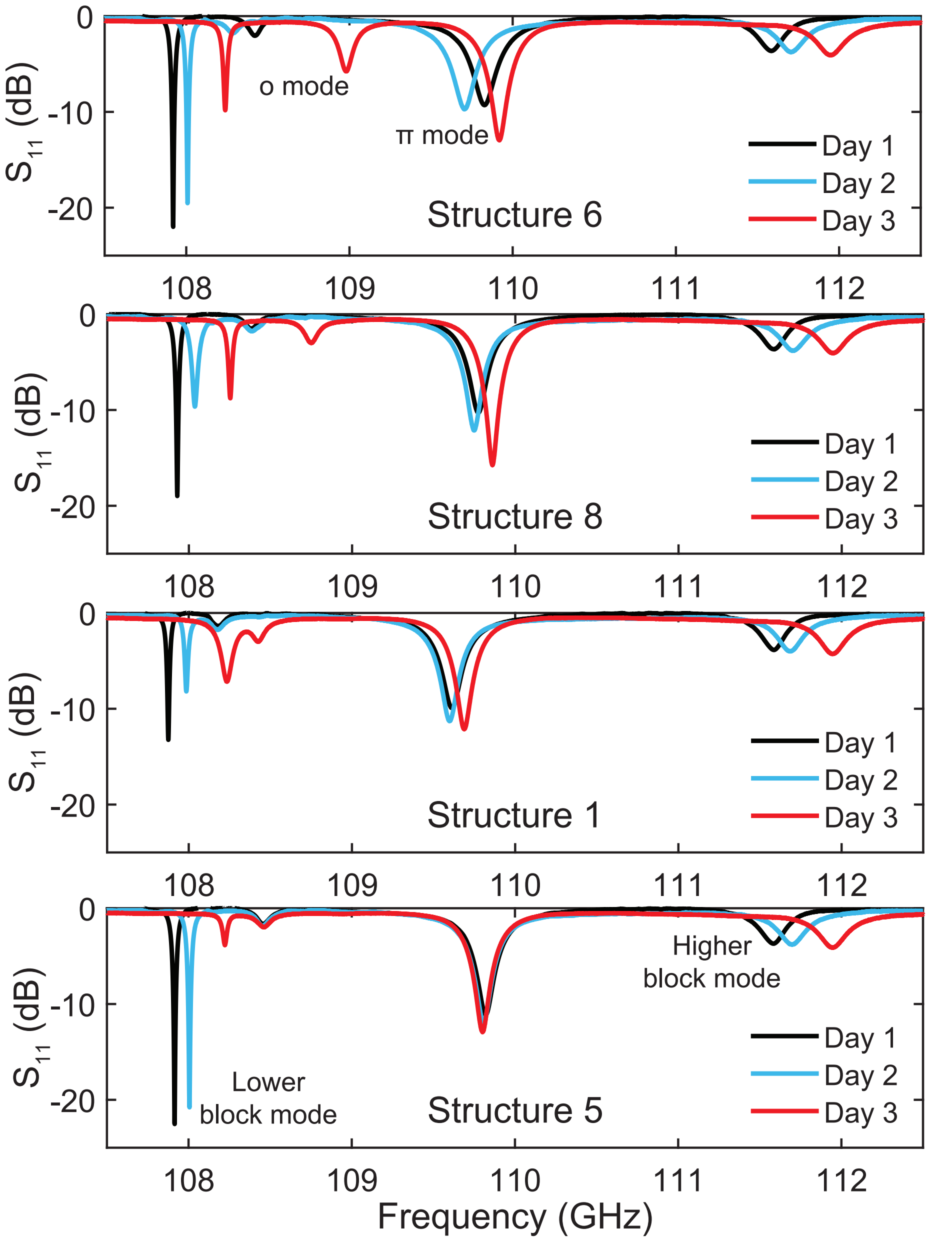

Figure 4.33: Measured S_{11} before and after cleaning. Day 1 is the original frequency. Day 2 is after structures 6 and 8 were plated. The measurement after etching (Day 3) shows an increased frequency for all three structures. In all cases, the o mode shifted more than the π mode. This is most visible in structure 6. Structure 5 was not plated or etched and is included for reference. The shifts in the block modes are due to the mode converter block clamping.

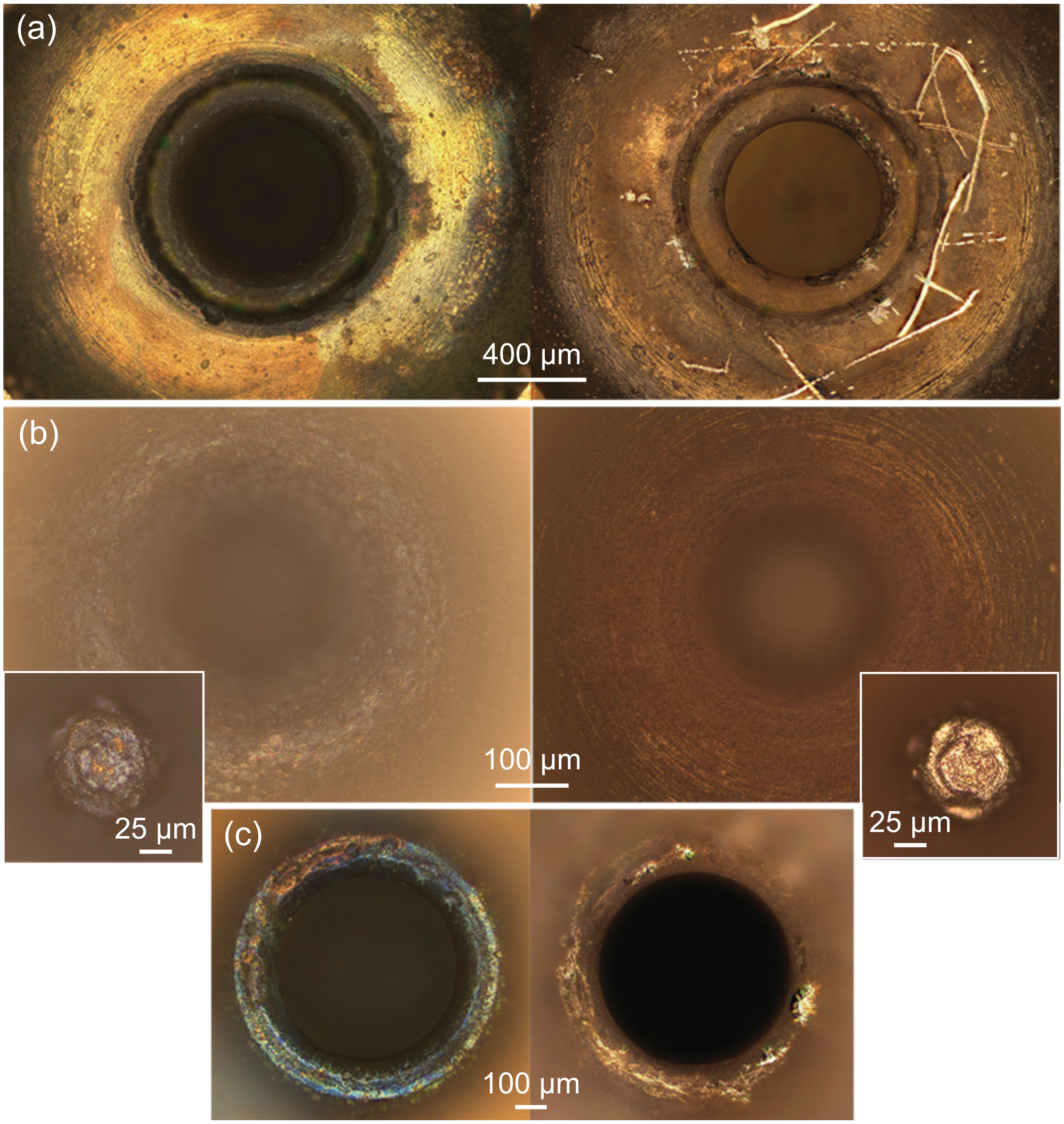

Figure 4.34: Images of the structures before (left) and after (right) etching. All images show the structures in the same orientation before and after. (a) The irises and coupling cell surface of structure 6. (b) The area around the base of the tip (the wall of the first cell) in structure 1. The surface changed significantly after etching, with some material removed. The insets show the top of the tips. After etching, the tip is less rounded and material was removed from the center. (c) The inner iris of structure 8.

4.5.4 Mechanical tuning

The final method used to tune the structures was mechanical deformation. The principle is the same as plating: by reducing the internal volume of the structure, the frequency should increase. Unlike a plating layer, which would be added to all internal features, deformation can be introduced on specific features. This is the hallmark of RF accelerator cavity tuning, where deformations can be made in a specific area of just one cell.

In practice, performing such deformation on W-band cavities is challenging. However, since the gun cells were electroformed as a cylinder rather than two halves of a block, they also are uniquely suited for azimuthal compression. This could potentially reduce the cell and iris diameters without significantly impacting the copper tip. As shown in Figure 4.26, changes in the cell radii on the order of 10 μm can substantially change the frequency and shift the mode balance. This corresponds to a change on the order of 1% in the cell radii.

To test this, several structures were compressed using a 3–4 mm ER collet. Such collets are designed to compress relatively evenly, though this depends on the quality of the collet. Figure 4.35 shows a photo of a structure in the collet. The structures were etched before tuning, which slightly increased mode frequencies as described in the previous section.

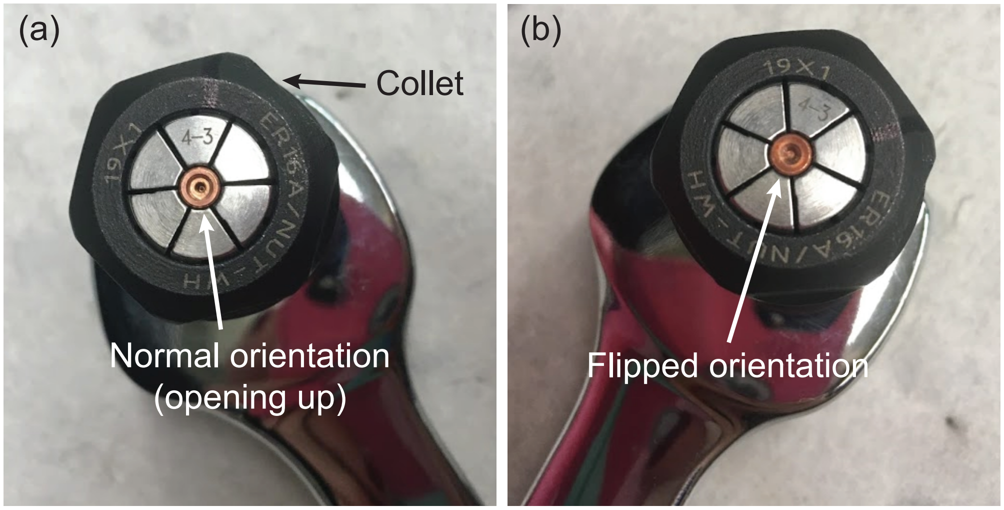

Figure 4.35: Images of a structure in the tuning collet. (a) The ‘normal’ orientation with the circular input waveguide opening pointing up. (b) The ‘flipped’ orientation.

Tuning was performed by making small compressions and measuring the frequency after each step. Markings on the face of the collet were used as reference points when returning to the previous degree of tightening. There is also significant resistance when compressing the structure, which makes it possible to distinguish between tightening the collet and compressing the structure. To ensure even compression, the collet was tightened to the same point for multiple tuning steps in a row. In some cases the repeated steps caused an additional frequency shift, indicating the compression is not entirely uniform.

Structures were tuned in two ways. In the first method, the cells were placed in the collet with the waveguide opening facing up for every step. In the second, the orientation was reversed. Several tuning steps were performed with the waveguide opening up, and then the structure was flipped upside down for several steps. This resulted in somewhat different tuning behavior. Figure 4.36 shows the measured results from one structure (structure 8) tuned using the first method. In this case, the o mode and π mode tuned by similar amounts. Coupling to both modes was eventually reduced and the relative mode balance did not change significantly.

Using the second method, it was possible to tune the o mode and the π mode almost independently. This was utilized to shift the o mode by more than the π mode to restore the design mode spacing. These results are shown in Figure 4.37 for structure 4. Tuning with the structure in the normal (waveguide opening up) orientation had some effect on both modes. However, multiple compressions to the same point continued to tune the o mode while the π mode remained almost constant. When the structure was flipped and compressed to the same point, the π mode jumped in frequency and the o mode frequency did not change significantly. Based on this behavior, the o mode can be tuned using the normal orientation and the π mode can be tuned in the flipped orientation. The resulting mode balance and spacing is much closer to the initial design, which should ensure better field balance, acceleration, and emission and is explored in the next section.

The net result in structure 4 was a shift in the π mode from $f = 109.911$ GHz to $f = 110.081$ GHz. The o mode was shifted from $f = 108.555$ GHz to $f = 109.332$ GHz. Tuning of the two modes separately was clearly demonstrated. The o mode tuning behavior is very similar to the results from changing the length of the first cell in the mode spacing simulations. The total change in the o mode frequency was 777 MHz, roughly 4.5 times the π mode shift (170 MHz). It is possible that while compressing in the azimuthal direction, the length of the first cell increased slightly. Combined with decreasing cell radii, this could explain the difference in the relative shifts.

The structures were imaged after tuning to see the impact on the irises and visible surfaces. No damage such as cracking or warping of any surfaces was observed. The tip size and profile also remained unchanged. The iris radii, the coupling waveguide radius, and the outside diameter of the structure were all measurably decreased. Figure 4.38 shows images of structure 4 before and after tuning which demonstrate this. Using the microscope, these dimensions were measured before and after tuning. The results are summarized in Table 4.3.

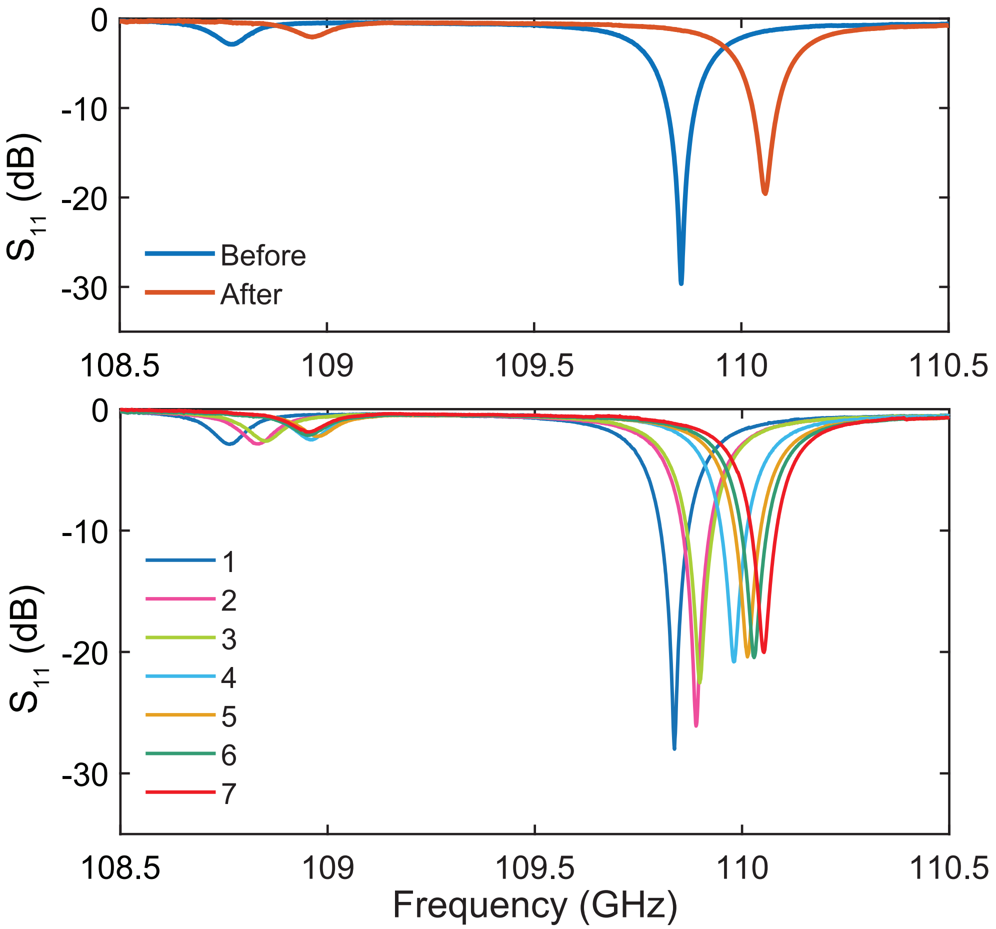

Figure 4.36: Tuning measurements of structure 8. The top plot shows the initial and final measurements and the bottom plot shows interim tuning steps. All tuning steps were performed with the waveguide opening facing up (the ‘normal’ orientation). The result is increased frequency for both modes, but no significant change in the mode spacing or balance. The coupling is also slightly reduced.

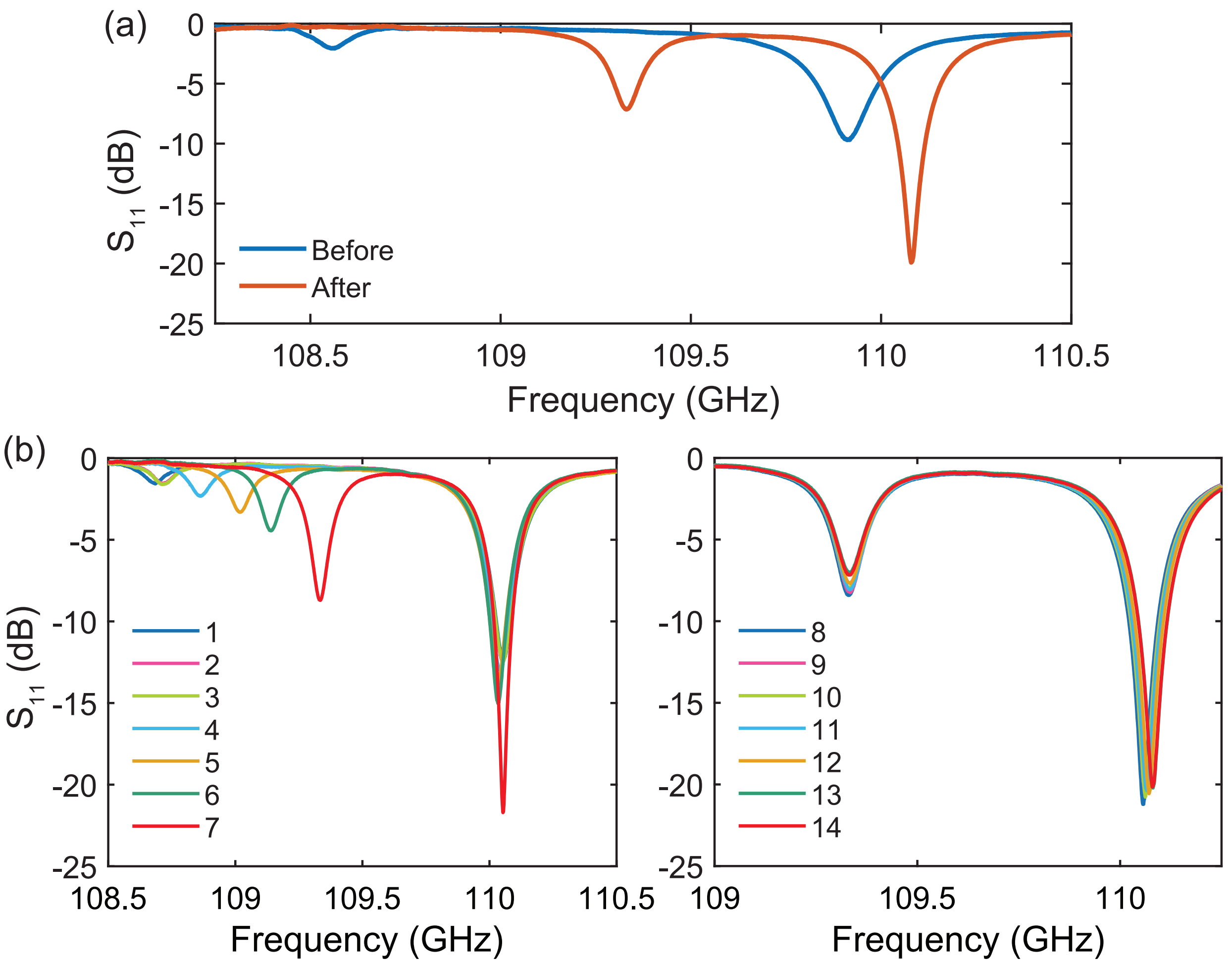

Figure 4.37: Tuning measurements of structure 4. (a) The initial and final measurements. In this case, the o mode was intentionally tuned by a larger amount than the π mode to bring the structure closer to the designed mode balance and spacing. This substantially improved the coupling of both modes. (b) Interim tuning steps of the o mode (left) and the π mode (right). The o mode steps were intentionally larger than the π mode steps since the o mode required a greater shift. All of the measurements in the left plot correspond to the cell being compressed in the 'normal' orientation. The right plot measurements correspond to tuning in the 'flipped' orientation. In the normal case, the π mode frequency is largely unchanged. In the 'flipped' tuning steps, the o mode coupling is reduced but its frequency does not change.

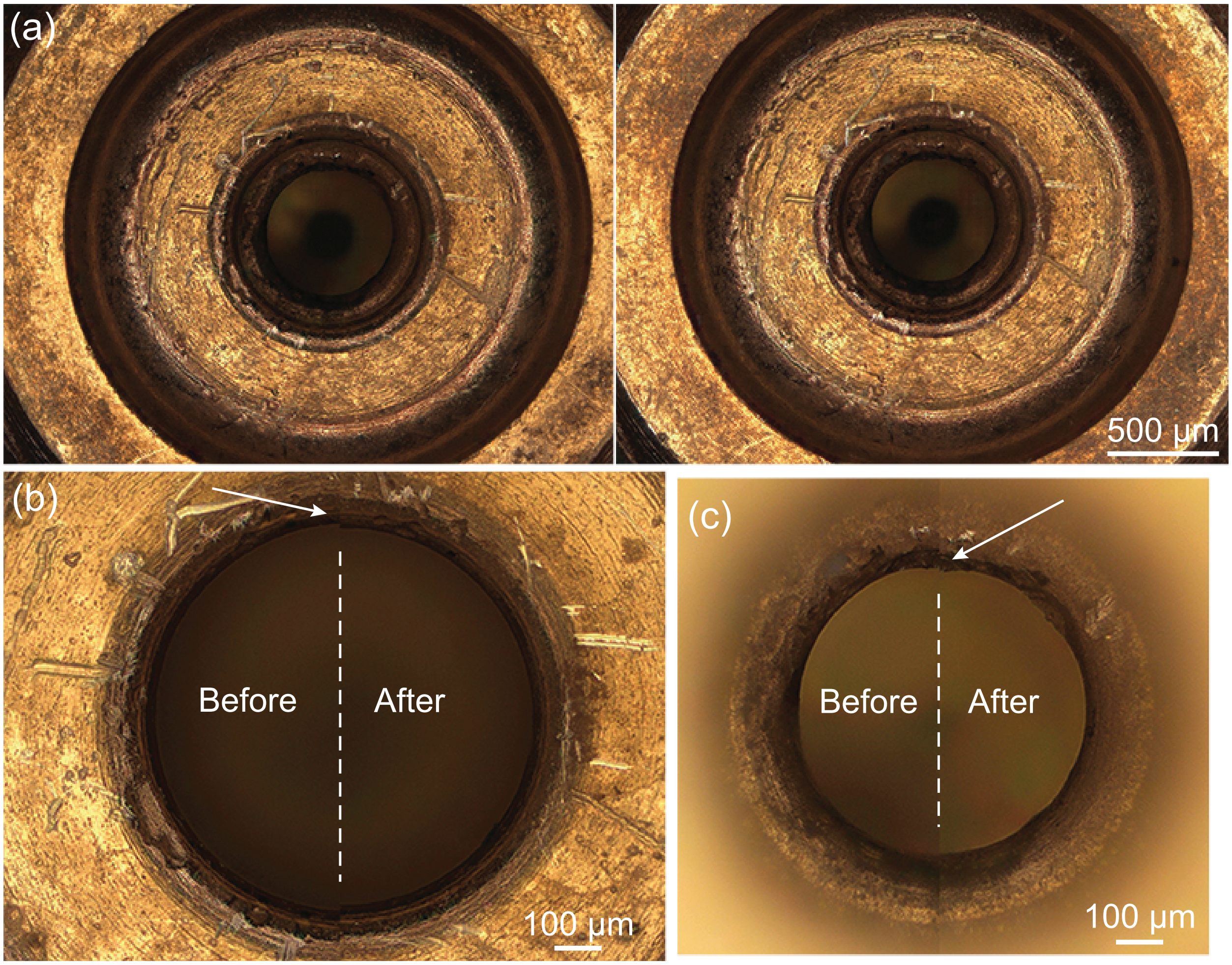

Figure 4.38: Images of structure 4 before and after tuning. In each of the photos, the structure is in the same orientation. (a) Images of the full structure before (left) and after (right) tuning, showing there was no damage to any of the visible surfaces due to tuning. (b) Split image of the coupling iris showing the small decrease in size. The dashed line indicates the boundary between the before and after images. (c) Split image of the inner iris, showing the slight decrease in radius. These images were taken on the same magnification as (b). The decrease in the coupling iris radius is visibly more significant.

Parameter	Before (mm)	After (mm)	Change (μm)
Iris radius	0.280	0.274	6
Coupling iris radius	0.409	0.399	10
Radius of input circular waveguide	1.188	1.173	15
Outer diameter of structure	3.490	3.465	25

Table 4.3: Measured values of structure 4 dimensions before and after tuning. All measurements were performed using the laser confocal microscope. The values are not exact, but the microscope is capable of sub-μm precision.

4.6 Modeling of the tuned structure

In order to predict acceleration performance of the mechanically tuned gun cells, new electromagnetic and particle simulations were performed. As discussed in the previous section, the mechanical tuning of structure 4 was done such that the o mode frequency was increased by more than the π mode frequency. The mode spacing and relative strength is indicative of the field balance in the two cells, which largely determines the acceleration performance of the gun. Section 4.5.1 discussed the performance of simulated cells based on the observed resonances in the fabricated structures. While these cells would still accelerate particles, they do not perform as well as the design and could have low bunch charges. Thus, the aim of tuning structure 4 in this manner was to achieve better field balance and acceleration. This section discusses the results of HFSS and GPT simulations of this structure and how they compare to the design.

4.6.1 Electromagnetic simulations

The simulations in this section are based on a version of the mandrel model discussed in Section 4.5.1 tuned to match the measured resonances of structure 4 after mechanical tuning. The measured values of the structure listed in Table 4.3 were used in combination with the measured mandrel values.

A series of HFSS driven modal simulations were performed sweeping the parameters of the structure found to strongly influence the mode spacing and balance, as described in Section 4.5.1. These dimensions were the cell and inner iris diameters (D1, D2, and D3) and the length of the first cell. The values were set to $D1 = 2.157$ mm, $D2 = 0.549$ mm, $D3 = 2.299$ mm, and $L1 = 0.510$ mm. In addition to roughly matching the mode spacing and balance after tuning, these simulations aimed to match the measured o and π mode frequencies as closely as possible. Figure 4.39 shows the resulting simulated S_{11} compared to the post-tuning measurement.

Figure 4.40 shows the resulting magnitude of the electric field of the π mode. The E field balance does not fully match the original design shown in Figure 3.9, but it is closer than in cases where the mode spacing is much larger such as the field show in Figure 4.27. The most important factor is that the field is much stronger on the tip than in the second cell as in the design. The strong field on the tip is required for emission and ensures significant acceleration within the first cell. The design value was 3.9 GV/m with 500 kW of input power and the tuned results give a maximum field of 2.5 GV/m. This is a substantial improvement over the original mode spacing, which gave less than 1 GV/m. Particle simulations were performed in GPT based on these fields to explore the acceleration performance of the full 3D beam.

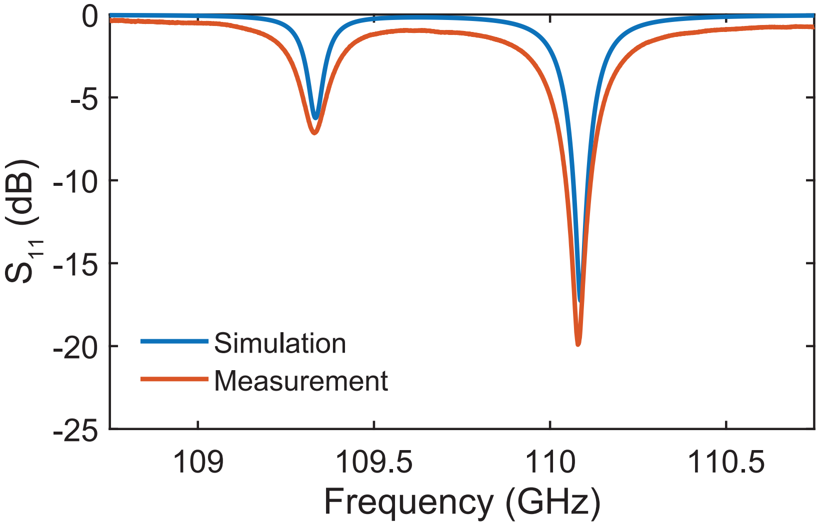

Figure 4.39: Simulated S_{11} of the tuned structure and the measured S_{11} post-tuning. The simulated structure was intentionally tuned to match the measured resonances.

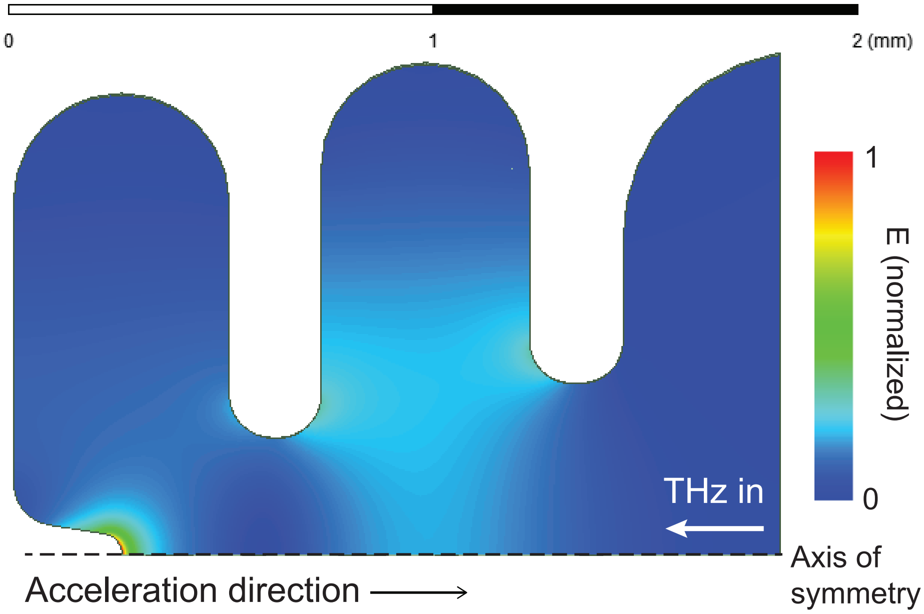

Figure 4.40: Electric field of the π mode in the tuned copper tip structure. The simulation assumes cylindrical symmetry around the dashed line and the electric field is shown in normalized units.

4.6.2 Particle simulations

As in Section 3.5.2, the electron emission was modeled using the Fowler-Nordheim equation with the simulated electric field on the tip surface. A series of 10 points along the tip radius was used to calculate a radial probability distribution used to initialize the beam in GPT. The emitted charge calculation depends on the HFSS value of the field, the emitting area, and additional field enhancement from the surface. The calculations in Section 3.5.2 assumed no additional field enhancement beyond the HFSS-calculated values, meaning the field enhancement factor β was set to 1. In reality, there will be additional local field enhancement due to sharp features and general surface roughness. It is not possible to know this β value exactly, and the value will change as the structure processes to high power. However, it is clear from images and the height profile of the tip that the surface is not smooth and therefore will have $\beta > 1$.

The bunch charge was calculated for a range of possible β values from 1–2 assuming 500 kW of input THz power. In the $\beta = 1$ case, the bunch charge was calculated to be roughly 1.5 aC. This bunch charge would still be detectable even though it is below the design value. For $\beta = 2$, the calculated bunch charge was 5.9 pC. The range of $\beta = 1$–2 is relatively modest, so even with a small amount of field enhancement the tuned structure should achieve sufficient bunch charge. A $\beta = 1.5$ roughly reproduces the design bunch charge at 31 fC. The current and radial probability profiles for $\beta = 1$ and $\beta = 2$ are shown in Figure 4.41. With field enhancement, there is more emission from the edges of the tip, but still no contribution from the outermost points.

GPT simulations were performed using the $\beta = 1$ case for the beam distribution and bunch charge. The goal of the GPT simulations was to determine the final energy and energy spread, which is largely independent of the bunch charge. The influence of larger β is primarily on the size of the beam with more of the tip emitting; space charge forces could also influence the beam and cause spreading with increased bunch charge.

The resulting energy distribution is shown in Figure 4.42. The beam is well-accelerated, but the peak and maximum energies are lower than the design value. In the design case, the maximum energy is also the peak energy at $\gamma = 1.717$ or 366 keV. The tuned structure results give a maximum energy of $\gamma = 1.693$ or 354 keV. The majority of the bunch is at a slightly lower energy with the center of the peak at $\gamma = 1.667$ or 341 keV. This is a substantial improvement over the prediction based on the resonances as-fabricated, shown in Figure 4.27.

Overall, these results verify that tuning the o mode by a larger shift than the π mode should result in better electron gun performance based on the improved field balance. It is not possible to directly measure the field balance in structures of this size, but the mode spacing and relative strength are strong indicators. Other gun structures that were not tuned in this manner and retain the large mode spacing can be tested and compared with structure 4 to verify the difference in performance.

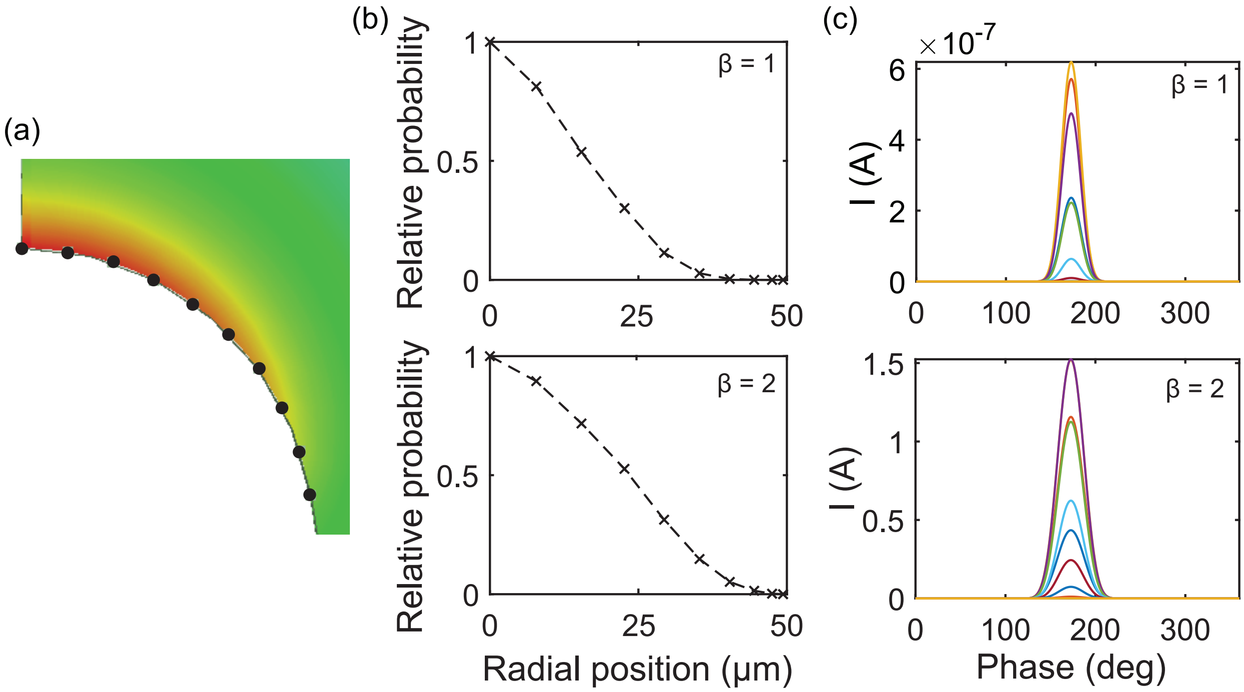

Figure 4.41: (a) HFSS electric field on the tip showing the points which were used to discretize the emission area. (b) The probability of emission at each of the points shown in (a) normalized to the maximum, which occurs at the center. The top plot is for $\beta = 1$ and the bottom is for $\beta = 2$. (c) The emitted current from the areas represented by the points in (a) over one RF cycle. For $\beta = 1$ (top) the current is much lower than for $\beta = 2$ (bottom). For a detailed explanation of how the current was calculated, see Section 3.5.2.

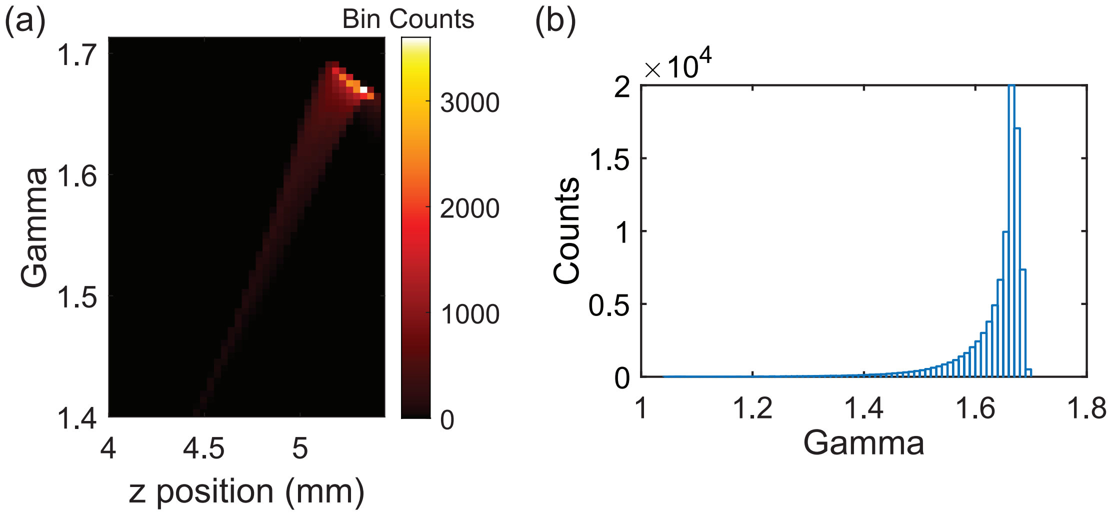

Figure 4.42: (a) Longitudinal phase space after acceleration and a drift. The peak occurs slightly lower in energy than the maximum, but the beam is still well-accelerated. (b) Histogram of the electron energy distribution. The energy bins are $\gamma = 0.01$ or roughly 5 keV. Most of the beam does not reach the maximum energy, which is about 10 keV lower than the design value. Instead, the peak is $\gamma = 1.66$–1.67, about 25 keV lower than the design peak/maximum.

Chapter 5

Full gun assembly and high power setup

5.1 Introduction

This chapter details the experimental setup for future high power measurements. The goal of the high power assembly is to characterize the output electron beam from the gun. In order to measure the beam properties, the setup is essentially a tabletop accelerator beamline. Magnets were designed to control the focusing and steering of the output beam. Three detectors are included to measure the on-axis beam profile, the energy spread of the beam, and the current. The setup is built to be aligned with the output beam of a 110 GHz gyrotron. Details of the gyrotron transmission line are also discussed in this chapter.

The entire setup is designed to use 500 kW of input power from the gyrotron, but can be adapted for higher or lower input powers. The expected energy of the electrons is 350–370 keV for 500 kW. This energy range is a challenging regime because the non-relativistic beam can be substantially impacted by small magnetic fields. Rather than using a magnetic quadrupole doublet or triplet for focusing, this setup uses a solenoid focusing magnet. Energies on the order of 300 keV are typical in electron microscopes which use focusing solenoids. To provide the best beam profile for measuring the energy spread, the solenoid is used to collimate the beam at the output of the beam tunnel rather than focus it to a small spot.

A dipole placed downstream is used to bend the beam as part of an energy spectrometer. With RF cycles below 10 ps, timing resolution would be difficult to achieve. Instead, energy spread characterization is based on the dipole-induced spatial distribution of the beam.To provide sensitivity to single electrons, the setup uses microchannel plate (MCP) detectors which multiply detected electrons to enhance the signal. The dipole can also steer the beam into a Faraday cup to measure the current. A model and photo of the full experimental assembly are shown in Figure 5.1. Each of the elements shown are discussed in the following sections.

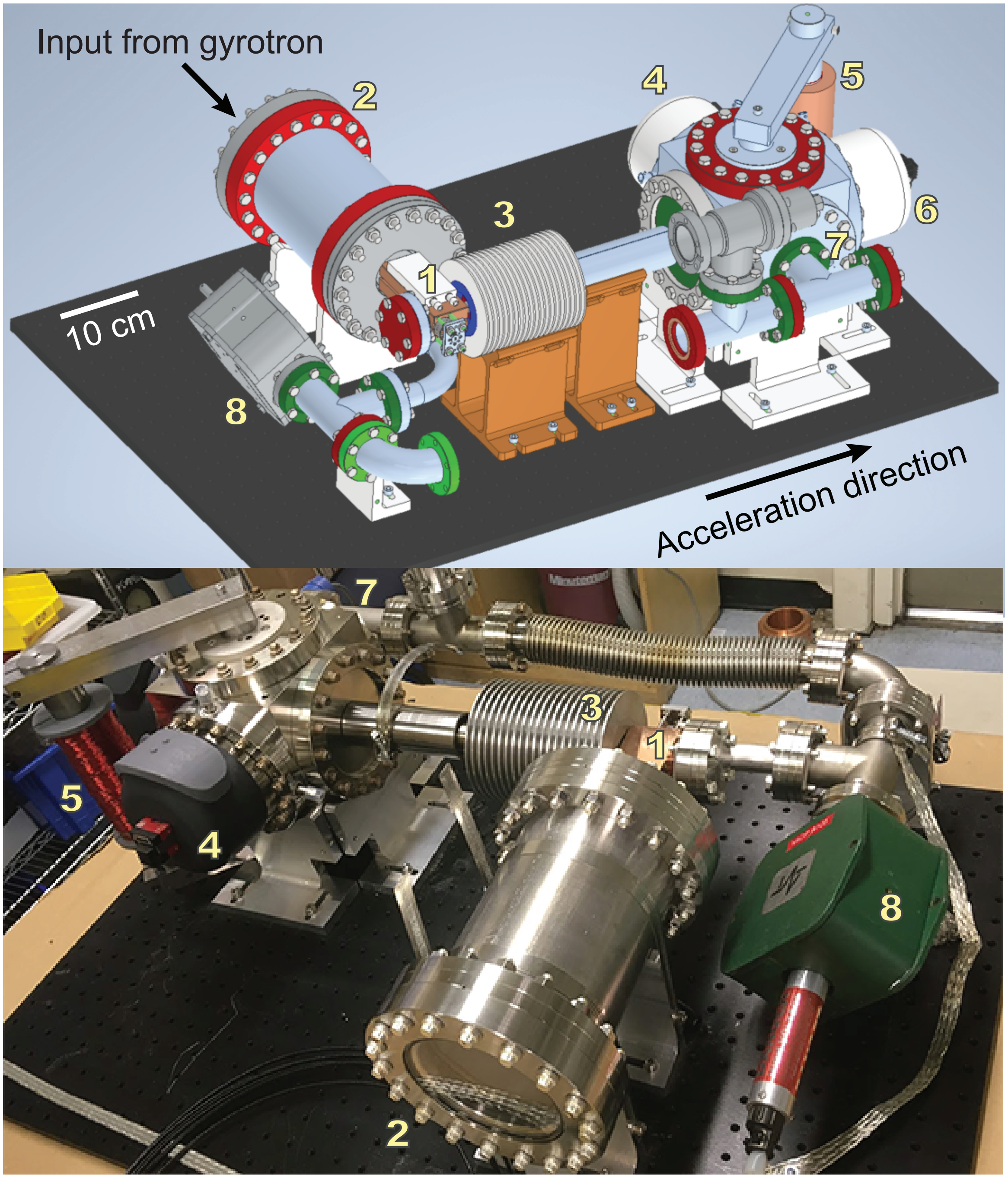

Figure 5.1: Overview of the high power experimental setup. The numbered components are: (1) gun assembly, (2) high power input window, (3) solenoid, (4) energy spectrometer microchannel plate detector, (5) bending dipole, (6) on-axis microchannel plate detector, (7) Faraday cup, and (8) ion pump. The acceleration and THz input directions are shown.

5.2 Gyrotron source

The gun cells and characterization setup were designed to be used with an existing gyrotron oscillator. The gyrotron is located in the Plasma Science and Fusion Center Waves & Beams lab at MIT and has been used to perform high power breakdown measurements on other 110 GHz cavities [46]. The gyrotron consists of a thermionic electron gun, a superconducting magnet, and a resonant interaction region. The electron gun produces an annular beam with both longitudinal and transverse components to the momentum. As the electrons travel along the magnet bore, they gyrate at a characteristic frequency. This frequency can be matched to an eigenmode of the interaction circuit which allows for stimulated emission of electromagnetic waves. Bunching and instabilities in the beam lead to power being transferred to the electromagnetic waves. The resulting high power waves are extracted while the electron beam is deposited on a collector.

The gyrotron is capable of outputting up to 1.5 MW of power at 110.081 GHz and can be tuned over the range of roughly 110.08–110.1 GHz. As discussed in Section 3.4, the gyrotron operates in the $\mathrm{TE}_{22,6,1}$ mode [73, 74]. Power is coupled out and transported in the HE_{11} mode of a corrugated waveguide [75]. This mode couples to a Gaussian beam in free-space, allowing for quasi-optical transmission. An attenuator is used in the transmission line to control the forward power.

Gyrotrons have much longer output pulses than what is needed to fill a THz accelerator structure. The fill time is on the order of a few nanoseconds for 110 GHz structures, but the output gyrotron pulse is 3 μs. Powering the structure for too long would lead to pulsed heating and increase the chance of breakdowns and material damage. To shorten the gyrotron pulse, the setup uses a laser-controlled semiconductor switch. Multiple switch materials have been tested [77] and a Si wafer has been used in experimental measurements of 110 GHz structures [46].

The wafer is typically transparent to the 110 GHz beam. When the wafer is illuminated by a neodymium-doped yttrium aluminum garnet (Nd:YAG) laser, the charge carrier density increases which causes the wafer to become reflective. The wafer remains reflective for a short period of time until the charge carrier density decays. When the wafer is reflective, it serves as a mirror to transmit the 110 GHz beam forward. Otherwise, the beam passes through to a beam dump. A 6 ns FWHM laser pulse on the Si wafer results in a 9 ns 110 GHz pulse with 78% of the input power reflected forward to the structure [77]. Different semiconductor materials can be used to produce different pulse lengths, and multiple wafers can be used in series to reach pulses as short as 3 ns. Photographs of the transmission line and switch are shown in Figure 5.2.

Losses in the transmission line and the switch limit the available input power at the structure. The nominal operating point for designing the gun, magnet, and diagnostics was set at 500 kW. The power is monitored by a series of mm-wave Schottky diodes with sub-ns rise time. The diodes are calibrated to provide an absolute power value, which is needed to calculate the resulting gradient and structure performance. A diode on the beamline measures the forward power. The power transmitted through the gun structure is measured

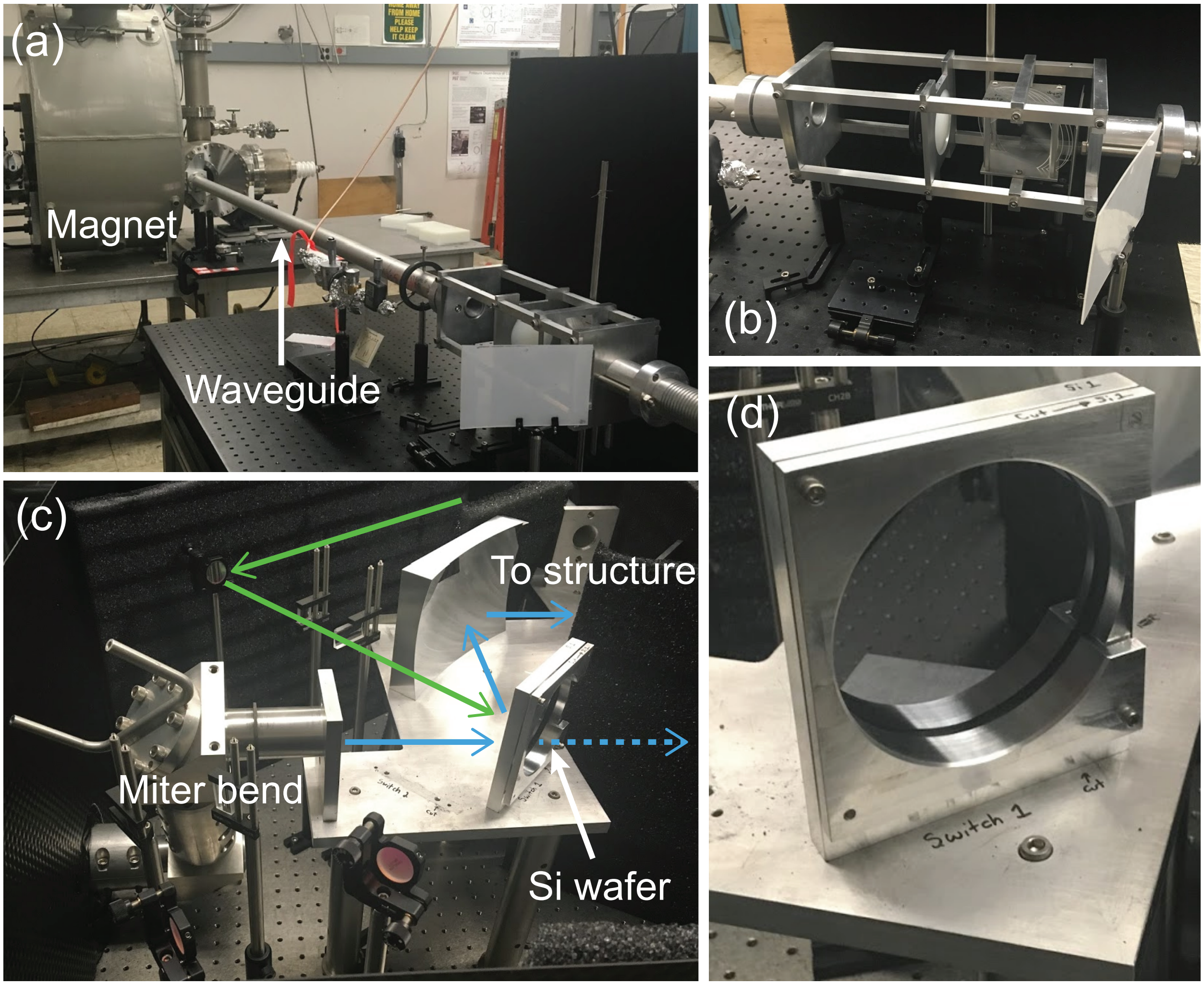

Figure 5.2: (a) View of the gyrotron. The gyrotron magnet and HE_{11} corrugated waveguide are indicated. (b) Variable attenuator in the gyrotron transmission line. (c) View of the switch setup. The THz beam path is marked by the blue arrows. A miter bend in the corrugated waveguide is used to direct the beam at the switch. When the Si wafer is made reflective by the input laser, it reflects the beam into a focusing mirror and on to the structure. Otherwise, the Si wafer is transparent (indicated by the dashed arrow). The laser path is indicated by the green arrow. (d) Close-up view of the Si wafer.

using the WR-8 diagnostic port (see Sections 3.4 and 5.3). The reflected power is measured using a diode pointing at the input of the Gaussian horn. Together, these values can be used to calculate the power dissipated in the structure and monitor for signatures of breakdown.

5.3 Gun assembly

The gun assembly was designed such that the cell structure would be fully demountable from the Gaussian horn and mode converter block. However, the system still needs to be vacuum-compatible for high power operation. Rather than bonding the cells to the block through brazing, a housing assembly is brazed to the horn/mode converter block. The gun cells are aligned using a holder that mates with the alignment feature on the block. A ceramic ball is used with a spring and set screw to provide pressure directly onto the cells to ensure good electrical contact. The holder and spring assembly are vented and connected to the full assembly vacuum space via vents machined into the horn/mode converter block. The gun housing is welded to a 2.75 inch conflat flange which is sealed for vacuum. A model of this portion of the assembly is shown in Figure 5.3.

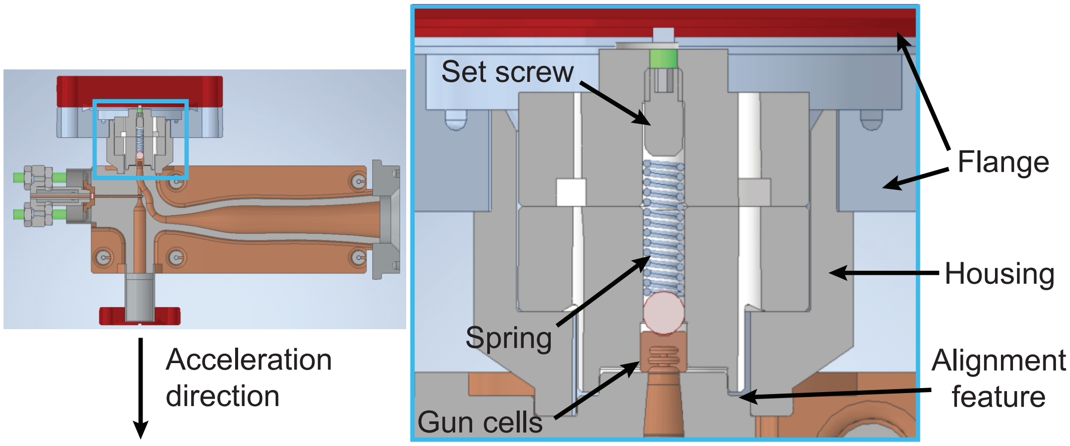

Figure 5.3: Cross section of the gun assembly focused on the gun mounting and alignment hardware. The gun cells and acceleration direction are indicated. The gun is pressed against the input waveguide using a ceramic ball and spring. The outer housing is brazed to the mode converter block and sealed with a flange. Details of the Gaussian horn and mode converter block can be found in Section 4.2.1.

The WR-8 diagnostic port off of the beam tunnel is sealed with a ceramic window. The ceramic is metalized and brazed into a copper ring which is then brazed to a larger weld fixture. There is a section of WR-8 waveguide outside of the vacuum to measure the port. On the beam tunnel side, a tube with a welded 1.33 inch conflat flange is brazed around the opening. This flange is small enough to fit inside the bore of the focusing solenoid (Section 5.4), allowing the solenoid to be placed at the output of the block beam tunnel. Models of the diagnostic port and beam tunnel vacuum fixtures are shown in Figure 5.4.

The Gaussian horn opening is connected to an input window assembly. The gyrotron beam must be focused onto the horn opening. The beam waist after the switch is about about 47 mm. A dielectric lens is used to focus it to a 4.5 mm waist at the input of the

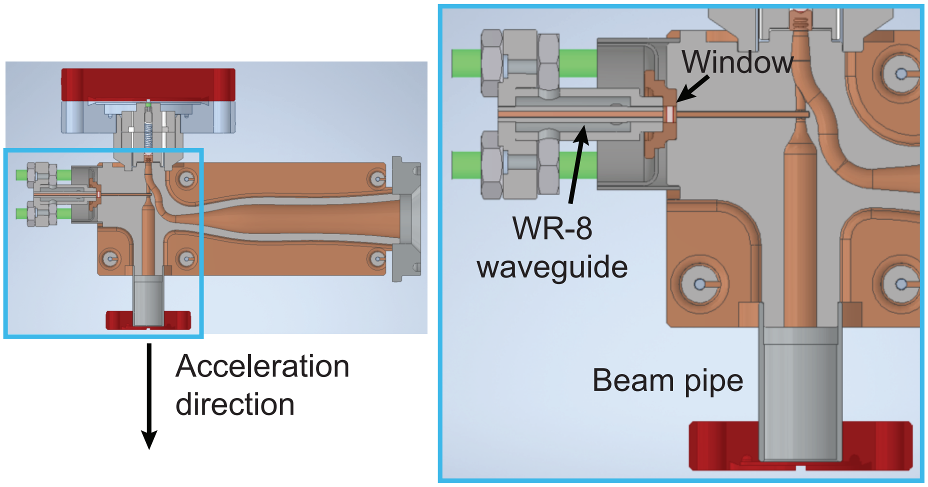

Figure 5.4: Cross section of the gun assembly focused on the WR-8 diagnostic port and the beam tunnel. A ceramic window in the WR-8 waveguide seals the vacuum. A stainless steel beam pipe is brazed to the output of the mode converter block beam tunnel.

Gaussian horn. The input pulse then travels through the TE_{11} to TM_{01} mode converter into the gun structure, as described in Section 3.4. If the input beam were focused in air onto a window directly in front of the horn opening, the high power could potentially cause damage to the window. Instead, a lens is placed against a large high power fused silica window at a significant distance from the horn and the focusing occurs in vacuum. A model of the high power window assembly is shown in Figure 5.5. The window thickness of 0.275 inches was chosen such that there would be maximum transmission at 110.08 GHz. The diameter of the window is 3.88 inches and it is mounted in a 6.75 inch diameter conflat flange (CF).

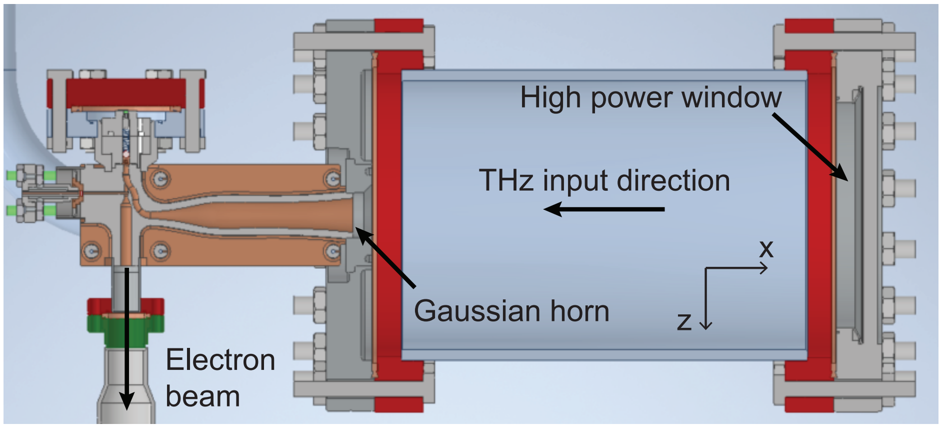

Figure 5.5: Cross section of high power window assembly and the gun assembly. The input gyrotron pulse passes through a lens (not pictured) followed by a window and is focused on to the Gaussian horn.

5.4 Solenoid

5.4.1 Theory of solenoid focusing

A solenoid electromagnet consists of a current-carrying coil surrounding a center bore. The field in the center of the bore points along the axis through its entire length. The fields make a closed loop around the outside of the coil and thus the fields point in opposite directions at either end of the magnet. A schematic of a standard solenoid field is shown in Figure 5.6.

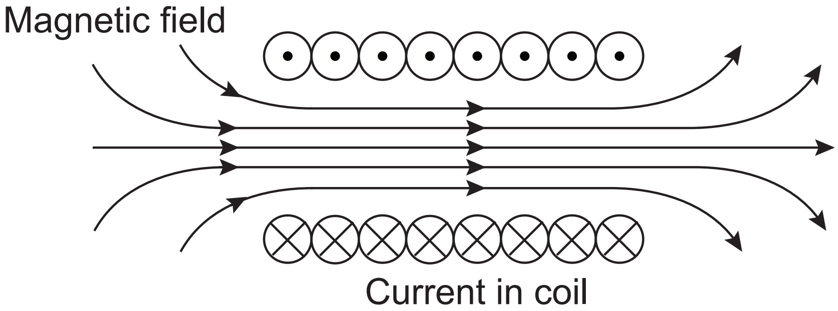

Figure 5.6: Schematic of an electromagnet solenoid. Current flows in and out of the page in a coil. The resulting field is purely along the solenoid axis in the center and diverges at the edges.

In the simplest picture, the magnetic flux density of an infinite solenoid is given by

$$B = \mu \frac{NI}{\ell} \tag{5.1}$$

where NI is the current-turns of the coil and ℓ is the length. When discussing magnets, the magnetic flux density is frequently referred to as 'the magnetic field' and is given in units of Tesla or Gauss. In a finite solenoid, there are both radial and longitudinal components. The longitudinal fields are strongest in the center of the magnet and the radial fields are strongest at the edges. For an axisymmetric solenoid, the field can be written as

$$\mathbf{B} = B_r\left(r,z\right)\hat{r} + B_z\left(r,z\right)\hat{z}, \tag{5.2}$$

where B_r is the radial component and B_z is the longitudinal component. Their dependence on the coordinates r and z is given by

$$B_z\left(r,z\right) = B\left(z\right) - \frac{r^2}{4}B''\left(z\right) + \cdots, \tag{5.3}$$

$$B_r\left(r,z\right) = -\frac{r}{2}B'\left(z\right) + \frac{r^3}{16}B'''\left(z\right) + \cdots, \tag{5.4}$$

where $B(z)$ is an arbitrary field varying in z [78]. Typical calculations use only the first order terms and assume $B\left(z\right) \approx B_0\left(z\right) = B_z\left(r=0,z\right)$. In other words, the longitudinal field is assumed to depend only on z, which is applicable when the radius of the solenoid bore is much smaller than its length. Neglecting all but the first term, the radial component varies as

$$B_r = -\frac{r}{2}B_0'\left(z\right). \tag{5.5}$$

Solenoid focusing occurs as a consequence of the fields at the end of the magnet. In the center of the magnet, the particles are moving in a uniform field and as a result follow circular orbits. This motion is not responsible for focusing, but introduces necessary quantities to describe the particle motion. The orbit has a radius ρ given by

$$qvB = \frac{\gamma m v^2}{\rho} \tag{5.6}$$

where q is the charge, v is the velocity, and m is the mass. The radius is used in defining the magnetic rigidity

$$B\rho = \frac{p}{q} \tag{5.7}$$

using the relativistic momentum $\mathbf{p} = \gamma m \mathbf{v}$. This motion is further characterized by the associated angular frequency ω_C, known as the cyclotron frequency. The cyclotron frequency is given by

$$\omega_C = \frac{qB}{\gamma m}. \tag{5.8}$$

When particles move through the radial fields at the edge of the magnet, they are given an azimuthal component of momentum which results in a separate orbit. The radius of this orbit is such that it is tangential to the solenoid axis, $r = 0$. The angular frequency of this motion is the Larmor frequency, defined by

$$\omega_L = \frac{\omega_C}{2}. \tag{5.9}$$

The radius of this orbit is $\rho_L = \rho_0/2$, where ρ_0 is the initial radius from the solenoid center when the particle enters the magnet. Thus, the particle distance from the solenoid axis is varying as it travels through the magnet. At the exit of the solenoid, azimuthal momentum is transferred to radial momentum, the magnitude of which is determined by the distance from the solenoid axis. The field strength and length of the solenoid can be designed such that this radial momentum is towards the solenoid axis, resulting in focusing [79]. Solenoids are distinct from quadrupole doublets or triplets in that they focus in both x and y simultaneously (assuming the beam is symmetric in these planes beforehand). Approximations can be applied to define a focal length and other analogies to optical lenses.

5.4.2 Design and modeling

Unlike the idealized cases typically used for analytical calculations, the beam produced in this gun has both angular divergence and energy spread. While a solenoid can focus the beam, the focusing is less ideal. For the purposes of this experiment, it was not necessary to tightly focus the beam in the same way that would be required in an electron microscope, for example. Instead, it was necessary to limit the divergence of the beam to prepare it for the energy spread measurement. The solenoid was designed to act primarily as a collimator with a small amount of focusing to reduce the beam size.

Initial simulations were performed using the built-in GPT `Bzsolenoid` field. The field describes a simple, homogenous, finite solenoid:

$$B_z = \frac{1}{2}\mu_0 \left(\frac{z + \frac{1}{2}L}{\left[\left(z + \frac{1}{2}L\right)^2 + R\right]^{1/2}} - \frac{z - \frac{1}{2}L}{\left[\left(z - \frac{1}{2}L\right)^2 + R^2\right]^{1/2}} \right) nI \tag{5.10}$$

$$B_r = -\frac{r}{4}\mu_0 \left(\frac{1}{\left[\left(z + \frac{1}{2}L\right)^2 + R^2\right]^{3/2}} - \frac{1}{\left[\left(z - \frac{1}{2}L\right)^2 + R^2\right]^{3/2}} \right) nIR^2. \tag{5.11}$$

The solenoid length L and radius R are specified in meters. The current is input as nI in units of Ampere-turns per meter. The fields do not account for any finite thickness of the solenoid coil. Simulations were performed to determine preliminary values for L, R, and nI. The target was to provide a collimated beam several cm downstream at the dipole. For chosen values of L and R, the `gdfsolve` utility was used to optimize β_x and β_y while maintaining a reasonable x and y size. Further adjustments were made to optimize the energy spread distribution, discussed in Section 5.5.

Once optimized values were chosen, a realistic solenoid was modeled in ANSYS Maxwell [80]. Maxwell is a finite element code capable of simulating magnetic fields in 2D and 3D. The solenoid was designed to be axially symmetric and therefore 2D simulations were used. There were a number of practical factors considered in designing the full coil. A physical magnet requires the coil to have a finite thickness. For a given current per unit length, any finite thickness results in a lower field in the bore than an infinitely thin solenoid. However, the thickness determines power dissipation in the coil. The power dissipated in a resistive material due to a current is given by Ohm's law,

$$P = I^2 R. \tag{5.12}$$

Using material resistivity ρ in units of Ohm-meters, this can be used to find the volumetric power dissipation, $P_V = J^2\rho$. With the current value fixed, a thicker coil reduces J and therefore the power dissipated per unit volume.

A thickness of $t = 1$ cm was chosen to keep the total dissipated power $P_{diss} = P_V V \lesssim 100$ W. Figure 5.7 shows the resulting vector field. The values match well with the GPT analytical formula. After the initial design, the current was increased to counteract the effects of fringing fields of the dipole magnet. The field shown in 5.7 reflects this increase. Table 5.1 summarizes the final parameters of the design. The design assumes only 75% of the coil design cross-section will be conductors. This accounts for a realistic packing fraction of wire windings to create the coil. The dissipated power calculation assumes the coil wires are copper with $\rho = 1.71 \times 10^{-8}$ Ωm.

Parameter	Value	Description
ℓ	12.1 cm	Coil length
r	2 cm	Bore radius
t	1 cm	Coil thickness
nI	5.68 kA-turns	Current
f	0.75	Packing fraction of windings
A_w	9.1 cm^2	Cross sectional area of windings
J	6.25 MA/m^2	Current density in windings
P_{diss}	95.5 W	Power dissipated

Table 5.1: Design values of the solenoid.

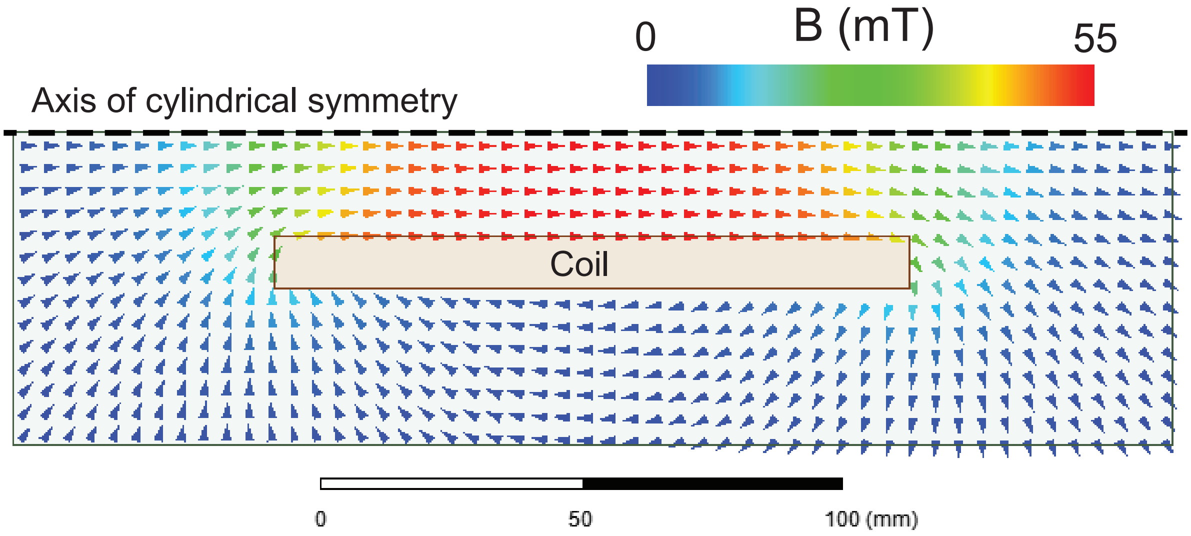

Figure 5.7: Simulated magnetic field of the solenoid. The simulation is in 2D and assumes cylindrical symmetry. The field in the center of the solenoid is 55 mT for 5.68 kA-turns of current in the coil.

5.4.3 Fabrication

The solenoid was constructed by wrapping the copper wire coil around an aluminum bobbin. The bobbin contains openings for the wire leads. To assist with maintaining the magnet temperature, a sheath of aluminum fins was made to fit around the bobbin. The internal bore of the solenoid was designed to be large enough to accommodate a 1.33 inch conflat flange. This allows the solenoid to be placed immediately against the output of the beam tunnel of the Gaussian horn/mode converter block. Figure 5.8 shows the model and photo of the fabricated solenoid.

To confirm the solenoid performance, measurements were taken along the axis of the solenoid using a probe mounted on a motorized translational stage. The result is shown compared to the simulated field in Figure 5.9.

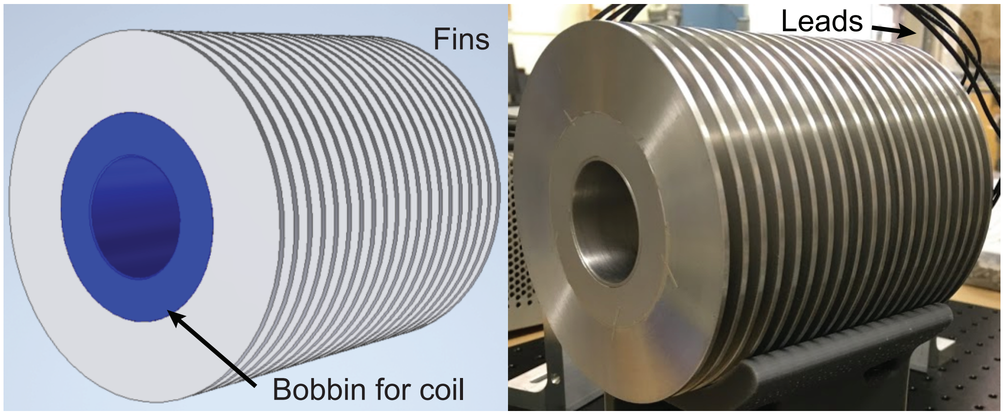

Figure 5.8: Model and photo of the solenoid magnet. The coil is wound on a bobbin and surrounding by a sheath of fins to dissipate heat.

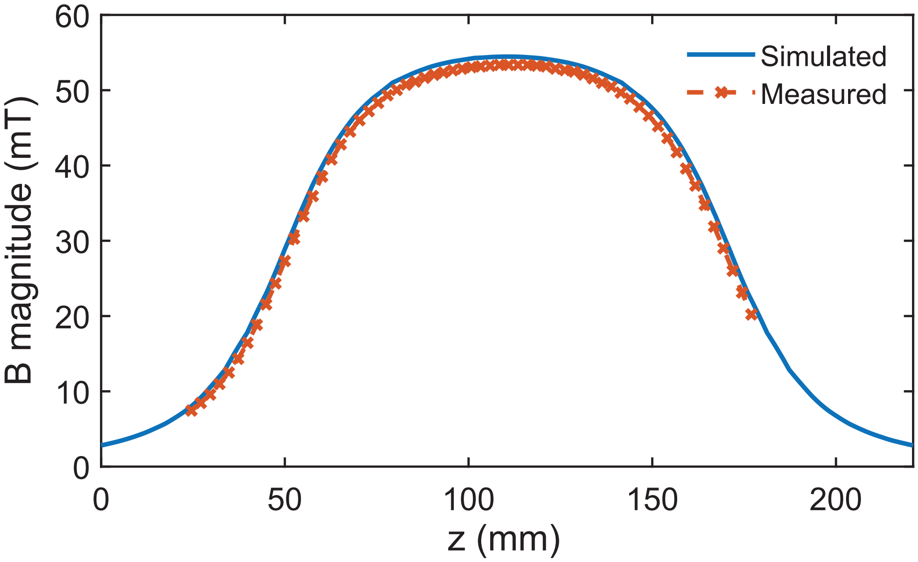

Figure 5.9: Simulated and measured field on-axis in the solenoid. The range of the measurement was limited by the translational stage.

5.5 Energy spread spectrometer setup

The principle of a spectrometer is to separate components of a beam for measurement. A spectrometer can create a correlation between a property of the particles and a measurable quantity on the detector. They are used when the property of interest can not be directly measured or varies across the beam. A common example is a mass spectrometer, which uses a magnetic field on a beam of ions to separate them based on their mass-to-charge ratio.

This spectrometer setup is built to measure the energy spread of the electron beam produced by the gun. A dipole magnet is used to bend the trajectory of the beam. The bending radius of each particle depends on its energy. Thus, the distribution of the electrons on the detector is linked to the energy spread of the beam. This type of measurement is challenging for beams like the one expected from this gun. The energy is relatively low and thus measuring the energy spread requires being able to resolve differences on the order of tens of keV. This corresponds to a very small difference in the bending radius of the particles. Since the energy is not dependent on the transverse distribution of the particles, the energy-based distribution can be buried within the general spread of the beam without careful design. The following sections detail the design of this setup. Throughout, the magnet-induced spatial spread of the beam is referred to as a 'streak' to distinguish it from the energy spread.

5.5.1 Dipole

As in the case of the focusing solenoid, very low magnetic fields are required to steer the beam when it is sub-relativistic. The bending radius of a charged particle in a magnetic field was introduced in Equation 5.6. It can be rewritten in terms of the relativistic γ and β as

$$\rho = \frac{mc\gamma\beta}{qB} \tag{5.13}$$

where m is the mass, c is the speed of light, q is the charge, and B is the magnetic field. Higher energy particles have a larger bending radius than lower energy particles, so they follow a shallower trajectory. In the spectrometer setup, this spreads the beam over the detector based on the energy spread.

Bending magnets are typically dipoles. The field of a simple dipole points from one pole to the other at every location in the gap between the two poles. A charged particle entering the gap feels a force perpendicular to the field and its direction of travel. A schematic of this is shown in Figure 5.10 for an electron. A real dipole has fringing fields outside of the gap that fall-off with a distance largely determined by the gap size.

Simulations were performed in GPT to model a dipole bending magnet. The initial model used the built-in `sectormagnet` element which models an idealized bending magnet based on an a specified bending radius and magnetic field. The model can include fringing fields for a small distance outside of the magnet.

The bending-induced spread must be dominant over the beam size and divergence. In many cases, it is logical to focus the beam to the smallest size possible before passing through the dipole. This maximizes the divergence of the beam, but for a significant streak the energy-based spread will be larger. For the $\sim$ 500 kW beam expected from this gun, simulations showed that the divergence dominated and thus obscured the energy spread information. Instead, the best streak occurred when the beam was collimated by the solenoid and bent at a high angle. After the bend, the particles were allowed to drift which increased the

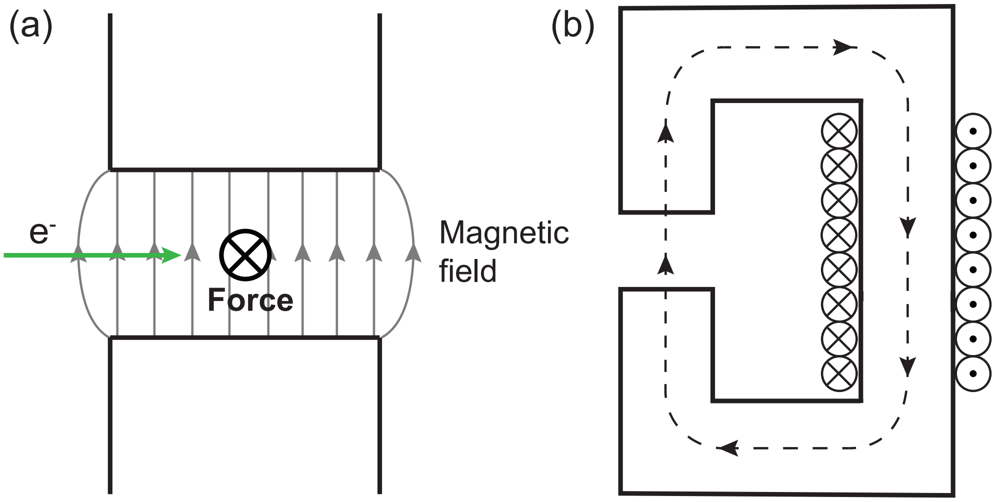

Figure 5.10: Schematic of a dipole magnet. (a) The field in the gap exerts a force on the particle perpendicular to its velocity. (b) Example geometry of an electromagnet dipole. A coil around a magnetic core creates a field in the gap.

separation between energy bins. The beam size is small enough that it was preferable to limit the divergence to allow for this drift region. The streak quality was determined based on the resolution of a microchannel plate detector (MCP) which is described in the next section.

After initial values of the optimal bending radius and field were found using GPT, a real dipole was modeled in Maxwell 3D. This produced a significantly more complex field and required shaped pole pieces to produce the required streak quality. Figure 5.11 shows a solid model of the dipole and pole pieces. The magnet consists of a coil with a steel core and nickel-plated steel pole pieces. In order to accommodate the desired MCP size, the dipole had to be designed with a large gap. The coil is kept out of the vacuum and the magnetic field in the gap is enhanced by the pole pieces and steel plates added to the vacuum flange.

Due to the large gap size, there are significant fringing fields along the length of the beam pipe which cause the beam to drift off-axis. To counteract this, a steel shielding tube was added between the solenoid and the dipole. The two magnets were modeled together in one Maxwell 3D simulation to calculate the field everywhere in the assembly. Figure 5.12 shows the fields of the combined solenoid and dipole simulation. The dipole field in the gap is about 25–28 mT. Like the solenoid coil, the dipole coil was designed to minimize the dissipated power. The design parameters of the coil are summarized in Table 5.2. The results of the Maxwell simulations were used to model the full assembly and the streak, discussed in the next section. Photos of the assembled pole pieces and dipole coil are shown in Figure 5.13.

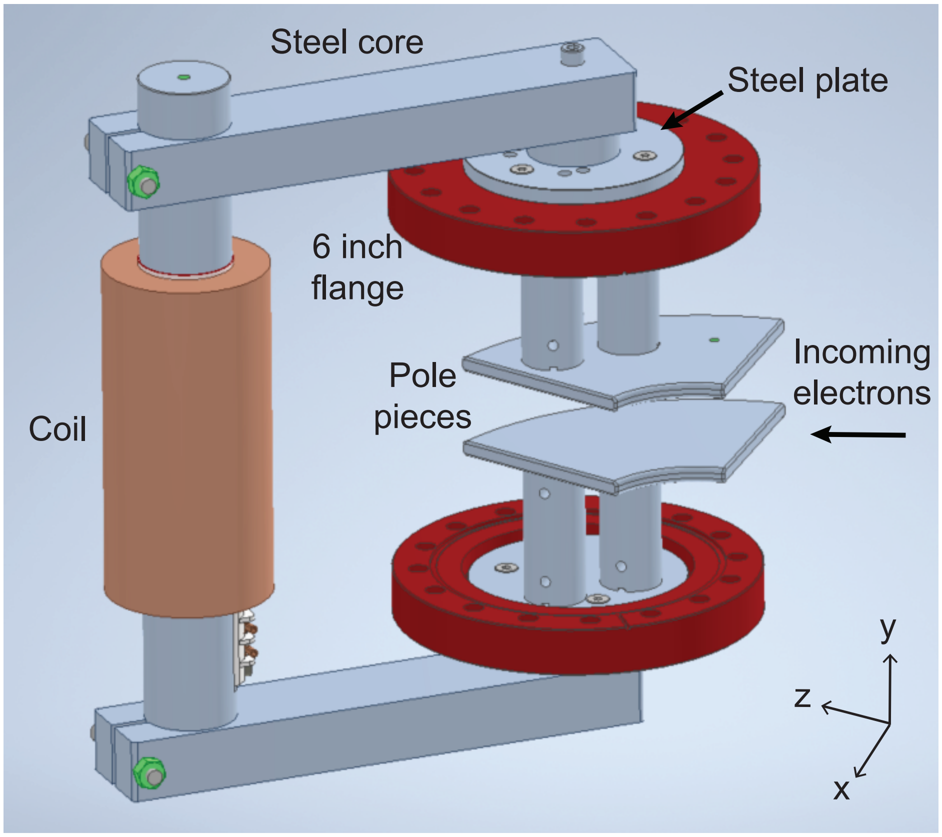

Figure 5.11: Model of the dipole magnet for the spectrometer assembly. The magnet consists of a coil around a steel core. The dipole is mounted on 6 inch conflat flanges. Inside vacuum there are nickel-plated steel pole pieces. The electrons enter the gap along the z axis and are bent towards x. The field for spreading the beam towards the spectrometer detector points in the positive y direction.

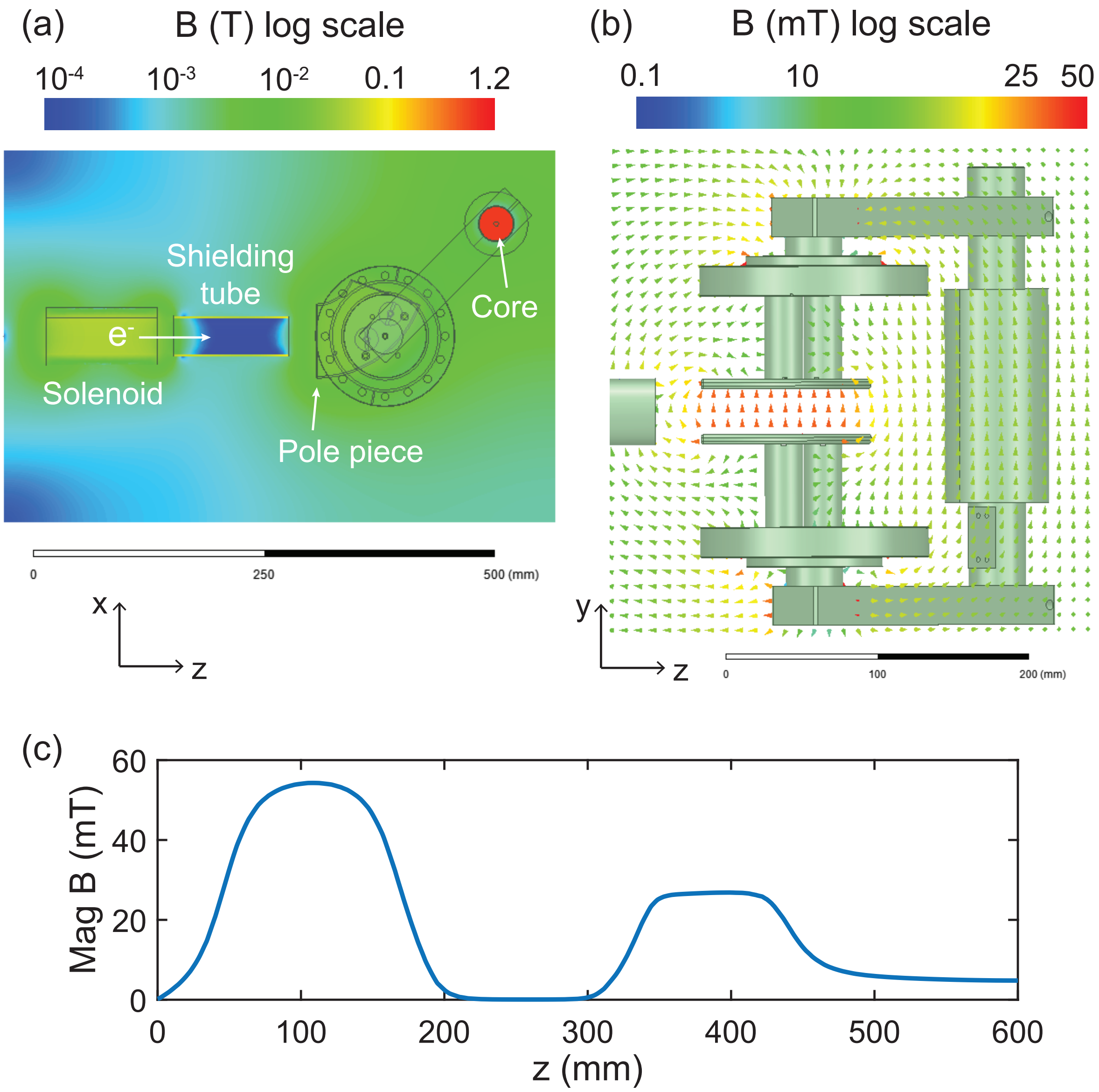

Figure 5.12: Results from the Maxwell 3D simulation of the solenoid and dipole magnets. (a) The magnitude of the B field in the x-z plane. The electron beam is traveling in z until it reaches the dipole. The field is strongest in the steel core of the dipole. (b) The vector B field in the y-z plane. The scale limits are reduced to show the field in the gap. Note that the coil is not in the y-z plane at $x = 0$ and so the field in the core is not shown in this view. (c) The on-axis magnitude of the B field through the full length of the simulation. The fields after the dipole show what the fringing fields in the beam pipe would be without the shielding tube, which reduces the field to zero.

Parameter	Value	Description
ℓ	14 cm	Coil length
r	1.95 cm	Bore radius
t	1.5 cm	Coil thickness
nI	1.55 kA-turns	Current
f	0.6	Packing fraction of windings
A_w	12.6 cm^2	Cross sectional area of windings
J	1.23 MA/m^2	Current density in windings
P_{diss}	3.1 W	Power dissipated

Table 5.2: Design values of the dipole coil for the energy spread spectrometer.

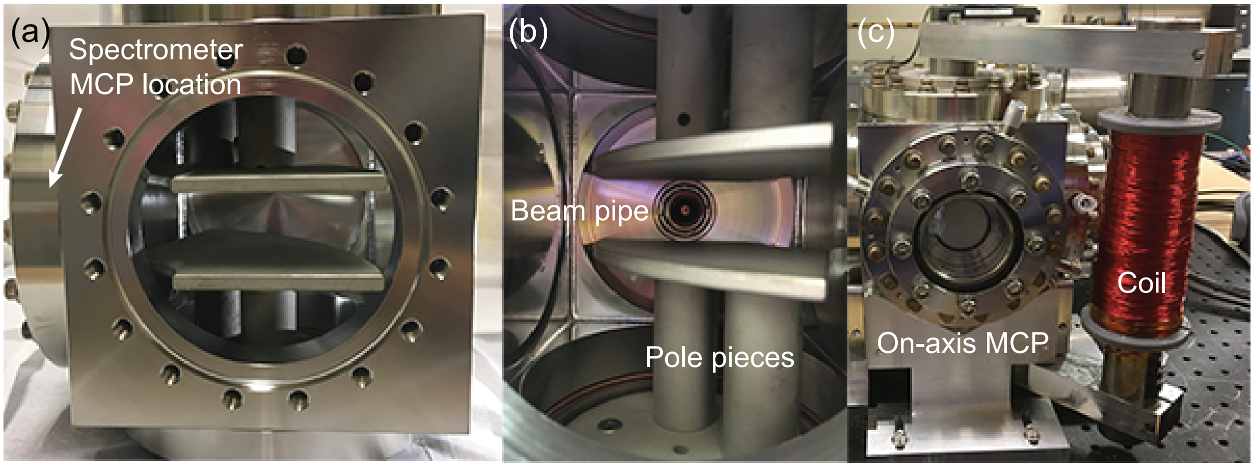

Figure 5.13: (a) View of the pole pieces from the location of the beam pipe. The spectrometer MCP (not shown) would be to the left. (b) View from the opposite end facing the beam pipe. (c) The dipole coil mounted on the cube. The on-axis MCP assembly is indicated.

5.5.2 Microchannel plate detector

The detector used in the spectrometer setup is a microchannel plate detector (MCP) coupled to a scintillating phosphor screen. MCPs are commonly used detectors which can measure single electrons. They operate by multiplying the input electron signal via secondary electron emission. A microchannel plate consists of μm-scale channels in a thin plate of resistive material. The channels are at a shallow angle with respect to the face of the plate. When an electron enters a channel, it hits the wall and causes secondary electron emission. These electrons go on to cause a cascade. A bias voltage ensures that the electrons travel through the channel to the readout device, which can be an anode or screen. On a phosphor screen, the electrons cause visible photons to be emitted, creating an image of the spatial positions of the electrons. MCPs are characterized by their channel size, pitch (spacing between channels), gain, and overall detection area.

Using the magnetic fields calculated in Maxwell, GPT simulations were performed to model the full beam transport and streak. The dipole bends the beam at an almost 90° angle. The beam then travels primarily along the x direction towards the MCP. Particle energies were recorded at specific y-z planes at various x locations off-axis, modeling the location of the MCP. The results were binned according to the spatial resolution of a chevron-type MCP with a phosphor screen. The chevron MCP uses two plates, which reduces the spatial resolution but increases the gain. The goal of the spectrometer streak is to match the z positions on the detector to the energy spread of the beam. Thus, optimization of the spectrometer setup was aimed at minimizing the overlap between spatial bins at different energies for a desired energy resolution. Examples of a high and low quality streak are shown in Figure 5.14. Figure 5.15 shows the spatial distribution of particles on the detector and the counts along z.

A large-area MCP chosen to allow for a significant spread in z. The detector is a Hamamatsu F2225-21PGF which consists of two MCPs with a phosphor screen. The diameter of the detectable area is 40 mm with a minimum gain of 10^6. The minimum achievable spatial resolution of the assembly is 80–100 μm. The MCPs and screen are mounted on a 6 inch conflat flange with a viewport for imaging the screen outside of vacuum. The first MCP is located 65 mm from the beam axis. A model of the spectrometer assembly is shown in Figure 5.16 including example particle trajectories. Photos of the MCP detector are shown in Figure 5.17.

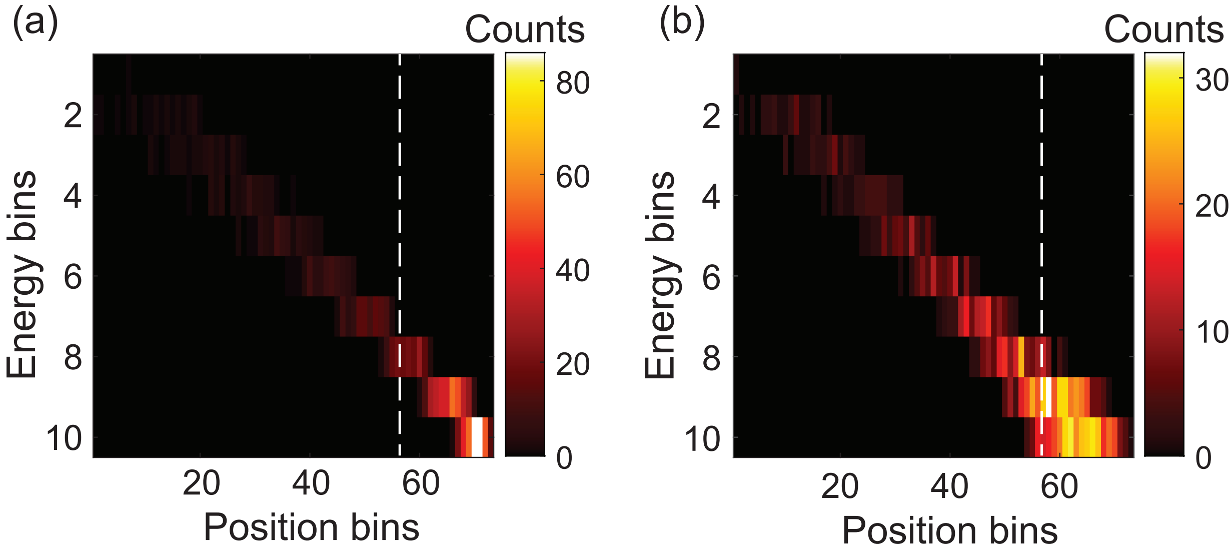

Figure 5.14: Energy spectrometer histograms with $\gamma = 0.01$ ($\sim$ 5 keV) energy bins and 80 μm position bins. These plots are focused on particles within 5% of the peak energy. For a perfect streak, one position in should correspond to only one energy bin. (a) Streak for the nominal operating configuration with a 1.55 kA-turns dipole current. (b) Poor quality streak of the same beam. The dashed line shows that for a certain position on the detector there are several overlapping energy bins. The peak is smeared over a large spatial range.

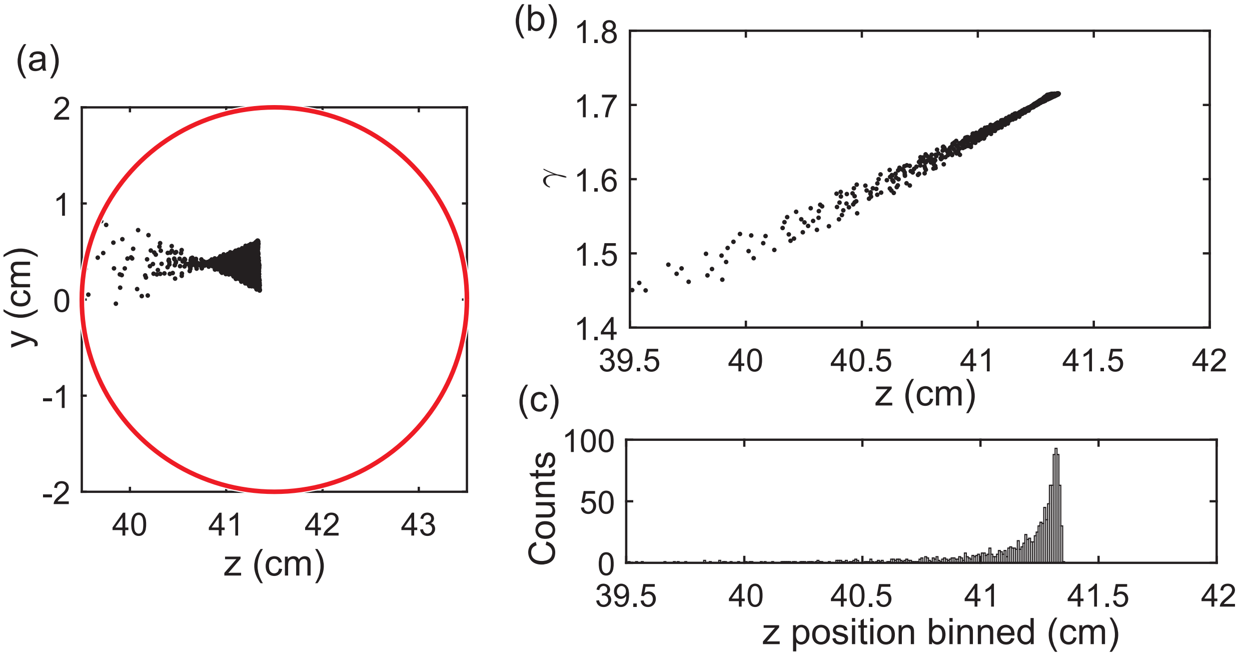

Figure 5.15: Distribution of the streak on the detector for measuring the energy resolution of the peak. (a) Locations where the electrons hit the detector, whose boundary is indicated by the red circle. The entire peak is captured. The dipole current can be changed to shift the distribution on the detector and measure the tail. (b) Plot of z position versus γ for the peak. (c) Histogram of the binned z positions on the detector.

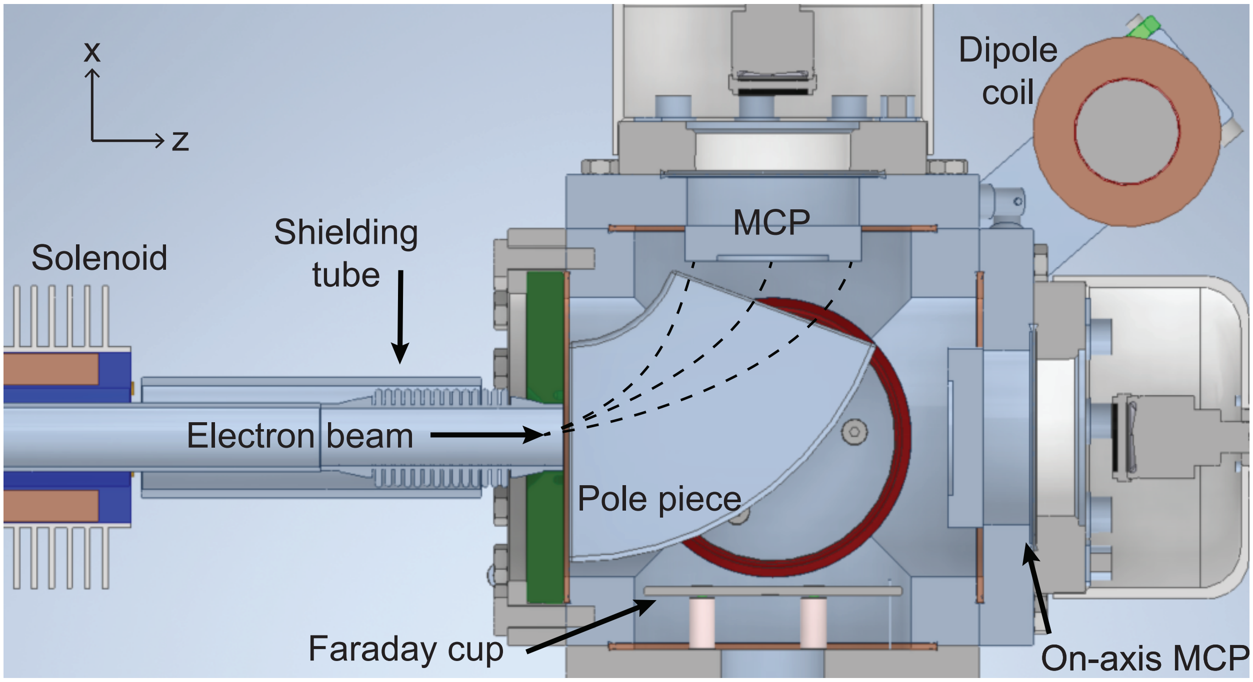

Figure 5.16: Top-down view of the spectrometer assembly. The beam exits the solenoid, travels through a beam pipe, and enters the gap between the dipole pole plates. The dipole bends the beam into the MCP in the y-z plane. Example trajectories are shown as dashed lines.

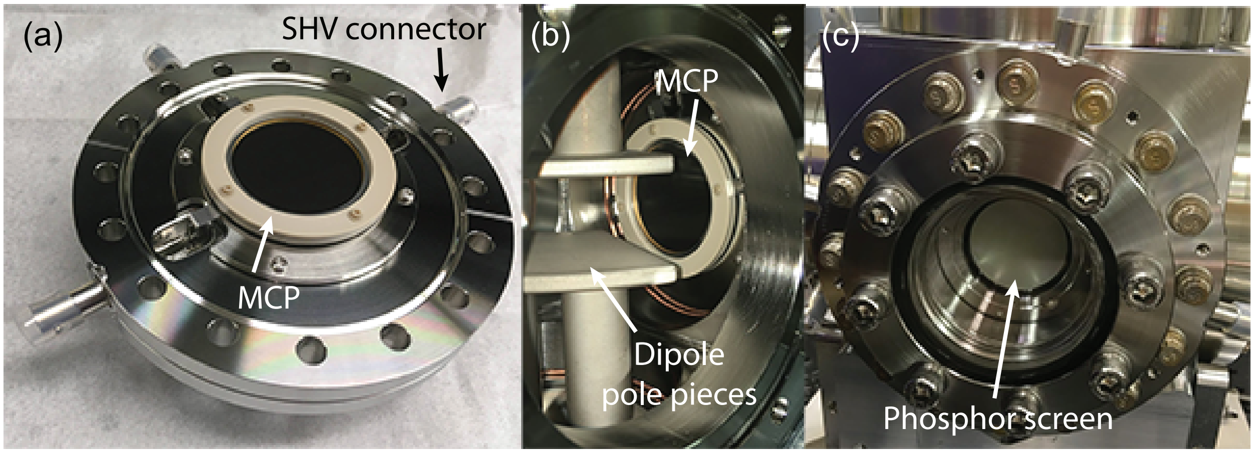

Figure 5.17: (a) MCP side of the assembly. The high voltage (SHV) connectors are also visible. (b) View of the spectrometer MCP mounted on the cube. (c) Outside of the MCP assembly showing the phosphor screen and viewport.

5.5.3 Readout camera

When electrons are incident on the phosphor screen, it emits visible light and can be imaged with a camera. The primary consideration in determining the imaging setup was preserving the spatial resolution. Based on the MCP gain, the number of photons emitted by the phosphor screen will be significant and not require a high sensitivity camera. Timing resolution is also not a concern in this setup. Each measurement consists of a $\sim$10 ns pulse from the gyrotron, which corresponds to many RF cycles. The phosphor screen decay time is several ms, so one image will be taken per gyrotron pulse.

The performance of the imaging system is determined by a number of factors. The sensor size, number of pixels, and pixel size determine the possible field of view and resolution. The lens focal length and the working distance from the object (the phosphor screen) to the lens determine the magnification and also limit the field of view. A CMOS camera and fixed focal length lens were chosen to image the phosphor screen. The camera is an Allied Vision Alvium 1800 U-158m, which has a 1.6 MP Sony IMX273 sensor. The pixel size is 3.45×3.45 μm. The lens is an Edmund Optics 6 mm f/1.85 fixed focal length lens. At the minimum working distance of 50 mm, this allows for a field of view that captures the entire 40 mm diameter of the screen. The object space resolution is roughly 36 μm, below the resolution of the MCP and phosphor screen. The camera is mounted to the MCP viewport at a fixed distance. Neutral density filters can be mounted on the lens if the photon flux is too high. The camera assembly is fully demountable outside of vacuum, so the filters can be changed between measurements. A cross section of the camera, lens, and mount are shown in Figure 5.18.

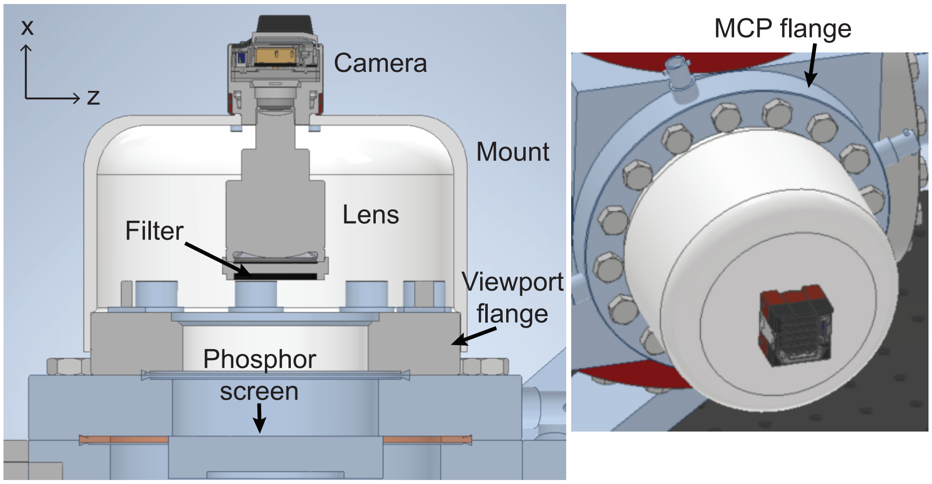

Figure 5.18: Cross-section and model of the camera assembly. The camera is mounted in an enclosure to block outside light. The lens focus is fixed based on location of the phosphor screen.

5.6 Additional detectors

In addition to measuring the energy spread, this setup is also designed to measure the beam size and current. This section describes the detectors included for these measurements. Figure 5.19 shows a model of the detector which is based on a 6 inch conflat flange cube. Three of the openings house the two MCPs and Faraday cup. The top and bottom of the cube are used to mount the dipole.

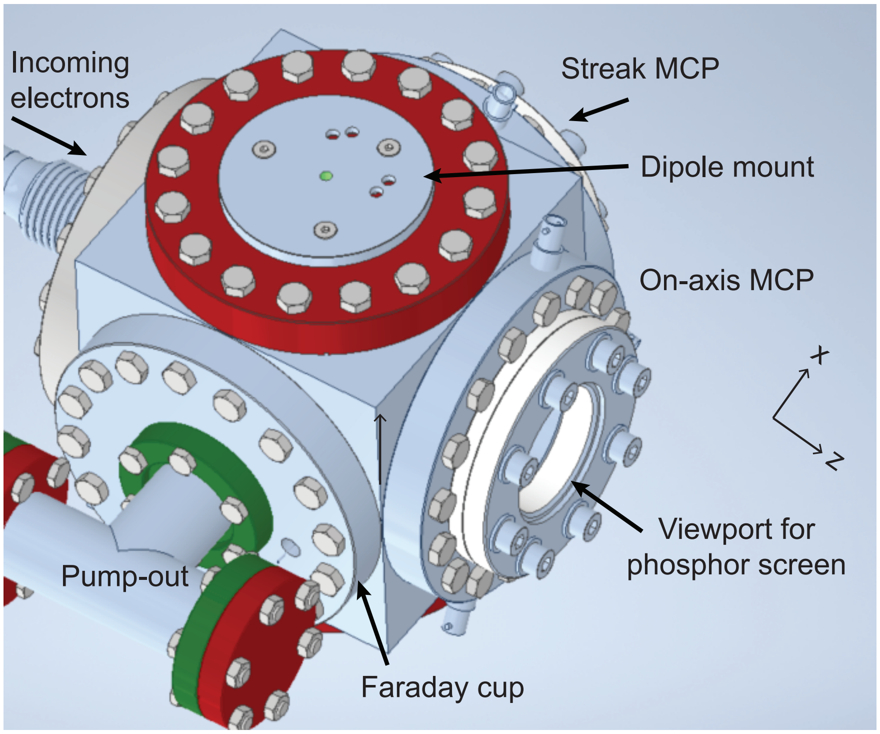

Figure 5.19: Model of the detector cube. On-axis, there is an MCP to measure the beam size. The spectrometer MCP and Faraday cup are on opposite sides of the cube. The dipole (not shown) bends the beam into one or the other depending on the coil current. The top and bottom flanges are modified to mount the dipole. The input beam pipe is also visible. The on-axis MCP is read out using the same camera as in Section 5.5.3, which is not shown. A cross-section inside the cube is shown in Figure 5.16.

5.6.1 On-axis characterization

The spectrometer MCP is located 90 degrees from the original beam path and can therefore only be used with the bending dipole. In order to characterize the beam on-axis without additional steering, a second MCP detector is included on-axis. As described in the previous section, the channels on the plate provide spatial resolution of the detected electrons. The on-axis MCP is identical to the spectrometer MCP, with a 40 mm diameter, phosphor screen, and camera readout.

The beam size at the detector will be on the order of a few mm. Since the resolution of the detector is 80–100 μm, the on-axis MCP can be used to measure changes in the beam size and position when the magnet currents are varied. During commissioning of the setup, the on-axis detector can also be used to confirm the alignment. Figure 5.20 shows the view from the location of the on-axis MCP looking towards the beam pipe.

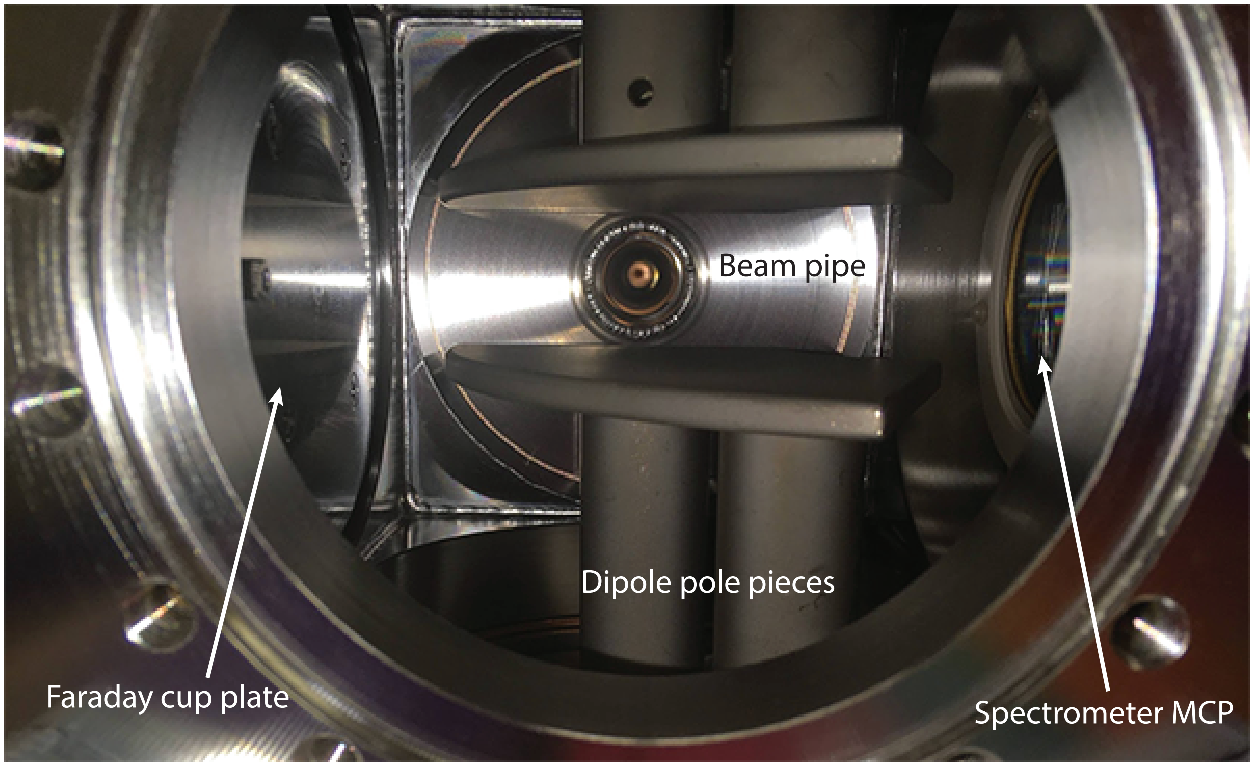

Figure 5.20: View down the beam pipe from the location of the on-axis MCP. The Faraday cup collector plate is visible on the left and the spectrometer MCP is on the right. The beam pipe opening is centered in the dipole gap. The opening to the beam tunnel in the Gaussian horn and mode converter block is faintly visible in the center of the beam pipe.

5.6.2 Faraday cup

A Faraday cup measures the current of charged particles incident on the detector. When the particles hit the metal portion of the detector, there is a net charge which can be read out. The metal is electrically separated from other elements by an insulator. Since electrons are the charge carriers of current flowing in a metal, the current read out directly measures the number of incident electrons.

In this assembly, the Faraday cup is opposite the spectrometer MCP. When the direction of the dipole current is reversed, the field direction in the gap flips. This directs the particles towards the Faraday cup. Due to the shape of the pole pieces, the particles are spread over a larger area than on the MCP. To detect all the particles, the Faraday cup was designed with a large 9.5 cm diameter collector plate. Figure 5.21 shows a model and image of the Faraday cup. The plate is separated from the 6 inch conflat flange with ceramic standoffs. A wire through a vacuum feed-through is used to measure the current.

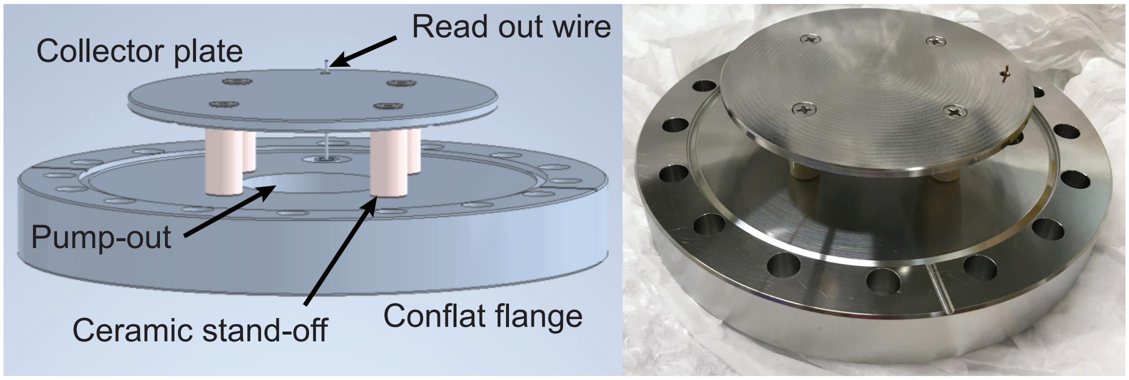

Figure 5.21: Model and photo of the Faraday cup detector. The plate collects the electrons and the current is read out through the wire shown. The plate is mounted using ceramic stand-offs on a 6 inch conflat flange. The flange contains a bore which serves as a vacuum pump-out.

The reversed field of the dipole was calculated in Maxwell and input into the GPT model to confirm the placement and size of the detector was sufficient to capture the particles. The plate is roughly 55 mm from the beam axis. The dipole current used in the calculation was -1.15 kA-turns, lower than the current required for the energy spread measurement. The resulting particle distribution is shown in Figure 5.22.

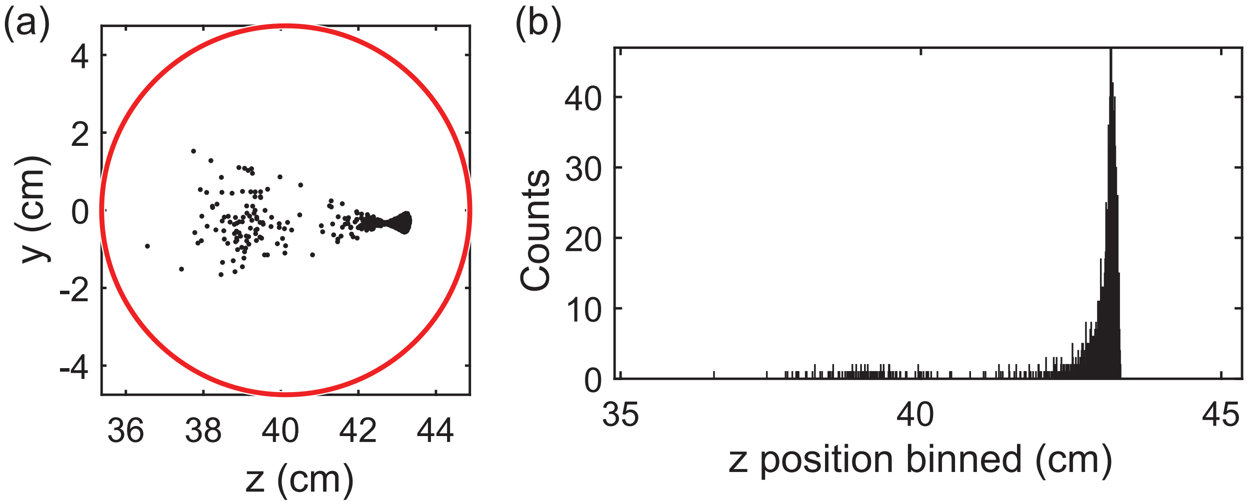

Figure 5.22: Distribution of particles on the Faraday cup plate. (a) Locations where the electrons hit the detector. The red circle represents the boundary of the plate. (b) Histogram of the binned z positions on the plate.

5.7 Vacuum assembly and measurements

The setup was assembled with the tuned structure 4 for high power measurements. The cold test measurements discussed in Chapter 4 primarily used the rectangular to circular waveguide mode converter block presented in Section 4.2.2. In order to confirm the frequencies of the resonances when the cells are mounted in the full assembly (described in Section 5.3), additional measurements were performed. The fused silica window was mounted directly onto the Gaussian horn flange. The added distance of the full high power window assembly is only necessary for focusing the gyrotron beam and was not included in these measurements.

Cold testing was performed using the 3D scanner introduced in Sections 4.2.1 and 4.4.3. The cold tests described in those sections measured the transmitted power by mounting a receiver on the 3D scanner. This method is valuable for characterizing the horn performance, but it does not provide a clear measurement of the resonances. To measure the resonances of the cells in the full assembly, the horn was instead excited by a WR-10 standard horn antenna mounted on the 3D scanner. The horn is not a perfect representation of the high power Gaussian beam, but it excites the structure sufficiently such that the resonances are visible in the reflection signal (S_{11}). By mounting the horn on the scanner, the alignment could be easily varied. Photographs of the setup are shown in Figure 5.23.

In measuring the S_{11}, it is necessary to distinguish between features in the signal due to cavity resonances and those due to reflections from other surfaces. Reflections can be reduced using microwave absorbers and careful alignment. However, some reflections will still occur due to internal features like the area surrounding the horn opening. The features

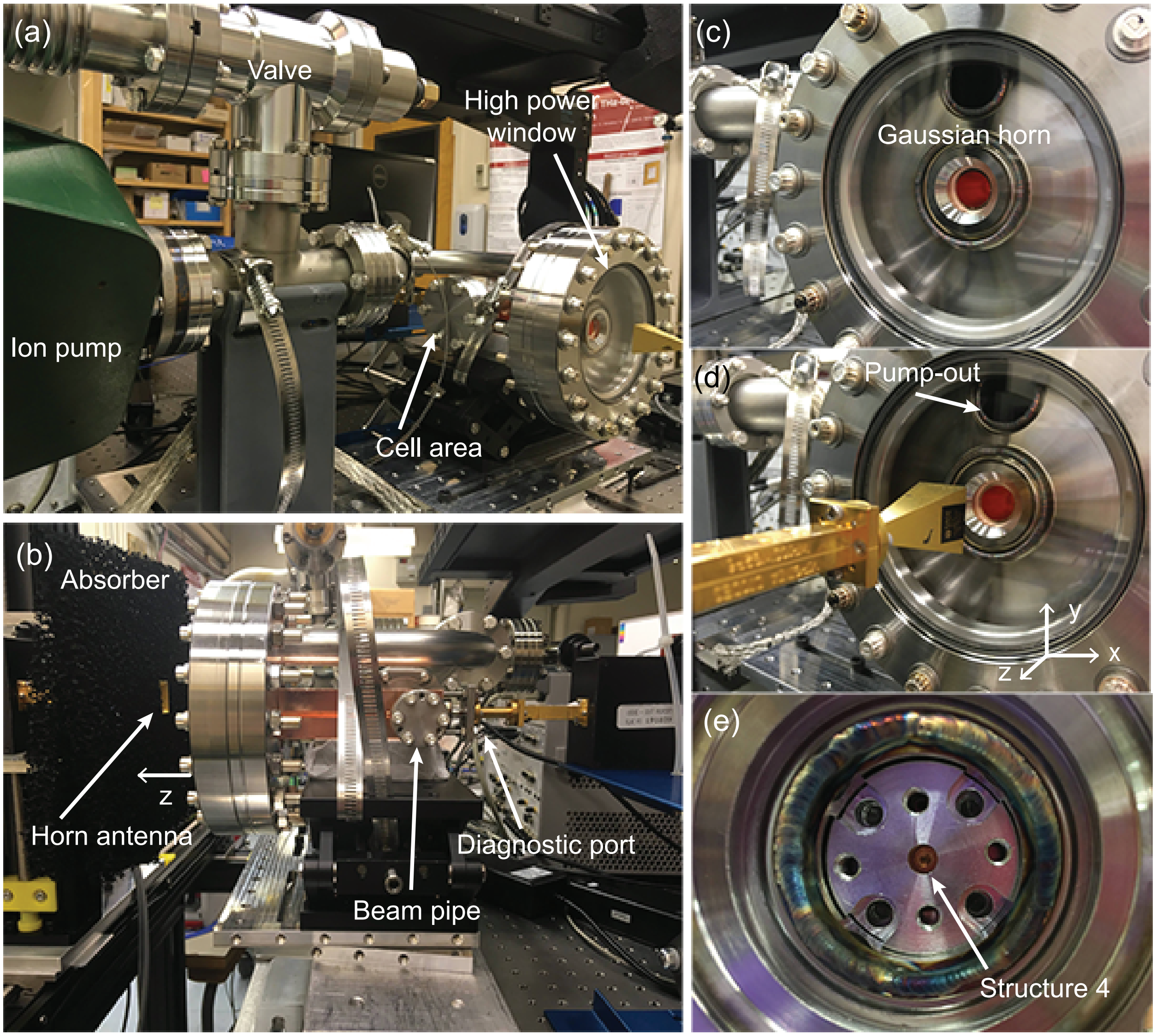

Figure 5.23: Photos of the full assembly cold test setup. (a) View facing the high power window showing the vacuum connections and ion pump. The blank flange labeled as 'cell area' seals the cell mounting section shown in Figure 5.3. (b) Side view of the assembly. The beam tunnel is sealed off with a blank 1.33 inch conflat flange. The WR-10 horn antenna is visible surrounded by absorber. The WR-8 diagnostic port waveguide is also visible and was used to monitor the transmission. (c) View looking in the high power window at the Gaussian horn opening. (d) Image showing the coordinate system of the measurement and the input horn antenna without the absorber. (e) Structure 4 mounted in the alignment holder before the ceramic ball and spring shown in Figure 5.3 were added.

can be distinguished by performing measurements at multiple distances from the structure. The frequencies of the cavity resonances should not shift significantly, but the peaks due to reflections will. Thus, measurements were performed at several planes in z each separated by 5 mm. Two sets of measurements were performed: one with the assembly at atmospheric pressure, and the other with the assembly under vacuum at a pressure of 3.5×10^{-7} Torr. A small frequency shift is expected when the structure is under vacuum. The shift occurs due to the difference in the ϵ and μ of air compared to vacuum. This shift was calculated to be 33 MHz and was confirmed with HFSS modeling of the cells. Results of the two sets of measurements are shown in Figure 5.24.

There are clear resonances in the measured S_{11} that match the previously measured frequencies. In air, the π mode frequency was measured as $f = 110.081$ GHz and the o mode frequency was 109.332 GHz. Based on the calculated shift, the frequencies under vacuum were expected to be roughly 110.114 GHz for the π mode and 109.365 GHz for the o mode. The locations of these values are indicated by dashed lines in Figure 5.24. The resonances visibly shift in air versus vacuum at occur at approximately the correct values. They do not change significantly at different z planes. The air measurements shown in Figure 5.24 were taken after the vacuum measurements, confirming that the electroformed structure can be cycled between air and vacuum without impacting its performance.

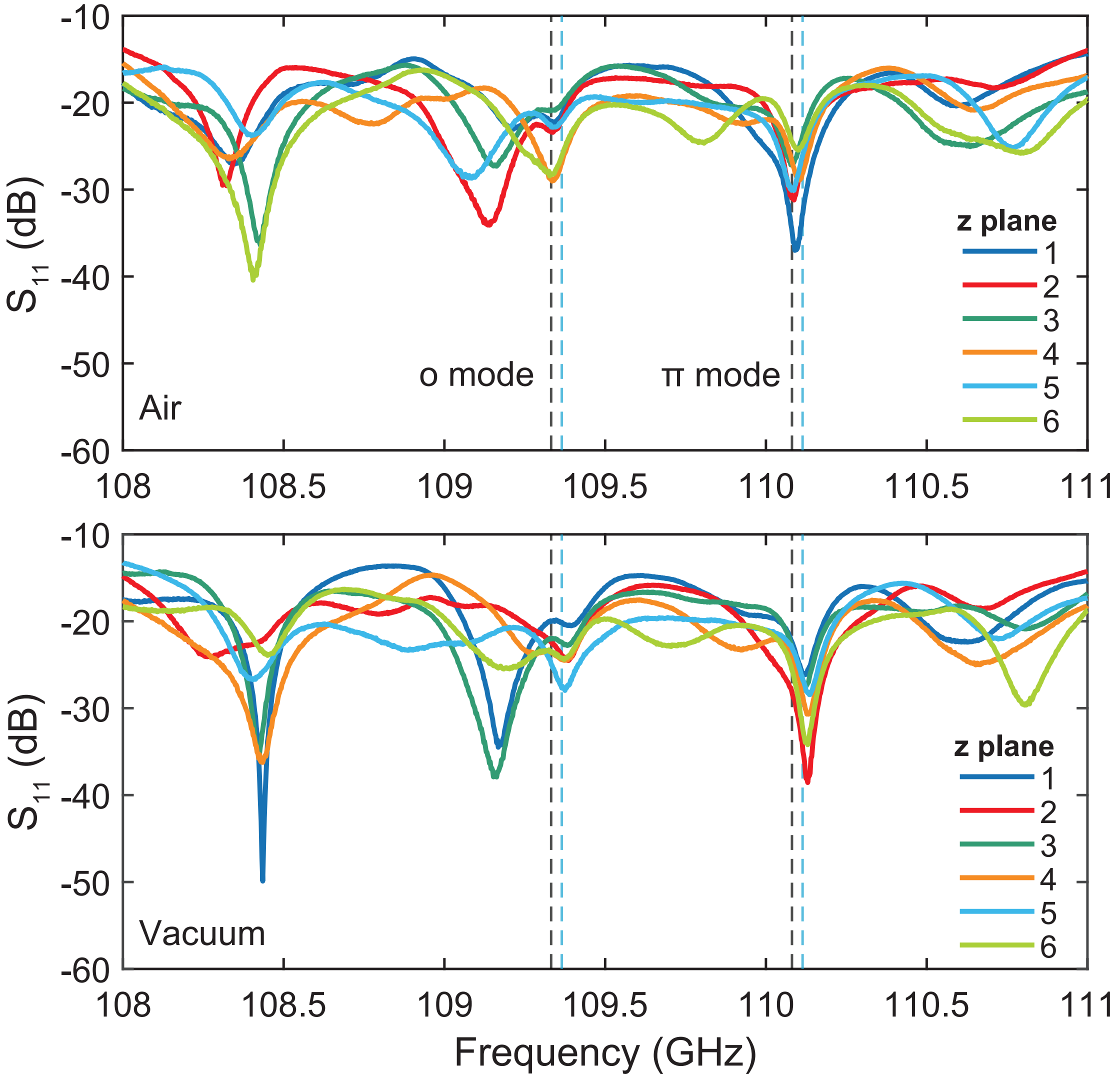

Figure 5.24: Measurements of structure 4 in the full assembly. The top plot shows the S_{11} of the input waveguide horn in air and the bottom plot is the measurement with the assembly under vacuum. The dashed lines indicate the expected resonances in air (black lines) and vacuum (blue lines). The solid lines are measurements at different distances from the horn (z planes). The spacing between the planes was 5 mm. The planes are not at exactly the same distance from the horn in the two cases because the assembly had to be moved. The third persistent resonance just below 108.5 GHz is a resonances from the mode converter which is also visible in simulations. Other features in the signal shift significantly at different z planes, indicating they are reflections.

Chapter 6

Conclusions

Particle accelerators are indispensable tools for modern scientific research. From probing fundamental physics to providing medical treatments to enabling the study of materials in regimes never before possible, accelerators are behind the scenes of many major advances across a broad range of fields. The need for new, more advanced accelerators only grows as scientists aim to explore the natural world on new scales. Electron accelerators are particularly in demand because of their uses both as a direct source of particles and as a vital element of larger facilities. Efforts in electron accelerator research are pushing for improvements on all fronts. Smaller footprints, higher brightnesses, better beam quality, shorter pulses, and better efficiency are all desirable for next-generation facilities. Many of these improvements start at the source: the electron gun. Novel electron sources provide a pathway to the desired improvements in accelerator performance. This thesis represents a substantial step towards a future THz-based electron linear accelerator.

The previous chapters detailed the development of a THz-driven field emission electron gun and an associated beam characterization assembly. Like any accelerator, the electron gun assembly contains a number of elements. The development of the assembly required electromagnetic modeling of the gun cells and magnets, start-to-end simulations of the particle beam transport, and extensive measurements and imaging of the fabricated gun cells. The electron gun operates in a regime that required the development of custom detectors and beamline magnets.

The gun structures produced are the first of their kind. High frequency metallic cavities are themselves fairly new. The use of THz for driving accelerator cavities is also a new area of research that has only become possible with the development of high power sources in recent years. The operating regime of the gun cells is similarly a growing area of study. Operating with very high surface electric fields in order to achieve high gradient has been demonstrated in preliminary experiments, which lay the foundation for this work. Finally, the gun cells were made using advanced fabrication techniques that have not been previously used to build an electron gun.

Multiple designs were considered for the gun cells. Chapter 3 explored the various designs and their limitations and benefits. The design process required a combination of electromagnetic simulations and particle simulations. Two designs were fabricated, one based on a diamond field emitter array cathode and the other using a copper tip cathode. The diamond cathode design has the potential to provide very high brightness beams, but faces some practical limitations. The copper tip design provides good acceleration over a broad range of operating points. As a result, the rest of the beam characterization assembly was designed based on the copper tip gun.

An extensive measurement campaign was performed to study both sets of cells (Chapter 4). Since the fabrication method was previously untested in this context, efforts were made to characterize the structures' performance and understand deviations from modeled values. Overall, the cavity resonant frequencies were lower than their design values and the mode balance and spacing did not match the simulations. Additional simulations were performed to model observed behavior and attempt to identify its source. These efforts showed that the change is due to small deviations in a few key dimensions in the structures. The results of these simulations were used to calculate the potential impact on the gun performance. While the resulting performance would not match the design, the gun cells would still be capable of significant acceleration and would support high surface electric fields. This demonstrates the robustness of the copper tip design, making it an ideal proof of concept structure that can be used to explore these limitations and their solutions.

A major consideration in the practical implementation of W-band accelerator cavities is their tuning. The frequency shift of the fabricated structures provided an opportunity to study methods of tuning the cavities. Simulations were performed to understand tuning based on varying dimensions of the structures as-fabricated as well as temperature-based tuning and shifts from copper plating. Attempts were made to tune the structures with varying degrees of success. The most significant result is the demonstration of mechanical tuning with μm-scale compressions of the structures. Further, these tuning measurements showed that the mode balance and spacing can be corrected, which is vital for a practical accelerator.

The electromagnetic performance of the gun cells was characterized in Chapter 4. Characterizing the resulting beam requires a significantly more complex experiment. The structures must be driven with a high input power to reach the fields required to produce electrons. The resulting electron beam must be focused and steered into detectors. Each of the elements of this system had to be designed specifically for the expected electron beam. Chapter 5 detailed the design of these components. The assembly is designed for use with an existing high power gyrotron source. The demonstrated performance of this gyrotron determined the nominal operating point used in developing the setup. The magnets and detectors were intentionally designed to provide flexibility; the gun cells are capable of operating at a variety of input powers, and thus the beam characterization assembly is can be used to measure the beam at each of these operating points. The resulting assembly is essentially a tabletop accelerator beamline, capable of measuring the energy resolution, size, and current of the electron beam.

High power measurements of the gun cells using this assembly will be performed when the gyrotron source is available. These measurements will be the first demonstration of a THz-based field emission electron gun. They will also provide an avenue to perform breakdown measurements at THz frequencies and study the field emission performance of electroformed copper with very high surface fields. The gun cells are fully demountable from the assembly and multiple structures can be tested with the same setup. Multiple gun structures were tuned to different mode spacings and will therefore have different field balances and acceleration performance. The high power measurements of these structures can be used to verify modeling of the acceleration and beam transport.

There is enormous potential for future work, both with the existing structures and with new designs based on the findings in this thesis. The fabricated structures demonstrated the benefits and limitations of electroforming the gun cells. While some dimensions may deviate from the design, the structures can be mechanically tuned in a way that would not be possible for structures fabricated using the split-block method. Future iterations could be designed with different cell sizes to result in higher frequency structures. The curvature of the cells and irises could also be changed to aid in the fabrication process. The initial copper tip was designed conservatively with a large radius of curvature. Different tip radii could be explored, which would influence the beam emittance and current.

Beyond the copper tip structures, future experiments can be performed using other cathode materials and types. With small design changes based on measurements of the fabricated diamond tip structures, new cells for the DFEA cathodes could be designed. Instead of a field emission cathode, the gun cells could be used with a photocathode material illuminated by a laser pulse. The high fields in the cells would also make it possible to develop a photo-field gun. These designs could provide emittance control while still benefiting from the high gradient acceleration provided by the high frequency cavities.

The electron gun is—both literally and figuratively—only the beginning. The gun assembly presented in this thesis can serve as the injector for a larger accelerator. The same cells used in the gun could be fabricated without the cathode to provide multi-stage acceleration in a W-band linac. With 1 MW of input power, the gun cells alone are expected to produce relativistic electrons. The expected bunch charges are tens of fC. A beam with these specifications matches the typical range used in ultrafast electron diffraction. With additional beam focusing, the gun assembly presented in this thesis could be directly developed into a compact ultrafast electron diffraction system.

Bibliography

[1] Eliane Lessner, Xijie Wang, and Pietro Musumeci. *Report of the Basic Energy Sciences Workshop on the Future of Electron Sources*. Department of Energy. Sept. 2016.

[2] Z. Zhang et al. “A high-power, high-repetition-rate THz source for pump–probe experiments at Linac Coherent Light Source II”. In: *Journal of Synchrotron Radiation* 27.4 (July 2020), pp. 890–901. DOI: `10.1107/S1600577520005147`.

[3] J. Schmerge et al. *A tunable, linac based, intense, broad-band THz source forpump-probe experiments*. Tech. rep. SLAC-R-1049. Feb. 2015. DOI: `10.2172/1169458`.

[4] W. Ronny Huang et al. “Highly efficient terahertz pulse generation by optical rectification in stoichiometric and cryo-cooled congruent lithium niobate”. In: *Journal of Modern Optics* 62.18 (2015), pp. 1486–1493. DOI: `10.1080/09500340.2013.868547`. eprint: `https://doi.org/10.1080/09500340.2013.868547`.

[5] Kai Zhong et al. “Optically pumped terahertz sources”. In: *Science China Technological Sciences* 60.12 (Dec. 2017), pp. 1801–1818. DOI: `10.1007/s11431-017-9057-3`.

[6] Samantha M. Lewis, Emilio A. Nanni, and Richard J. Temkin. “Direct Machining of Low-Loss THz Waveguide Components With an RF Choke”. In: *IEEE Microwave and Wireless Components Letters* 24.12 (Dec. 2014), pp. 842–844. DOI: `10.1109/LMWC.2014.2303161`.

[7] Emilio A Nanni et al. “Prototyping high-gradient mm-wave accelerating structures”. In: *Journal of Physics: Conference Series* 874 (July 2017), p. 012039. DOI: `10.1088/1742-6596/874/1/012039`.

[8] Mohamed Othman et al. “Prototyping of Brazed mm-Wave Accelerating Structures”. In: *Proceedings of the 10th Int. Particle Accelerator Conf.* IPAC2019 (2019), pp. 1–2. DOI: `10.18429/JACOW-IPAC2019-THPGW078`.

[9] X. J. Wang, X. Qiu, and I. Ben-Zvi. “Experimental observation of high-brightness microbunching in a photocathode rf electron gun”. In: *Physical Review E* 54.4 (Oct. 1996), R3121–R3124. DOI: `10.1103/PhysRevE.54.R3121`.

[10] Ben Cook and Pieter Kruit. “Coulomb interactions in sharp tip pulsed photo field emitters”. In: *Applied Physics Letters* 109.15 (Oct. 2016), p. 151901. DOI: `10.1063/1.4963783`.

[11] R. Ganter et al. “Laser-Photofield Emission from Needle Cathodes for Low-Emittance Electron Beams”. In: *Physical Review Letters* 100.6 (Feb. 2008), p. 064801. DOI: `10.1103/PhysRevLett.100.064801`.

[12] L. Wimmer et al. “Terahertz control of nanotip photoemission”. In: *Nature Physics* 10.6 (June 2014), pp. 432–436. DOI: `10.1038/nphys2974`.

[13] Sha Li and R. R. Jones. “High-energy electron emission from metallic nano-tips driven by intense single-cycle terahertz pulses”. In: *Nature Communications* 7.1 (Dec. 2016), p. 13405. DOI: `10.1038/ncomms13405`.

[14] V A Dolgashev. “Traveling Wave Linear Accelerator With RF Power Flow Outside of Accelerating Cavities”. In: *Proceedings LINAC2016* (2017), pp. 48–51.

[15] W. D. Kilpatrick. “Criterion for Vacuum Sparking Designed to Include Both rf and dc”. In: *Review of Scientific Instruments* 28.10 (Oct. 1957), pp. 824–826. DOI: `10.1063/1.1715731`.

[16] Gregory A. Loew and J. W. Wang. “RF Breakdown studies in room temperature electron linac structures”. In: *13th International Symposium on Dicharges and Electrical Insulation in Vacuum* SLAC–PUB–4647 (May 1988).

[17] Valery Dolgashev et al. “Geometric dependence of radio-frequency breakdown in normal conducting accelerating structures”. In: *Applied Physics Letters* 97.17 (Oct. 2010), p. 171501. DOI: `10.1063/1.3505339`.

[18] Lisa Laurent et al. “Experimental study of rf pulsed heating”. In: *Physical Review Special Topics - Accelerators and Beams* 14.4 (Apr. 2011), p. 041001. DOI: `10.1103/PhysRevSTAB.14.041001`.

[19] C. Limborg-Deprey et al. “Performance of a first generation X-band photoelectron rf gun”. In: *Physical Review Accelerators and Beams* 19.5 (May 2016), p. 053401. DOI: `10.1103/PhysRevAccelBeams.19.053401`.

[20] R. Akre et al. “Commissioning the Linac Coherent Light Source injector”. In: *Physical Review Special Topics - Accelerators and Beams* 11.3 (Mar. 2008), p. 030703. DOI: `10.1103/PhysRevSTAB.11.030703`.

[21] W. J. Brown et al. “Experimental and theoretical investigations of a 17GHz RF gun”. In: *Nuclear Instruments and Methods in Physics Research Section A: Accelerators, Spectrometers, Detectors and Associated Equipment* 425.3 (1999), pp. 441–459. DOI: `https://doi.org/10.1016/S0168-9002(98)01437-5`.

[22] A Jensen et al. “25 Year Performance Review of the SLAC 5045 S-Band Klystron”. In: *Proceedings of the 2nd Int. Particle Accelerator Conf.* IPAC2011.SLAC-PUB-16045 (2011), p. 3.

[23] Dennis Thomas Palmer. *The Next Generation Photoinjector*. Tech. rep. SLAC-R-500, 878424. Sept. 2005, SLAC–R–500, 878424. DOI: `10.2172/878424`.

[24] Christopher M. Pierce et al. "Low intrinsic emittance in modern photoinjector brightness". In: *Physical Review Accelerators and Beams* 23.7 (July 2020), p. 070101. DOI: `10.1103/PhysRevAccelBeams.23.070101`.

[25] L. Velardi et al. "Electron beams produced by innovative photocathodes based on nanodiamond layers". In: *Physical Review Accelerators and Beams* 22.9 (Sept. 2019), p. 093402. DOI: `10.1103/PhysRevAccelBeams.22.093402`.

[26] James McCarter. "Photocathode Research for Electron Accelerators". PhD thesis. University of Virginia, Nov. 2011. DOI: `10.18130/V3VN5H`.

[27] K. E. Nichols et al. "Demonstration of transport of a patterned electron beam produced by diamond pyramid cathode in an rf gun". In: *Applied Physics Letters* 116.2 (Jan. 2020), p. 023502. DOI: `10.1063/1.5128109`.

[28] Xiuyuan Shao et al. "A high-brightness large-diameter graphene coated point cathode field emission electron source". In: *Nature Communications* 9.1 (Dec. 2018), p. 1288. DOI: `10.1038/s41467-018-03721-y`.

[29] B. Hidding et al. "Directions in plasma wakefield acceleration". In: *Philosophical Transactions of the Royal Society A: Mathematical, Physical and Engineering Sciences* 377.2151 (Aug. 2019), p. 20190215. DOI: `10.1098/rsta.2019.0215`.

[30] C. Jing et al. "Electron acceleration through two successive electron beam driven wakefield acceleration stages". In: *Nuclear Instruments and Methods in Physics Research Section A: Accelerators, Spectrometers, Detectors and Associated Equipment* 898 (Aug. 2018), pp. 72–76. DOI: `10.1016/j.nima.2018.05.007`.

[31] C Joshi et al. "Plasma wakefield acceleration experiments at FACET II". In: *Plasma Physics and Controlled Fusion* 60.3 (Mar. 2018), p. 034001. DOI: `10.1088/1361-6587/aaa2e3`.

[32] Edda Gschwendtner and Patric Muggli. "Plasma wakefield accelerators". In: *Nature Reviews Physics* 1.4 (Apr. 2019), pp. 246–248. DOI: `10.1038/s42254-019-0049-z`.

[33] A. V. Arefiev et al. "Beyond the ponderomotive limit: Direct laser acceleration of relativistic electrons in sub-critical plasmas". In: *Physics of Plasmas* 23.5 (May 2016), p. 056704. DOI: `10.1063/1.4946024`.

[34] J Faure et al. "A review of recent progress on laser-plasma acceleration at kHz repetition rate". In: *Plasma Physics and Controlled Fusion* 61.1 (Jan. 2019), p. 014012. DOI: `10.1088/1361-6587/aae047`.

[35] Amin Ghaith et al. "Electron Beam Brightness and Undulator Radiation Brilliance for a Laser Plasma Acceleration Based Free Electron Laser". In: *Instruments* 4.1 (Jan. 2020), p. 1. DOI: `10.3390/instruments4010001`.

[36] Neil V. Sapra et al. "On-chip integrated laser-driven particle accelerator". In: *Science* 367.6473 (Jan. 2020), pp. 79–83. DOI: `10.1126/science.aay5734`.

[37] Emilio A. Nanni et al. “Terahertz-driven linear electron acceleration”. In: *Nature Communications* 6.1 (Dec. 2015), p. 8486. DOI: `10.1038/ncomms9486`.

[38] Dongfang Zhang et al. “Segmented terahertz electron accelerator and manipulator (STEAM)”. In: *Nature Photonics* 12.6 (June 2018), pp. 336–342. DOI: `10.1038/s41566-018-0138-z`.

[39] W. Ronny Huang et al. “Terahertz-driven, all-optical electron gun”. In: *Optica* 3.11 (Nov. 2016), p. 1209. DOI: `10.1364/OPTICA.3.001209`.

[40] G. Burt et al. “Dielectric and THz Acceleration (Data) Programme at the Cockcroft Institute”. In: *Proceedings LINAC2016* (2017), pp. 62–64.

[41] Hanxun Xu et al. *Cascaded high-gradient terahertz-driven acceleration of relativistic electron beams*. 2020. arXiv: `2005.11714 [physics.acc-ph]`.

[42] D Broemmelsiek et al. “Record high-gradient SRF beam acceleration at Fermilab”. In: *New Journal of Physics* 20.11 (Nov. 2018), p. 113018. DOI: `10.1088/1367-2630/aaec57`.

[43] J.B. Rosenzweig et al. “Ultra-high brightness electron beams from very-high field cryogenic radiofrequency photocathode sources”. In: *Nuclear Instruments and Methods in Physics Research Section A: Accelerators, Spectrometers, Detectors and Associated Equipment* 909 (Nov. 2018), pp. 224–228. DOI: `10.1016/j.nima.2018.01.061`.

[44] I. Petrushina et al. “High-Brightness Continuous-Wave Electron Beams from Superconducting Radio-Frequency Photoemission Gun”. In: *Physical Review Letters* 124.24 (June 2020), p. 244801. DOI: `10.1103/PhysRevLett.124.244801`.

[45] R. C. Dhuley et al. “First demonstration of a cryocooler conduction cooled superconducting radiofrequency cavity operating at practical cw accelerating gradients”. In: *Superconductor Science and Technology* 33.6 (June 2020), 06LT01. DOI: `10.1088/1361-6668/ab82f0`.

[46] Mohamed A. K. Othman et al. “Experimental demonstration of externally driven millimeter-wave particle accelerator structure”. In: *Applied Physics Letters* 117.7 (2020), p. 073502. DOI: `10.1063/5.0011397`. eprint: `https://doi.org/10.1063/5.0011397`.

[47] Massimo Dal Forno et al. “rf breakdown tests of mm-wave metallic accelerating structures”. In: *Physical Review Accelerators and Beams* 19.1 (Jan. 2016), p. 011301. DOI: `10.1103/PhysRevAccelBeams.19.011301`.

[48] David M. Pozar. *Microwave Engineering*. 4th ed. Wiley & Sons, 2012. ISBN: 978-0-470-63155-3.

[49] David P Pritzkau. “RF Pulsed Heating”. PhD thesis. Stanford Universty, Jan. 2001, SLAC–R–577, 798978. DOI: `10.2172/798978`.

[50] David P. Pritzkau and Robert H. Siemann. “Experimental study of rf pulsed heating on oxygen free electronic copper”. In: *Physical Review Special Topics - Accelerators and Beams* 5.11 (Nov. 2002), p. 112002. DOI: `10.1103/PhysRevSTAB.5.112002`.

[51] E. L. Murphy and R. H. Good. “Thermionic Emission, Field Emission, and the Transition Region”. In: *Physical Review* 102.6 (June 1956), pp. 1464–1473. DOI: `10.1103/PhysRev.102.1464`.

[52] “Electron emission in intense electric fields”. In: *Proceedings of the Royal Society of London A* 119 (1928), pp. 173–181.

[53] J. W. Wang. “RF properties of periodic accelerating structures for linear colliders”. PhD thesis. Stanford University, 1989.

[54] W. Schottky. “Über kalte und warme Elektronenentladungen”. In: *Zeitschrift für Physik* 14.1 (Dec. 1923), pp. 63–106. DOI: `10.1007/BF01340034`.

[55] Ryan Miller, Y. Y. Lau, and John H. Booske. “Schottky’s conjecture on multiplication of field enhancement factors”. In: *Journal of Applied Physics* 106.10 (Nov. 2009), p. 104903. DOI: `10.1063/1.3253760`.

[56] Martin Reiser. *Theory and Design of Charged Particle Beams*. 2nd ed. Wiley-VCH, 2008. ISBN: 978-3-527-40741-5.

[57] John D. Jackson. *Classical Electrodynamics*. 3rd ed. Wiley & Sons, 1999. ISBN: 978-0-471-30932-1.

[58] Helmut Wiedemann. *Particle Accelerator Physics*. 4th ed. Springer, 2015. ISBN: 978-3-319-18317-6.

[59] Emilio Nanni et al. “Toward High-Power High-Gradient Testing of mm-Wave Standing-Wave Accelerating Structures”. In: *Proceedings of the 9th Int. Particle Accelerator Conf.* IPAC2018 (2018), pp. 1–4. DOI: `10.18429/JACOW-IPAC2018-TUZGBE4`.

[60] E A Nanni et al. “mm-Wave Standing-Wave Accelerating Structures for High-Gradient Tests”. In: *Proceedings of the 7th Int. Particle Accelerator Conf.* IPAC2018 (2016), pp. 1–4.

[61] B. Spataro et al. “High-power comparison among brazed, clamped and electroformed X-band cavities”. In: *Nuclear Instruments and Methods in Physics Research Section A: Accelerators, Spectrometers, Detectors and Associated Equipment* 657.1 (Nov. 2011), pp. 88–93. DOI: `10.1016/j.nima.2011.06.047`.

[62] Xiaowei Wu et al. “High-gradient breakdown studies of an X -band Compact Linear Collider prototype structure”. In: *Physical Review Accelerators and Beams* 20.5 (May 2017), p. 052001. DOI: `10.1103/PhysRevAccelBeams.20.052001`.

[63] Evgenya I. Simakov et al. “Diamond field emitter array cathodes and possibilities of employing additive manufacturing for dielectric laser accelerating structures”. In: National Harbor, MD, USA, 2017, p. 060010. DOI: `10.1063/1.4975877`.

[64] Kimberley Nichols et al. “Modeling of Diamond Field Emitter Arrays for Shaped Electron Beam Production”. In: *Proceedings of the 9th Int. Particle Accelerator Conf.* IPAC2018 (2018), pp. 1–3. DOI: `10.18429/JACOW-IPAC2018-THPML010`.

[65] C.-K. Huang et al. “Modeling of diamond field emitter arrays for a compact source of high brightness electron beams”. In: *Journal of Applied Physics* 125.16 (Apr. 2019), p. 164501. DOI: `10.1063/1.5086292`.

[66] D. Kim et al. “Divergence study and emittance measurements for the electron beam emitted from a diamond pyramid”. In: *Nuclear Instruments and Methods in Physics Research Section A: Accelerators, Spectrometers, Detectors and Associated Equipment* 953 (Feb. 2020), p. 163055. DOI: `10.1016/j.nima.2019.163055`.

[67] J. D. Jarvis et al. “Uniformity conditioning of diamond field emitter arrays”. In: *Journal of Vacuum Science & Technology B: Microelectronics and Nanometer Structures* 27.5 (2009), p. 2264. DOI: `10.1116/1.3212915`.

[68] Jonathan D. Jarvis et al. “Emittance measurements of electron beams from diamond field emitter arrays”. In: *Journal of Vacuum Science & Technology B, Nanotechnology and Microelectronics: Materials, Processing, Measurement, and Phenomena* 30.4 (July 2012), p. 042201. DOI: `10.1116/1.4724312`.

[69] P. Piot et al. “Operation of an ungated diamond field-emission array cathode in a L-band radiofrequency electron source”. In: *Applied Physics Letters* 104.26 (June 2014), p. 263504. DOI: `10.1063/1.4884375`.

[70] K. E. Nichols et al. “Demonstration of transport of a patterned electron beam produced by diamond pyramid cathode in an rf gun”. In: *Applied Physics Letters* 116.2 (Jan. 2020), p. 023502. DOI: `10.1063/1.5128109`.

[71] Heather Andrews et al. “Shaped Beams from Diamond Field-Emitter Array Cathodes”. In: *IEEE Transactions on Plasma Science* (2020), pp. 1–5. DOI: `10.1109/TPS.2020.2984156`.

[72] Ansys. *Ansys HFSS: High Frequency Electromagnetic Field Simulation.* `https://www.ansys.com/products/electronics/ansys-hfss`.

[73] David S. Tax. “Experimental Study of a High Efficiency Step-Tunable MW Gyrotron Oscillator”. PhD thesis. Massachusetts Institute of Technology, 2013.

[74] David S. Tax et al. “Experimental Results for a Pulsed 110/124.5-GHz Megawatt Gyrotron”. In: *IEEE Transactions on Plasma Science* 42.5 (May 2014), pp. 1128–1134. DOI: `10.1109/TPS.2014.2314019`.

[75] Jeffrey M. Neilson et al. “Design and High-Power Test of an Internal Coupler to HE $_{11}$ Mode in Corrugated Waveguide for High-Power Gyrotrons”. In: *IEEE Transactions on Electron Devices* 65.6 (June 2018), pp. 2316–2320. DOI: `10.1109/TED.2018.2805889`.

[76] S. B. van der Greer and M. J. de Loos. *General Particle Tracer.* `http://www.pulsar.nl/gpt/`.

[77] Julian F. Picard et al. “Laser-driven semiconductor switch for generating nanosecond pulses from a megawatt gyrotron”. In: *Applied Physics Letters* 114.16 (Apr. 2019), p. 164102. DOI: `10.1063/1.5093639`.

[78] Vinit Kumar. “Understanding the focusing of charged particle beams in a solenoid magnetic field”. In: *American Journal of Physics* 77.8 (Aug. 2009), pp. 737–741. DOI: `10.1119/1.3129242`.

[79] Santiago Bernal. “Linear magnetic lenses and deflectors”. In: *A Practical Introduction to Beam Physics and Particle Accelerators*. 2053-2571. Morgan & Claypool Publishers, 2016, 2-1 to 2–15. ISBN: 978-1-6817-4076-8. DOI: `10.1088/978-1-6817-4076-8ch2`.

[80] Ansys. *Ansys Maxwell: Low Frequency Electromagnetic Field Simulation*. `https://www.ansys.com/products/electronics/ansys-maxwell/`.